Rigid Origami of Thick Panels and Deployable Membranes

Yue Cao

A dissertation submitted for the degree of Master of Science in the Department of Engineering Science at the University of Oxford

Mansfield College

Trinity Term 2017

Abstract

Rigid origami is about folding flat inextensional facets which are connected by creases. It is gaining popularity and being used in an increasing number of engineering applications. Since this is a relatively new field, a number of challenges exist, e.g., folding facets with a finite thickness and achieving folding compactness. This dissertation summarises two attempts to address these two issues. Specific attention has been drawn to the offset crease technique and the wrapping membrane patterns.

In the first part of this dissertation, I have established a kinematic model describing the offset crease models, which leads to a proof that the motion of the thick panel folding is kinematically equivalent to that of its parent pattern with zero thickness. A detailed design approach for adapting this technique has been proposed and proven to be effective by various physical implementations. In order to achieve a higher compactness, an anisotropic tessellation has been derived from the traditional Miura-ori pattern. Its compatibility with pre-existing thickness accommodation approaches has been demonstrated via thick-panel models.

The second part of the dissertation examines a number of deployable membrane patterns. Firstly, the hexagonal winding membrane has been validated with a strict mathematical proof that a rigid transition is non-existent. Therefore, a number of newly proposed wrapping patterns have been designed and their motions have been studied via numerical simulation to discover the adequate rigid-foldable patterns. The algorithm of the simulation has been synthesised to create visualisation software for simulating general origami patterns. Furthermore, we have proposed a comprehensive scheme to allow arbitrary material thickness to be accommodated for the wrapping patterns. Finally, a sequential square twist pattern with a high deployed-to-stowed ratio has been created.

To My Family

Acknowledgement

During my study in Oxford, I have received support, help and encouragement from a great number of organizations and individuals.

Foremost, I would like to express my sincere gratitude to my supervisor Prof. Zhong You, for his patience, motivation and guidance. He accepted me a student in this world-reputed university and introduced me to this interesting subject of origami-inspired deployable structures, which tremendously helps my career. He imparts me abundant freedom to discover novel assemblies, as well as guiding me to discover the theory behind the intriguing motions with rigorous mathematic validation. His insightful comments and immense knowledge has been extraordinarily beneficial to my research.

My appreciation also goes to the colleagues and staffs in the Department of Engineering Science at University of Oxford. I would particularly like to single out Mr. Tuo Wang for his selfless help and patient instruction in the process of programming. Without him, I could not imagine how frustrated I could be when dealing with those tricky challenges. I also thank Mr. Bob Scott, Mr. Clive Baker, Prof. Chris MacMinn and Dr Ross McAdam for their valuable guidance and technical support during my study.

Financial aid from the China-Oxford Scholarship Funds (COSF) and Mansfield College Graduate Awards are greatly appreciated. With the funds, my financial pressures are to some extent mitigated, which makes me more focus on my research.

I deeply appreciate all my dearest friends I meet in this town. Because of you I never walk alone even in the darkest night. A big thanks to my ex-girlfriend Miss. Pu Sun for her thoughtful care and warm companion. Because of you I never stray too far from the vast

and hazy meadow. I am very grateful to my parents for their endless love and unconditional support from all aspects. Because of you I am never afraid of standing still against gale.

Over the past two years, I have experienced triumph and frustration, but mostly, ordinary days. It was those ones who support me to complete this thesis. My flat words are insufficient to express my sincerest gratitude and they deserve more than that.

Table of Contents

List of Figures

List of Tables

Nomenclature

$\boldsymbol{A_i}$	Matrix for solving $\boldsymbol{\Phi}_i$ at i^{th} step.
$\boldsymbol{B_i}$	Matrix for solving $\boldsymbol{\Phi}_i$ at i^{th} step.
$\boldsymbol{C}$	Compatibility matrix.
C	Width of creases.
C^H	Width of creases along horizontal path in the Miura-ori.
C_μ^H	Width of the μ^{th} crease along horizontal path in the Miura-ori.
C^Z	Width of creases along zigzag path in the Miura-ori.
D	Dimension of an assembly.
E_i	i^{th} part of equation.
$\boldsymbol{G}$	Matrix of the node-bar relationship.
$\boldsymbol{H}$	Equilibrium matrix.
$\boldsymbol{H'}$	Modified equilibrium matrix formed by nodal coordinates only.
$\boldsymbol{L}$	Reshaped matrix of bar lengths.
$\boldsymbol{L'}$	Vector of bar lengths.
N	Number of sides of a polygon.
P_i	i^{th} crease of the winding membrane.
$Q_{i(i+1)}$	Three dimensional transformation matrix between reference frame i and reference frame i+1.
R	Revolute joint.
R_i	i^{th} revolute joint.
$T_{i(i+1)}$	Four dimensional transformation matrix between reference frame i and reference frame i+1.

$\boldsymbol{U_i}$	Orthogonal matrix in singular value decomposition at i^{th} step.
$\boldsymbol{V_i}$	Orthogonal matrix in singular value decomposition at i^{th} step.
$\boldsymbol{W_i}$	Diagonal matrix in singular value decomposition at i^{th} step.
$a_{i(i+1)}$	Link length, i.e. distance between axis of joint i and axis of joint i+1.
b	Number of bars.
c_i	Coordinate of point i.
$\boldsymbol{d}$	Vector of nodal displacements.
$\boldsymbol{d}_i$	Vector of nodal displacements at step i.
$\boldsymbol{e}$	Vector of bar elongation.
f_i	Number of the kinematic variables of joint i.
g	Width of a parallelogram of the anisotropic Miura-ori.
h	Height of a parallelogram of the anisotropic Miura-ori.
j	Number of joints of a linkage.
j_n	Number of non-foundation joints.
k	Sequential number of bars.
l	Length of a bar.
$l_{i,k}$	Length of k^{th} bar at i^{th} step.
m	Mobility of a mechanism.
n	Number of links of a linkage.
$\boldsymbol{p}$	Vector of applied nodal loads.
q	Number of independent rigid mechanisms.
r	Rank of equilibrium matrix $\boldsymbol{H}$.
s	Number of states of self-stress.
$\boldsymbol{t}$	Vector of bar forces.

x	Coordinates in Cartesian system.
y	Coordinates in Cartesian system.
z	Coordinates in Cartesian system.
$\alpha_{i(i+1)}$	Link twist around axis x_i, i.e. angle between axis of joint i and axis of joint i+1.
β	Sector angle in a wrapping pattern.
γ_i	i^{th} forward path.
δ	Sector angle in a wrapping pattern.
η	Sector angle in a wrapping pattern.
$\boldsymbol{\varepsilon}$	Vector of force coefficients.
ε_{vr}	Force coefficient between nodes v and r.
ε_{vu}	Force coefficient between nodes v and u.
ε_{vw}	Force coefficient between nodes v and w.
ϵ_{ik}	Strain of kth bar at ith step.
θ_i	Link rotation around axis z_i, i.e. angle between link length i and link length i+1.
κ	Sector angle of a parallelogram of the anisotropic Miura-ori.
λ	Thickness of a single layer.
μ	Sequential number of the horizontal creases in the Miura-ori.
τ	Locally obstructive pattern of the winding membrane.
ω	Sector angle in a wrapping pattern.
Δ_i	Amplitude of a predictor at step i.
$\boldsymbol{\Phi}_i$	Vector of correctors at step i.

$\boldsymbol{\Psi}_i'$	Configuration of a pin-jointed framework at step i.
$\boldsymbol{\Psi}_i$	Configuration of a pin-jointed framework before applying corrector $\boldsymbol{\Phi}_i$ at step i.
Ω_i	i^{th} wrapping pattern.

1. Introduction

1.1 Background

Origami is the ancient art of transforming a flat piece of paper into a variety of 3D shapes by simply folding along a pre-set crease pattern. Originating in China in the 17th century and subsequently being refined in Japan, this conventional paper folding skill still retains its richness which has been empowered by generations of origami practitioners. Advances in its geometry analysis to date has provided new tools to bring this art to the field of science. It has recently seen an explosion of research interests among scientists and engineers as origami provides them with new sources of inspiration for developing new structures. The diversity of folding materials allows intricate but elegant 3D objects to be created whose dimensions range from nanoscale structures to large buildings. Recent applications include medical stents (Duerig and Wholey, 2002), solar panels (Miura, 1980), transforming robotics (Felton et al., 2014) and kinematic architectures (Merchan, 1987). Most of them are constructed using relatively rigid materials, which requires the structures to be folded without either stretching any surface or generating new creases during the entire folding process. This type of origami is known as the rigid origami, which is the focus of this dissertation.

1.2 Motivation

In a mathematics context, the kinematic model of rigid origami disregards material thickness. The physical implementations, however, will inevitably involve folding panels of non-zero thickness, leading to failure to achieve the desired foldability due to self-intersections. Accommodating panel thickness is therefore one of the crucial challenges when developing origami-inspired deployable structures. Various thickness-accommodating techniques have been proposed. Prominent contributions include the hinge

shift technique (Hoberman, 2010), the use of tapered materials (Tachi, 2011) and offseting panels (Edmondson et al., 2014). All of these methods are capable of preserving the original kinematics of its zero-thickness counterpart. However, their utilisation in real structures has been limited due to failure to achieve the full range of motion or maintaining surface flatness. A novel thickness-accommodating method proposed by Ku and Demaine (2016), which uses double parallel creases, shows promise in addressing these limitations. However, its kinematics remains unclear. A rigorous validation and an elaborated implementation method are therefore imperative.

On the other hand, one of the most noticeable origami-inspired applications is the way in which solar panels on spacecraft are folded. Solar energy receivers on a satellite need to be folded towards the central body for launch, and deployed into a flat profile once in orbit. This can be achieved by a handful of origami patterns which wrap the circumjacent facets around a central hub. The earliest recorded example of such a pattern was in the early 1960s (Huso, 1960), which involved a sheet reel for retracting the tarpaulin shade of a vehicle. It utilised the spin of the central post to draw the shade towards the hub. This pioneered wrapping technique has been refined subsequently to achieve a higher deployed-to-stowed ratio. Two remarkable contributions were made by Scheel (1974) and Cambridge Consultants (1989) who adopted the wrapping pattern for the application of a solar sail. However, none of the existing wrapping techniques are capable of preventing the panels from being stretched during the folding and unfolding process, causing damage to the solar array surfaces if they are undeformable. Although the winding membrane proposed by Guest and Pellegrino (1992) claimed to be inextensional, it was only proven to be so in the fully flat and the fully stowed configurations. A rigid transition is empirically speculated to be non-existent, despite a lack of a rigorous mathematical proof.

1.3 Scope and aim

In the light of the aforementioned inadequacies, two primary aims were set for this project.

The first was to establish a kinematic model for thickened origami with the offset crease technique, and to develop an implementation method for adopting this technique to rigid origami patterns.

The second was to design a number of inextensional deployable models that can be applied to different types of solar energy receivers. The rigid foldability of each pattern would be examined with rigorous kinematic analysis. A thickness-accommodation scheme was then to be designed for the eligible wrapping patterns.

1.4 Dissertation layout

Layout of the dissertation is as follows.

Chapter 2 provides a comprehensive literature review related to this work, encompassing an analogy between rigid origami and mechanical linkages, the mobility of an assembly, the research methodology, existing origami patterns, thickness-accommodation techniques and inextensional wrapping patterns. The analysis of past contributions clearly leads to the motivation of this work.

Chapter 3 concerns with the rigid origami of thick panels. In particular, the further development of the offset crease technique is presented, including a detailed kinematic analysis and an elaborated strategy for adopting the technique to general tessellations. A modified tessellation based on the traditional Miura-ori pattern is then proposed, and its compatibility with the thickness accommodation techniques is demonstrated.

Chapter 4 is dedicated to the design of an inextensionally deployable membrane. Firstly, a rigorous validation of the rigid foldability of the winding membrane is presented. This is

followed by a set of newly proposed wrapping patterns, including the patterns with multi-layer layouts and square hubs. Furthermore, the algorithm employed is programmed to produce a rigid origami simulator with visualised interfaces. A thickness accommodation scheme is designed for the eligible wrapping patterns. Finally, a sequentially square twist pattern is proposed.

The major achievements of this research project and recommendations for future work are summarised in Chapter 5, which concludes the dissertation.

2. Literature Review

2.1 Linkages and mobility

2.1.1 Rigid origami and mechanical linkages

Rigid Origami is a type of origami for which foldability can be retained with neither deforming any panels nor creating any new creases (Edmondson, 2015). It can be modelled kinematically using mechanism theory.

In the theory of mechanisms, a kinematic chain refers to an assembly formed by a number of rigid bodies. The bodies, or links, are interconnected by kinematic joints. If all the joints in a kinematic chain are lower pairs, such as revolute joints or spherical joints, the assembly is sub-categorized as a mechanical linkage.

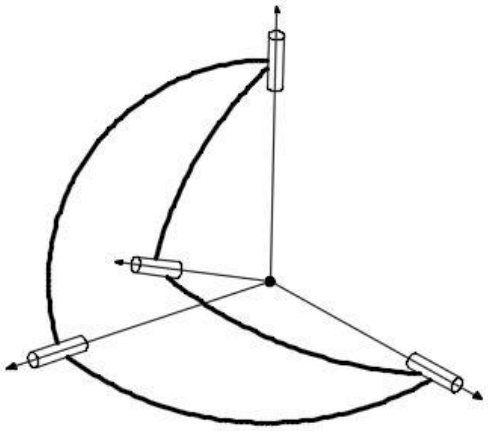

Figure 2.1 A spherical linkage transformed from a rigid origami pattern.

A rigid origami can be commonly treated as a mechanical linkage, where rigid panels act as the links and creases as revolute joints (R). For a single vertex origami, if the axes of the revolute joints meet at a point, the linkage is a spherical linkage (Figure 2.1). The trajectories of links stay on a concentric sphere (You and Chen, 2012), and the sum of sector angles around a vertex is 2π (Ruth and McCarthy, 1999). If the material thickness

is considered, the axes of revolute joints may not intersect. The linkage falls into the category of spatial linkages (Chen, Peng and You, 2015).

2.1.2 Mobility of a linkage

The mobility, *m*, of a mechanism refers to the number of inputs needed to determine the motion of the entire assembly with respect to the ground. This is also commonly known as the degree of freedom (DoF) (You and Chen, 2012). The mobility of an assembly is calculated using the Kutzbach criterion (Hunt, 1978). For a free rigid link in a 3D space, there are six degrees of freedom: three displacements and three rotations in three directions. Therefore *n* free links are supposed to have 6*n* degrees of freedom. If one link is deemed as ground, the remaining degrees of freedom become to $6(n-1)$. A binary joint with f degrees of freedom connecting two links reduces the degrees of freedom by $6-f$. For non-binary connection with *n* links, the number of joints at that connection is counted as $n-1$.

For a spatial linkage which consists of *n* links connected by *j* joints, where each joint has f_i ($i=1,2,\ldots,j$) degrees of freedom, the mobility, m, is calculated as

$$m = 6(n-1) + \sum_{i=1}^{j}(6-f_i) \tag{2.1a}$$

or

$$m = 6(n-j-1) + \sum_{i=1}^{j} f_i. \tag{2.1b}$$

This equation applies to a spatial linkage. For a planar assembly where the axes of joints are all parallel, the trajectories of all points on the bodies are constrained on a common plane. The mobility equation thus becomes

$$m = 3(n - j - 1) + \sum_{i=1}^{j} f_i. \quad (2.2)$$

Only three degrees of freedom are applicable in a plane: two displacements and one rotation. This equation is also true for spherical linkages as only rotations around three concurrent axes are allowed. The parallel constraint for planar linkages and the concurrent constraint for spherical linkages mean the two types of linkage resemble to each other in kinematic properties. In effect, the parallel rotational axes of a planar linkage can be deemed to meet at infinity.

Despite the clarity of its application, this criterion presents a number of limitations which may cause confusion. Firstly, it describes the global mobility only, which means the locally movable components are not able to be detected. Besides that, it is noted that the mobility calculated from the Kutzbach criterion may consist of an idle degree of freedom. For example, if a link is jointed with two spherical joints at both ends, it is free to rotate about itself. Such motion needs to be identified to obtain useful mobility. Moreover, generally, if a mechanism has non-positive mobility calculated from the Kutzbach criterion, the mechanism turns into a fixed structure. However, it may still possess full range motion as an over-constrained mechanism if some special geometry conditions are fulfilled (Baker and Min, 1986). This is due to the intrinsic ignorance of geometric information from this mobility calculation criterion. The Kutzbach criterion has no connection with dependency if analytical tools (such as linear algebra, affine geometry, etc) are not applied. For example, the degrees of freedom of both parallelogram planar linkages (as shown in Figure 2.2) are calculated as zero. Full range motion can still be achieved if link *a* is parallel with link *b* and link *c* (Figure 2.2-A) although the mobility calculation demonstrates otherwise. Therefore, the criterion only provides the lower bound of the possible non-idle mobility

for a configuration, which means the practical value of this criterion is limited, despite of its valuable theoretical foundations.

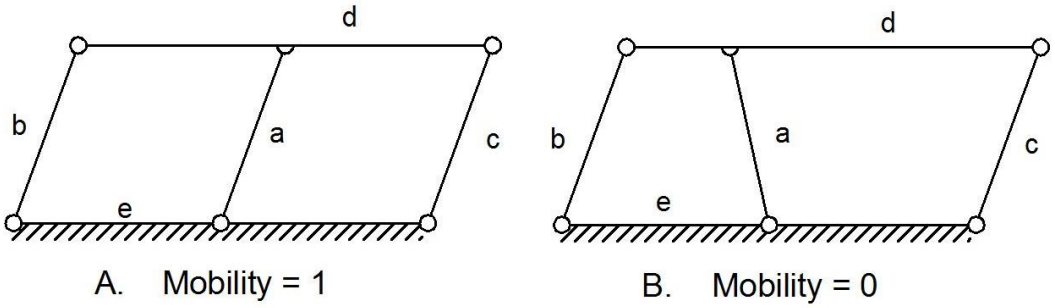

Figure 2.2 (A) A planar over-constrained mechanism and (B) a planar fixed structure.

2.2 Research methodology

The topology and geometry of rigid origami has provided engineering challenges with novel solutions. Before addressing this issue, rigorous mathematical models must be established to fully understand the motion of bodies. A series of research has been conducted utilising various methods. Huffman (1976) derived a computer-aided strategy based on the Gaussian curvature of polygonal surfaces. At the area next to vertices and creases, the curvature remains unchanged for inextensional mechanisms. Wu and You (2010) unitized rotating vectors to represent 3D configurations of the spherical linkages with closed loop equations, enabling full range motion to be traceable. Quaternions and dual quaternions were employed to convert the intricate spatial trajectories to a series of nonlinear equations. The sequential quadratic programming method was then applied to converge this to an optimized solution. Evans et al. (2015) employed the concept "gadgets" to examine the rigidity of origami, where a gadget refers to a localised bunch of crease patterns that can replace apices. This approach can be further applied to improve existing tessellations as well as creating new crease patterns.

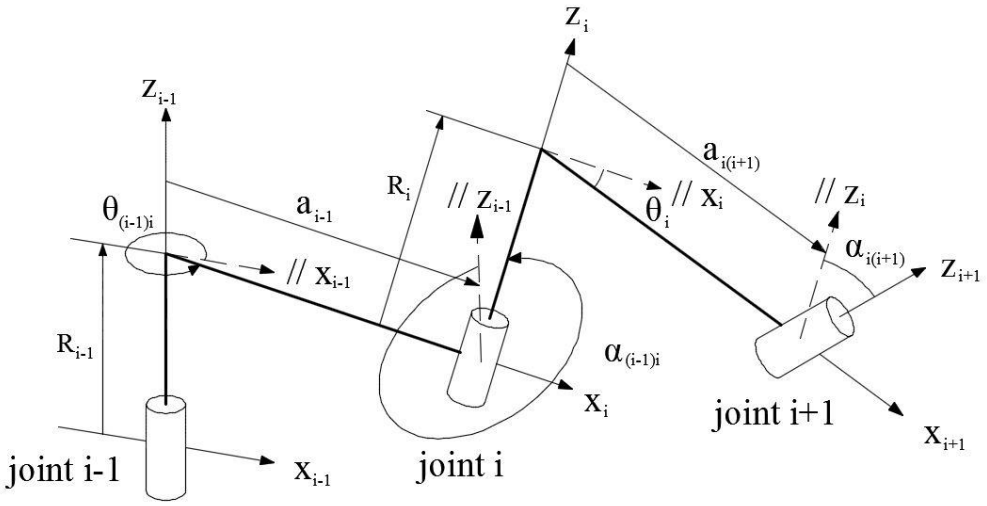

Figure 2.3 Coordinate systems with DH notation attached. Picture reproduced from You and Chen (2012).

There are two approaches that are immensely relevant to this report. Denavit and Hartenberg (1955) established a matrix based method (known as the DH notation) which is widely used in spatial mechanism analysis. The coordinates *c* of a point *i*, in a fixed reference frame are transformed by a four dimensional matrix, thus providing new coordinates $c_{(i+1)}$ on a moving reference frame. Thus,

$$c_{(i+1)} = T_{i(i+1)}c_i, \tag{2.3}$$

where

$$T_{i(i+1)} = \begin{bmatrix} \cos\theta_i & -\cos\alpha_{i(i+1)}\sin\theta_i & \sin\alpha_{i(i+1)}\mathrm{Sin}\theta_i & a_{i(i+1)}\cos\theta_i \\ \sin\theta_i & \cos\alpha_{i(i+1)}\cos\theta_i & -\sin\alpha_{i(i+1)}\cos\theta_i & a_{i(i+1)}\sin\theta_i \\ 0 & \sin\alpha_{i(i+1)} & \cos\alpha_{i(i+1)} & 0 \\ 0 & 0 & 0 & 1 \end{bmatrix}. \tag{2.4a}$$

It can be shown that

$$T_{(i+1)i} = T_{i(i+1)}^{-1} = \begin{bmatrix} \cos\theta_i & \sin\theta_i & 0 & -a_{i(i+1)} \\ -\cos\alpha_{i(i+1)}\sin(\theta_i) & \cos\alpha_{i(i+1)}\cos\theta_i & \sin\alpha_{i(i+1)} & 0 \\ \sin\alpha_{i(i+1)}\sin(\theta_i) & -\mathrm{Sin}\alpha_{i(i+1)}\cos\theta_i & \cos\alpha_{i(i+1)} & 0 \\ 0 & 0 & 0 & 1 \end{bmatrix}. \tag{2.4b}$$

This allows the link twist $\alpha_{i(i+1)}$, joint angle θ_i and link length $a_{i(i+1)}$ to be taken into account during the transformation and a forward path can then be obtained by iteratively applying Eq. 2.3. If this path reaches the initial reference frame, a closed loop can be obtained. For a loop-closure assembly containing *n* links, it gives

$$T_{12}T_{23}T_{34}\dots T_{n1} = I_4 \tag{2.5}$$

where I_4 refers to a four by four unit matrix. If *i+1>n*, *n* is substituted for 1.

For a spherical linkage, link lengths $a_{i(i+1)}$ are all zero since all the axes meet at a concurrent point. The transformation matrix $T_{i(i+1)}$ can be reduced to three dimensional matrix $Q_{i(i+1)}$, which is

$$Q_{i(i+1)} = \begin{bmatrix} \cos\theta_i & -\cos\alpha_{i(i+1)}\sin\theta_i & \sin\alpha_{i(i+1)}\sin\theta_i \\ \sin\theta_i & \cos\alpha_{i(i+1)}\cos\theta_i & -\sin\alpha_{i(i+1)}\cos\theta_i \\ 0 & \sin\alpha_{i(i+1)} & \cos\alpha_{i(i+1)} \end{bmatrix}. \tag{2.6a}$$

Similarly, there is

$$Q_{(i+1)i} = Q_{i(i+1)}^{-1} = \begin{bmatrix} \cos\theta_i & \sin\theta_i & 0 \\ -\cos\alpha_{i(i+1)}\sin\theta_i & \cos\alpha_{i(i+1)}\cos\theta_i & \sin\alpha_{i(i+1)} \\ \sin\alpha_{i(i+1)}\sin\theta_i & -\sin\alpha_{i(i+1)}\cos\theta_i & \cos\alpha_{i(i+1)} \end{bmatrix}. \tag{2.6b}$$

The closed loop condition yields

$$Q_{12}Q_{23}Q_{34}\dots Q_{n1} = I_3, \tag{2.7}$$

where I_3 refers to a three by three unit matrix.

The matrix based approach is widely used for examining the kinematics of rigid origami due to its simplicity in mathematic knowledge. It allows geometric features of a mechanism to be considered. Once a loop-closure equation is obtained, the whole system is actually locked. Through the assignment of the input variables, the value of all output variables can be obtained. The number of required input variables is, in fact, the mobility of the assembly.

Meanwhile, the full range motion can be tracked by altering the variables within its attainable range.

However, this method has a few evident drawbacks that may cause problems in some cases. The concatenation of matrices produces a system of non-linear simultaneous equations, consisting of massive trigonometric functions. It is thus not feasible to create a systematic method to simplify these complex trigonometric equations. This means the analytic procedure can be computationally expensive and a solution is not guaranteed. Since a value of trigonometric function may yield more than one answer, a portion of equations may require to be squared. Consequently, each output variable needs to be validated before being used for subsequent calculation. It could potentially augment the computational time and lead to ambiguity. Another apparent shortcoming of this forward kinematics is its incompetence in dealing with complex open loop problems. For some simple open loop cases, the coordinates system of the next body can be established through assigning the value of particular variables. Nonetheless, for origami, some facets or creases may be removed or trimmed. The application of the matrix method therefore turns the loop-closure conditions to multi-open-loop systems. This would generate an excessive number of variables whose values demand to be predicted, which makes it unsuitable for using this method.

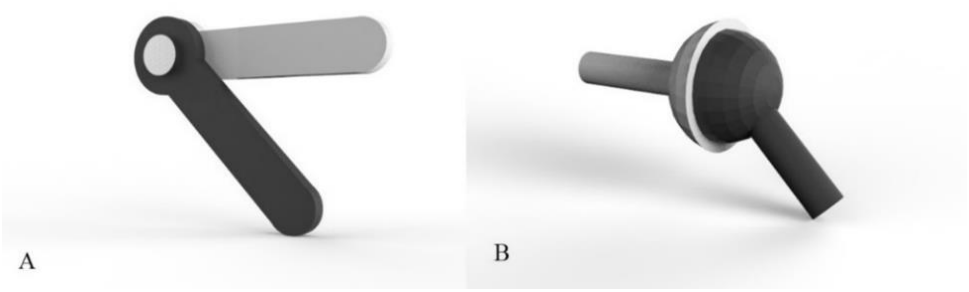

Figure 2.4 (A) A revolute joint and (B) a spherical joint.

Kumar and Pellegrino (2000) proposed a mechanical modelling method to simulate rigid motions of origami. This is done by converting an origami pattern to a pin-jointed frame, i.e. to replace the two fundamental elements of an origami pattern, creases and vertices, with links and pins, respectively. These pin joints can be revolute joints (Figure 2.4-A) in a planar mechanism or spherical joints (Figure 2.4-B) in a 3D mechanism. Furthermore, in order to constrain trivial internal movements, additional diagonal bars are introduced to triangulate facets. The origami pattern is therefore transformed to a truss frame consisting of multiple triangular facets (Figure 2.5).

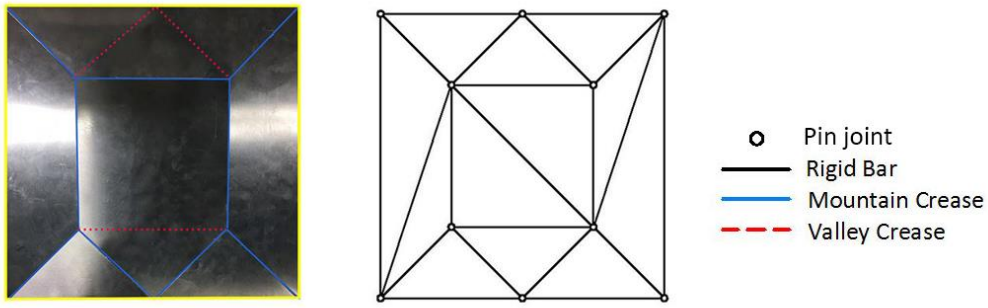

Figure 2.5 Transformation from an origami pattern to a pin-jointed truss frame.

To carry out numerical simulation, the geometrical properties of a pin-jointed frame are incorporated into two linearized equations, which are

$$\mathbf{Ht} = \mathbf{p}, \tag{2.8}$$

$$\mathbf{Cd} = \mathbf{e}, \tag{2.9}$$

where equilibrium matrix $\mathbf{H}$ relates bar forces $\mathbf{t}$ to applied nodal loads $\mathbf{p}$, and compatibility matrix $\mathbf{C}$ relates nodal displacement $\mathbf{d}$ to bar elongation $\mathbf{e}$. Kinematic-static duality yields

$$\mathbf{C} = \mathbf{H}^T. \tag{2.10}$$

Once the matrix has been constructed, the next step is to calculate the number of independent rigid mechanisms q and the number of states of self-stress s. According to Pellegrino and Calladine (1986), there is,

$$q = Dj_n - r, \tag{2.11}$$

$$s = b - r. \tag{2.12}$$

The two parameters are associated with the number of non-foundation joints j_n, the dimension of an assembly D, the number of bars b and the rank r of the equilibrium matrix **H**. That means all the information required can be obtained at this stage. Similar to the calculation of mobility, the determination of parameters q and s also yield necessary but not sufficient conditions for static and kinematic determinacy (Hutchinson and Fleck, 2006). However, this approach has an evident advantage over the calculation of mobility due to its ability in detecting bifurcation points. When $q \geq 2$ and $s \geq 1$, the assembly is at a bifurcation point, which means the mechanism has more than one possible motions in this particular configuration. Once a motion has been selected, the assembly will move along this single kinematic path until the next bifurcation point has been reached.

Next, the trivial internal movement needs to be constrained. Despite being triangulated, the panels still bend easily. Schenk and Guest (2011) applied extra constraints by vector inspection of dihedral fold angles. However, this step requires the compatibility matrix to be reformulated with a number of newly introduced vectors, which largely increases the complexity of the method.

The kinematic behaviour of a pin-jointed framework can now be analysed. For a configuration $\boldsymbol{\Psi}_i'$ which moves along a single kinematic path, the subsequent configuration $\boldsymbol{\Psi}_{i+1}$ can be predicted by

$$\boldsymbol{\Psi_{i+1} = \Psi'_i + \mathbf{d}_i \Delta}. \quad (2.13)$$

The nodal displacement $\mathbf{d}_i$ can be obtained by solving the null space of the compatibility matrix via singular value decomposition (SVD). The magnitude and the sign of Δ determine the amplitude and the direction of this predictor step. A corrector $\boldsymbol{\Phi_{i+1}}$ is then introduced to modify bar lengths to their original values, allowing the correct configuration $\boldsymbol{\Psi'_{i+1}}$ with no bar extension to be obtained. Thus,

$$\boldsymbol{\Psi'_{i+1} = \Psi_{i+1} + \Phi_{i+1}}. \quad (2.14)$$

Iterative execution of this predict-correct augmentation allows trajectories of full range motion to be traceable, thus a mechanism can be analysed without any stretches or bends.

This mechanical modelling method suits well for all origami patterns, including those who have certain panels or creases being trimmed away, as it does not rely on a loop closure condition. Unlike the matrix method, the mechanical modelling method does not detect any deformation. Instead, the iterative approach stipulates constant bar lengths, and presents the trajectories of motion in an intuitionistic way. This approach still suffers a handful of disadvantages: 1) fundamentally, it is a type of numerical validation, therefore the results are approximate values and the small errors in each step will be accumulated thus affecting accuracy; 2) at the bifurcation point, a desired path of motion needs to be selected manually. These drawbacks limit its utility on a number of origami validation problems.

2.3 Origami patterns

2.3.1 Single-vertex origami patterns

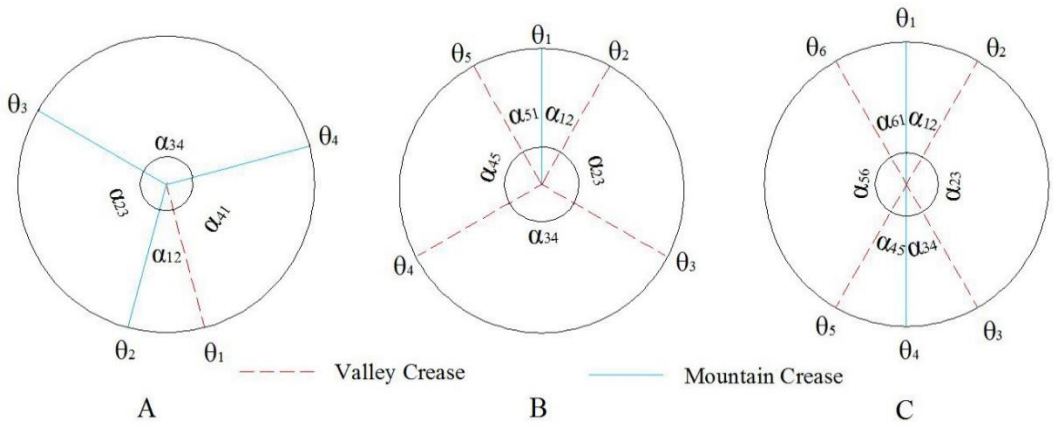

Figure 2.6 Examples of spherical linkages for origami: (A) 4R, (B) 5R and (C) 6R.

For an original origami pattern constructed with paper, a single vertex origami pattern can be treated as a spherical linkage when the thickness of panels is neglected because all creases meet at a concurrent point. It forms a loop-closure system where the spherical perimeter is 2π, and it contains an equal number of links and joints. According to Miura (1989a), in order to preserve mobility, the minimum number of creases around a vertex is four. It is called a degree-four vertex, also known as a spherical 4R linkage. This type of mechanism consists of three mountain creases and one valley crease, or vice versa, as shown in Figure 2.6-A. If four sector angles satisfy the condition $\alpha_{12} + \alpha_{34} = \alpha_{23} + \alpha_{41} = \pi$, the pattern can be folded flat (Hull, 1994). Chen, Peng and You (2015) discovered a relationship between the rotations, which are

$$\theta_2 = \theta_4, \tag{2.15a}$$

$$\theta_1 = -\theta_3, \tag{2.15b}$$

where θ_1 refers to the rotation about a valley crease and $\theta_2, \theta_3, \theta_4$ correspond to those of the mountain creases.

The relationship between rotations is dependent on sector angles α, which are

$$\frac{\tan\frac{\theta_1}{2}}{\tan\frac{\theta_2}{2}} = -\frac{\sin\frac{\alpha_{23}-\alpha_{45}}{2}}{\sin\frac{\alpha_{23}+\alpha_{45}}{2}}. \tag{2.16}$$

Besides the spherical four-bar linkage, Chen, Peng and You (2015) also discovered angular relationships for symmetric types of assembly with five and six creases, respectively. For a symmetric spherical 5R linkage, shown in Figure 2.6-B, the conditions are

$$\alpha_{51} = \alpha_{12}, \alpha_{23} = \alpha_{45} = \frac{\pi}{2}, \alpha_{34} = \pi - 2\alpha_{12}, \tag{2.17a}$$

$$\theta_4 = \theta_3, \theta_5 = \theta_2. \tag{2.17b}$$

The equations obtained through loop-closure conditions are

$$\frac{tan\frac{\theta_3}{2}}{tan\frac{\theta_2}{2}} = \frac{1-sin\alpha_{12}}{cos\alpha_{12}}, \tag{2.18}$$

and

$$tan^2\frac{\theta_2}{2} - \frac{2tan\frac{\theta_2}{2}}{tan\frac{\theta_1}{2}}\frac{cos\alpha_{12}}{1-sin\alpha_{12}} - \frac{1+sin\alpha_{12}}{1-sin\alpha_{12}} = 0. \tag{2.19}$$

Similarly, for a symmetric spherical 6R linkage, shown in Figure 2.6-C, the conditions are

$$\alpha_{12} = \alpha_{34} = \alpha_{45} = \alpha_{61}, \alpha_{23} = \alpha_{56} = \pi - 2\alpha_{12}, \tag{2.20a}$$

$$\theta_1 = \theta_4, \theta_2 = \theta_3 = \theta_5 = \theta_6. \tag{2.20b}$$

and

$$\tan\frac{\theta_1}{2} + cos\alpha_{12}tan\frac{\theta_2}{2} = 0. \tag{2.21}$$

2.3.2 Multi-vertex origami tessellations

So far the kinematics of commonly used single-vertex origami patterns have been given. In general, origami tessellations are formed by a combination of single vertex origami patterns. The originally independent vertices can be linked through simply merging adjacent panels and creases. A number of origami tessellations have been proposed for diverse applicable purposes. Remarkable applied contributions include the water bomb pattern (Lang, 2003) and the diamond pattern (Yoshimura, 1955), which consists of six-crease vertices, as well as Miura-ori (Miura, 1989b) and the traditional square-twist pattern (Lang, 2003), which are formed by four-crease vertices. The latter three are closely related to this thesis.

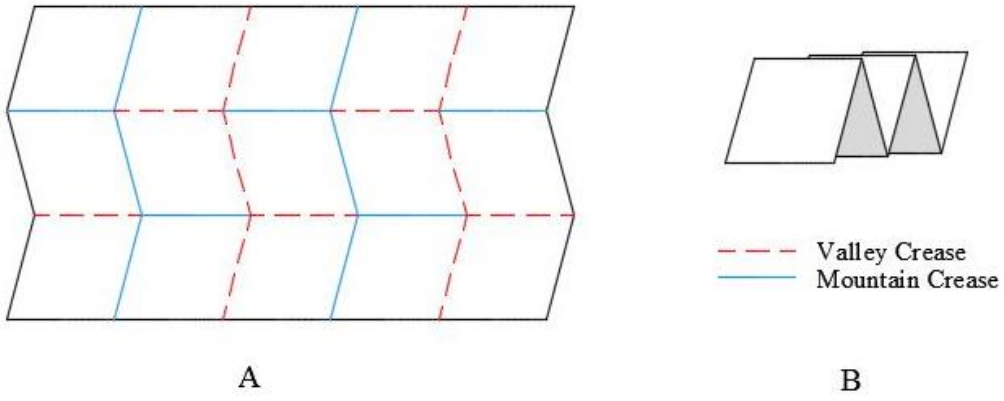

Figure 2.7 The Miura-ori pattern in (A) the fully flat state and (B) the fully folded state.

Miura-ori (Figure 2.7) sets a milestone for origami structures which have been applied to a wide range of applications from map folding to deployable solar panel arrays. Geometrically it consists of a set of congruous parallelograms, which are arranged by translating in one direction and mirroring to the orthogonal direction. Therefore a corrugated surface is formed and bounded by straight and zigzag lines, respectively (Sareh and Guest, 2015). In fact, it is made of a group of 4R spherical linkages and its mobility calculated from the Kutzbach criterion is negative. However, exertion of symmetry enables rigid deployment from this over-constrained system (Sternberg, 2010). Moreover, the little

skew of zigzag lines offers the configuration a predefined direction and enables collapse by releasing internal forces. Satisfaction of these two conditions allows the highly over-constrained assembly, Miura-ori, to be actuated with a single mobility (Mavroidis and Roth, 1995).

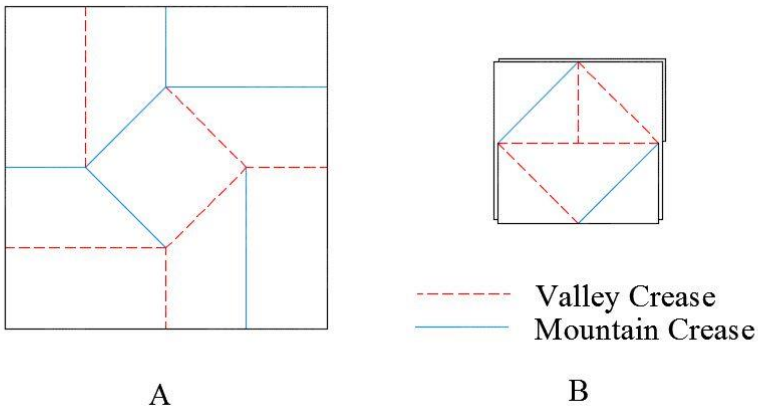

Figure 2.8 The square twist pattern at (A) the fully deployed state and (B) fully stowed state. Figure reproduced from Hull (2013).

The square twist pattern contains a central square where the four vertices are the concurrent points of four identical spherical 4R linkages. Its cyclic configuration embodies rotational symmetry and the folds can be either concave (valley crease) or convex (mountain crease) (Silverberg et al., 2015). Greenberg et al. (2011) demonstrated that there are 2^{12} possible ways of assignment but only sixteen of them can be folded flat. Furthermore, if all the panels are required to be unbent throughout the folding process, there remains only one valid configuration, as given by Figure 2.8. Once the assembly is compressed diagonally, a rigid folding is expected until a smaller square has been reached at a fully flat state. Despite possessing the ability of folding flatly and rigidly, the utilization of the square twist pattern is still limited. This is due to the relatively small deployed-to-stowed ratio, which requires further research in response to this.

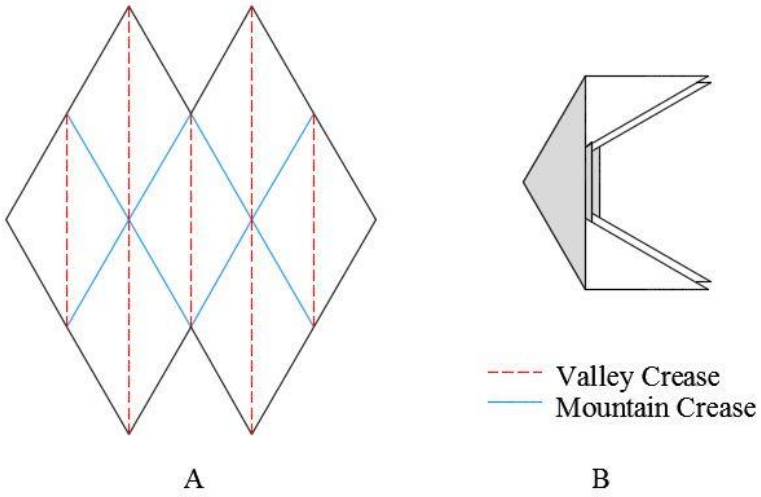

Figure 2.9 The diamond pattern in (A) the fully flat state and (B) the fully folded state.

Another commonly used tessellation is called the diamond pattern proposed by Yoshimura (1955). Consisting of a series of congruent obtuse triangles, this crease pattern is constructed by repetitively mirroring the panels with respect to the transverse creases. By merging the adjacent edges of the triangles, a symmetric configuration is produced, where each vertex is joined by six creases, as depicted in Figure 2.9-A. Essentially the pattern possesses three degrees of freedom. However, by imposing symmetry, its mobility can be reduced to one (De Temmerman et al., 2007). This allows the diamond pattern to be actuated by simply controlling a single input parameter. Furthermore, its elegant geometry enables the tessellation to be folded from an initially flat configuration to an arch-like intermediate state and it ends up with a flat stowed assembly (Figure 2.9-B). No in-plane deformation is required during the entire folding process. These desirable features allow the diamond pattern to be applied to a range of architectural structures such as makeshift shelters and deployable roofs.

2.4 Existing thickness accommodation techniques

Most origami-inspired applications are constructed with materials in which thickness cannot be neglected. Since origami patterns are primarily designed for paper with zero-thickness, they need to be modified for adoption in engineering applications. To take thickness into consideration, various approaches have been proposed. These can be categorised into four main types: the hinge shift (Hoberman, 2010), the tapered materials (Tachi, 2011), the offset panels (Edmondson et al., 2014) and the offset creases (Ku and Demaine, 2016). The four techniques, plus their strengths and weaknesses, are discussed next.

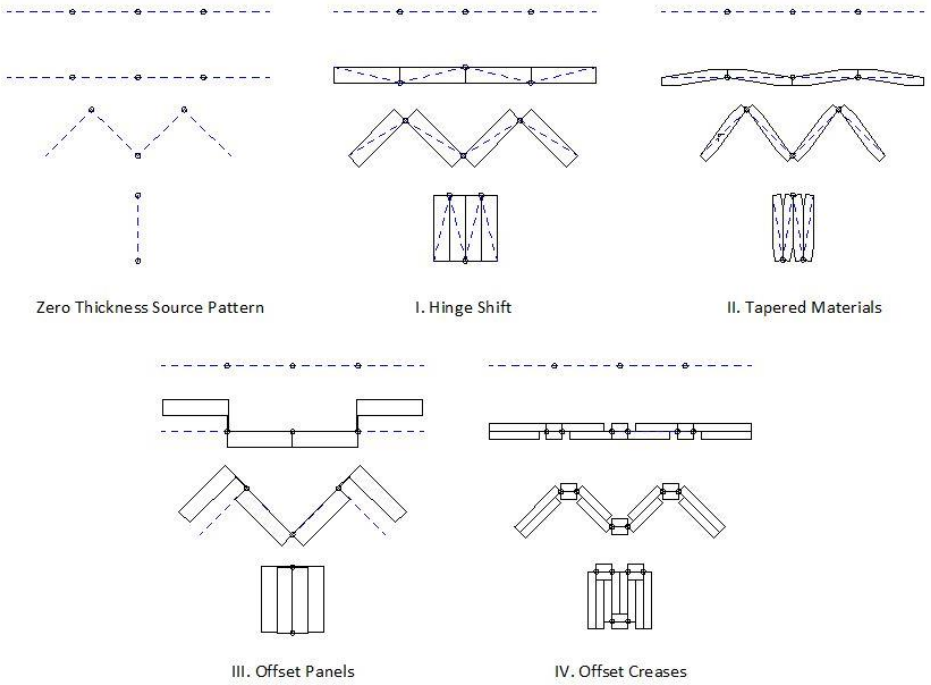

Figure 2.10 Some existing thickness accommodation techniques.

I. Hinge Shift

The hinge shift technique applies a spatial layout, whereby the rotational axes lie out of plane, i.e. shifting the hinges to the top or bottom of the panels depending on the direction of folding (Hoberman, 2010). As shown by Figure 2.10-I, the axes are offset by a distance

that equals to the material thickness in order to get rid of collisions. This strategy enables an assembly to fold rigidly without clearance between panels, which is useful in a one dimensional pattern. For higher dimensional assemblies, e.g. tessellations, full range motion is often restricted. Furthermore, as the folding lines are not coplanar, the kinematic motion is often different from that of its zero-thickness origami counterpart, and thus, the planar design approach does not apply. A recent approach extends this technique to origami tessellations (Chen, Peng and You, 2015). Nonetheless, rigorous thickness and angular conditions have to be satisfied to enable motion, setting geometrical restrictions to assemblies.

II. Tapered materials

Unlike the hinge shift method, the tapered materials technique locates the rotational axes on the same plane, which enables the same kinematic motion as that of their origami counterpart (Tachi, 2011). This allows the motion of thick panels to be predicted based on their source pattern. The thick panels can therefore be simply attached to both sides of the fold plane. As panels fold, self-intersection is avoided by trimming the materials in the collision zones and the shape of the panels depends on the dihedral angles of folding (Figure 2.10-II). While keeping the original kinematics provides a huge advantage over the hinge shift strategy, this method also presents an obvious drawback as the full range of motion is not achievable (Edmondson, 2015). Neither can it deploy to a fully flat plane, nor fold to a void-free compacted form. In addition, slanted and irregular panels can cause difficulties in fabrication for mass productions (Ku and Demaine, 2016).

III. Offset Panel

This approach locates the folding creases on the same joint plane, and shifts the panels away to a distance which equals to the thickness of them. A series of rigid extensions are

required to connect the offset panels to the joint plane (Edmondson, 2015). This design allows the folds to coincide with the zero-thickness source pattern, maintaining unchanged kinematics when applying to thick panels (Figure 2.10-III). Full range of motion is achievable and a compact stack without clearance is expected in the stowed position. Thus it presents a great potential for application in industry. However, extremely robust extensions are indispensable for physical models, or these slender standoffs will be particularly vulnerable to break.

IV. Offset Crease

The offset crease technique replaces each original crease with two parallel hinges without relying on a non-rigid membrane. The new folds are offset about the original fold in a symmetric way to accommodate the thickness, where offset distances depend on material thickness and geometry of assemblies (Ku and Demaine, 2016). This allows a rotation to be divided into two identical turns around the new creases. For example, to complete an 180˚ turn to reach the fully stowed state, each hinge needs to contribute a folding angle of 90˚ (Figure 2.10-IV). A two-layer layout is required as all rotational hinges need to be arranged in the middle plane, which can be deemed as the same fold plane of the origami source pattern. Although a portion of the panels need to be removed to avoid self-intersection, the thickness for the majority part remains constant. This suggests promising application prospects since a flat surface is expected when fully collapsed. Nonetheless, conversion to two new hinges nullifies the previous spherical linkage in which rotational axes fail to meet at a concurrent point. This means the assembly, in fact, becomes a spatial mechanism and its kinematic behaviour is not fully understood. Furthermore, the authors only introduced a little information on applying this newly proposed technique. The method to determine crease widths and the area of discarded polygons remains very vague and it cannot be generalised to other origami models. This leaves an open question for

researchers to examine what the rigorous trajectories of the motion should be, whether a kinematically equivalent pattern can be found, and how to generalise it to existing commonly-used origami patterns.

2.5 Inextensional wrapping

2.5.1 Past research

With the development of spacecraft, solar energy receivers have gained extensive research interests, which use solar radiation as a power source for spacecraft propulsion. This approach requires ultra large and light annular configurations to gain energy from space. However, receivers must be folded to a compact stowed form, during launch, before deploying to a flat state with a much larger surface area. This requires a thin, flat membrane to be wrapped cylindrically around a central hub with a high deployed-to-stowed ratio. In response to this requirement, a number of origami-based solutions have been proposed. Notable contributions include the crease patterns invented by Scheel (1974) and Cambridge Consultants (1989), as shown by Figure 2.11. The former applies a fold pattern consisting of a series of creases. The major creases lie approximately tangential to the imaginary central circle and the intermediate creases bisect the angles between the major folds. This innovative design allows a flexible annular membrane to be wrapped around a hub and deployed thereon. The latter creates a 24-sided central polygon with interchanged mountain/valley creases. The sail can be stowed to a 4-meter-diameter configuration for launch and deployed to a 276-meter-diameter disk when in orbit, enabling sufficient radiation to be collected. These fold patterns were designed for a flexible membrane with negligible thickness. Whereas some applications, such as solar panel arrays, demand thick, rigid materials to complete the same motion. This means the panels must neither undergo

any extensions nor create new folds during the entire folding process, posing new challenges for researchers.

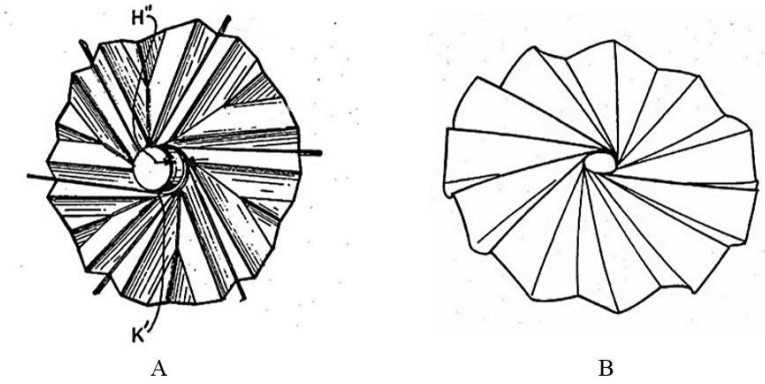

Figure 2.11 Wrapping patterns invented by (A) Scheel and (B) Cambridge consultants.

2.5.2 Basic design approach

A remarkable attempt has been made by Guest and Pellegrino (1992) who established a systemic strategy to design a fold pattern for inextensional wrapping. The approach started with the assumption that panels have zero-thickness and thus the layers remain coplanar when stacked. The conventionally circular hub is replaced by an *N*-sided polygon since straight sides preserve the flatness of the wrapping panels without creating any voids (Johnson and Yu, 1980). For a convex regular *N*-sided polygon, the inner angle η is given by

$$\eta = \pi(1 - \frac{2}{N}). \tag{2.22}$$

Taking the example of a hexagonal hub, the inner angle is thus equal to 120 °, as shown by Figure 2.12. 4R spherical linkages are formed at each vertex, which imparts loop-closure conditions. This suggests that no angular deficiency exists, thus the sum of angles around a vertex equals to 2π. Isometric panel heights are enforced to match the side length of the hub:

$$\mathrm{AB} = \mathrm{BC} = \mathrm{CD} = \mathrm{DE}. \tag{2.23}$$

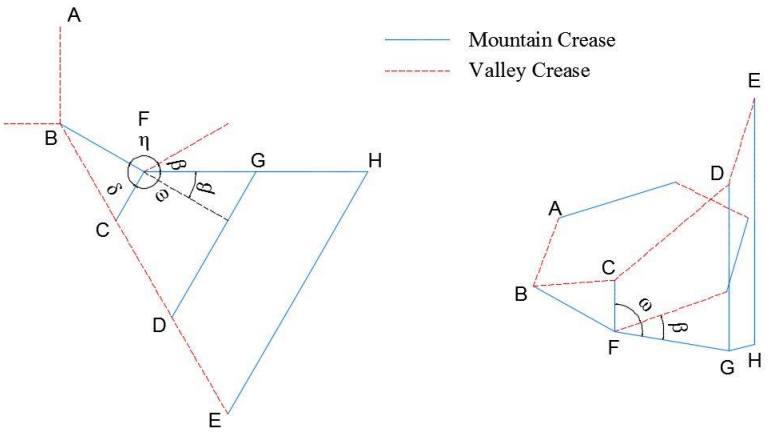

Figure 2.12 Topological details of fold pattern for N=6 in (A) flat and (B) wrapped states.

Additional conditions are provided by considering the fully stowed state, where CF, DG and EH must kept vertical. Therefore the following conditions must be fulfilled, which are

$$\beta = \frac{\pi}{n}, \omega = \left(\frac{1}{2} + \frac{1}{N}\right)\pi \text{ and } \delta = \frac{\pi}{2}. \tag{2.24}$$

Substitute *N*=6 to Eq. 2.22 and Eq. 2.24, the zero-thickness winding membrane with a hexagonal hub is obtained, as denoted by Ω_1 in Figure 2.13.

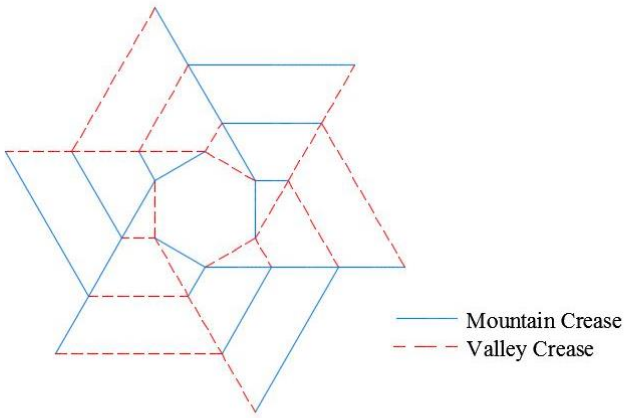

Ω_1

Figure 2.13 The winding membrane proposed by Guest and Pellegrino (1992).

2.5.3 Ability to fold rigidly

Despite being designed for inextensional wrapping, the above-mentioned fold pattern only fits well in the fully flat configuration and completely wrapped state, where no deformation is required to attain the desired position. Beyond these two states, no evidence has been provided that a rigid transition is achievable (Guest and Pellegrino, 2012). Although the physical models made of thin cardboard can be fold and deployed relative smoothly, still it can be seen that the facets have to be flexed to snap-through towards the two stable configurations. The non-rigid transition is also predicted by the mobility of the assembly. The Kutzbach criterion shows the mobility of this hexagonal pattern is -9. This suggests an inextensional transition is only possible if the rotational symmetry is sufficient to convert the configuration to an over-constrained mechanism. Albeit rigorous verification is required, it is not seen as an eligible prototype for applying to solar array panels in which the solar cell must not be flexed.

In order to suit the needs for developing solar panel arrays, two strategies have been proposed based on the basic pattern proposed by Guest and Pellegrino (Figure 2.14).

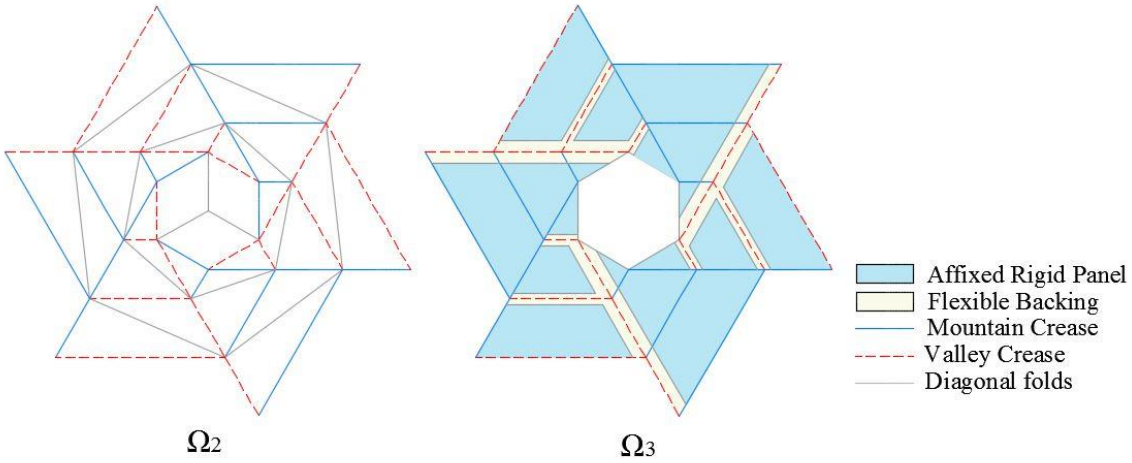

Figure 2.14 Modification schemes: (Ω_2) introducing diagonal folds and (Ω_3) applying membrane backing.

The first one triangulates all quadrilateral panels by adding extra diagonals to each of them, while the hexagonal hub is divided into three parallelograms (Ω_2) (Kumar and Pellegrino, 2000). It is conservatively conjectured that the rotational angles of the diagonals are less than five degrees, based on observations from the physical model. Therefore the newly introduced diagonal hinges might be stiffer than the original ones. These extra folds allow the non-triangular panels to fold slightly, thus providing enough flexibility to enable holistic rigidity. This was confirmed with a rigorous validation by tracking the full motion with the mechanical modelling method, as reviewed in Section 2.2. However, there are some points that are worth noting in relation to this desirable conclusion. First, the rigid transition relies on a slight rotation of the hinges within the hub, i.e. out-of-plane distortion is permitted. As the transition happens, these pin-jointed bars do not move simultaneously. Instead, the motion of the outer loop would not start until the motion of the inner loop is fully complete. A bifurcation point is expected when the outer loop completes its motion. The panels that are already folded undergo a tiny movement while the outer parts are moving, which in practice may cause some strain. The authors only proved the model's rigid foldability with two loops, but a giant solar structure requires multiple loops of triangles. This requires further investigation on extending the model to multiple layers to achieve a high deployed-to-stowed ratio. Finally, the addition of extra diagonals divides the panels into two parts, which maybe not be allowed for some particular applications.

The second strategy applies a thin, flexible backing on the bottom of the whole model. Some gaps are deliberately left at the valley creases for avoiding local self-intersections, as shown by Figure 2.14-Ω_3 (Zirbel et al., 2013). The width of a gap is chosen depending on the panel thickness and the designated rotational angles in the valley creases. The affixed panels can be kept undeformed throughout the transition, whereas, in fact, the whole crease pattern is no longer rigid. The membrane-like backing in the gaps is

significantly distorted to allow the stowage and deployment. Furthermore, the soft backing reduces the stiffness of the array, which demands an extra structure to support it. Therefore the flexible backing method is not desired for satellite sailing and deployment actuation.

2.5.4 Ability to accommodate material thickness

So far, three fold patterns has been proposed for the purpose of inextensional wrapping. As introduced earlier, all of the three patterns are based on the design approach introduced in Section 2.5.2. Thus they have same configuration at the fully folded states where the layers coincide with the verge of the central hexagon. However, this idealised configuration cannot be progressed to physical applications with finite thickness. Implementing the thickness accommodation technique (as reviewed in Section 2.4) alone failed to deal with this challenge. Guest and Pellegrino (1992) established a modified model which replaces the straight creases to deflected piecewise lines (Figure 2.15-A). This leads to a less compact helical form at the fully stowed state. This design applies a radial increase principal from the Archimedean spiral (Figure 2.15-B). The facets are separated with a constant rate between successive wrappings, allowing thickness to be added in the voids between panels (Figure 2.15-C).

However, this strategy only works for extremely thin material, like a membrane, as the space created is very limited. Also, its rigid foldability is yet to be validated. For applications with significant thickness, like solar cells, this model would not be suitable since unacceptable collisions can be expected. Consequently, a novel scheme to achieve rigid foldability and thickness-accommodating ability is acutely required.

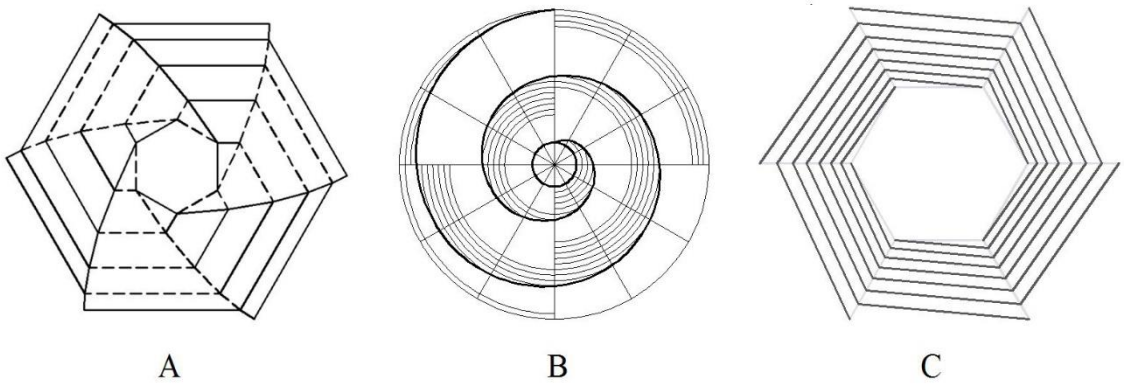

Figure 2.15 The design of the thickness-accommodation model.

2.6 Final remarks

Rigid Origami is an important division of origami which allows the assembly to transform from one configuration to another without deforming any faces or generating new creases. It provides rich inspiration for engineering design, as most deployable structures are made by stiff materials where internal movements only happen at the joints. This behaviour mimics the motion of a mechanical linkage which therefore allows the kinematics of rigid origami to be investigated by being treated as linkages. The mobility of origami structures can be obtained through the Kutzbach criterion, as a necessary but not sufficient condition to obtain static and kinematic determinacy. A range of methods have been proposed to mathematically study the motion of origami structures. Two approaches, the matrix method and the mechanical modelling method have been selected and thoroughly studied for use in different situations, with the pros and cons for each of them being discussed.

The kinematics of single-vertex origami has been investigated, with the examples of three key units: spherical linkages of 4R, 5R and 6R. Most commonly used origami tessellations are constituted via combination of these three linkages. Examples include the Miura-ori, the square twist and the diamond pattern. All assemblies contain a series of identical spherical linkages and can be actuated with a single degree of freedom.

Mathematically, origami is stipulated as paper where thickness can be discarded. However, origami-inspired physical implementations will inevitably have considerable thickness that needs to be taken into account within pattern design. Various strategies have been proposed and some of them are able to retain the original kinematics from their parent origami model. Ku and Demaine (2016) came up with a promising method called the offset crease technique, which means the creases are offset from their original positions. This method presents great application potential as a flat surface is expected when fully deployed. However, as a newly invented technique, its kinematics and adopting approach are yet to be understood, leaving a pivotal challenge for engineers and researchers.

A noteworthy application of origami is the deployable solar receivers of a spacecraft, such as solar sail or solar panel arrays. The receivers are required to retract for rocket transportation and deploy to a huge disk once in orbit. A number of origami-based solutions are capable of doing so by wrapping a flexible thin membrane cylindrically around the hub, but none of them can achieve an inextensional deployment. Whereas some particular applications, e.g. brittle solar panels, demand rigid and thick material to be used, presenting an acute need of eligible solutions. Guest and Pellegrino (1992) have established a systematic way of discovering inextensional wrapping patterns. The winding membrane guarantees the panels are not stretched in the fully flat and stowed state, but no rigorous validation has been made to confirm a rigid transition between the two states. Two derivatives from the winding membrane, proposed by Kumar and Pellegrino (2000) and Zirbel et al. (2013), have been studied explicitly. Despite coming close to a practical solution, neither model possesses the ability to fold rigidly and the ability to accommodate material thickness simultaneously, leaving a challenging gap for researchers.

3. Rigid Origami of Thick Panels

In this chapter, a newly proposed thickness-accommodating method for rigid origami, the offset crease technique, is further developed. As reviewed in Section 2.4, the kinematics and implementation procedure of this promising method is yet to be understood.

This chapter starts with a comprehensive analysis which precisely defines the trajectories of motion. This is done by making comparisons between kinematics of a single-vertex spatial linkage, which is constructed through this technique, with that of its original spherical counterpart. A detailed strategy for adopting the technique then follows, with the aid of a demonstrative example, the Miura-ori. The strategy, proven to be adequate for general rigid origami tessellations, is applied to fabricate a number of eligible physical models. The ineligible patterns are then identified. Finally, a novel tessellation with better performance in thickness accommodation is elaborated on to conclude the section.

3.1 Comparisons between spatial linkages and the corresponding spherical linkages

The majority of commonly used tessellations, for example, the traditional Miura-ori pattern, square twist pattern and diamond pattern are generally formed by vertices with four, five or six fold lines. Therefore, these three types of single-vertex patterns are selected to be studied in this section.

As reviewed earlier, a single apex of rigid origami with four creases can be treated as a 4R spherical linkage with all axes of revolute joints meet at a concurrent point, as shown by grey dot-dash lines in Figure 3.1. The offset crease technique, however, requires each of the original creases to be converted to two parallel symmetric folds, as noted by blue and red lines. Besides that, the rotation of creases from each symmetric pair must be kept

identically throughout the entire motion. This could be done by introducing interlocking gears for the two symmetric creases, and thus the mobility of each pair is reduced to one. Therefore, we have the following conditions,

$$\theta_1 = \theta_2, \theta_3 = \theta_4, \theta_5 = \theta_6 \text{ and } \theta_7 = \theta_8, \tag{3.1}$$

where θ's are rotational angles about their corresponding Z creases.

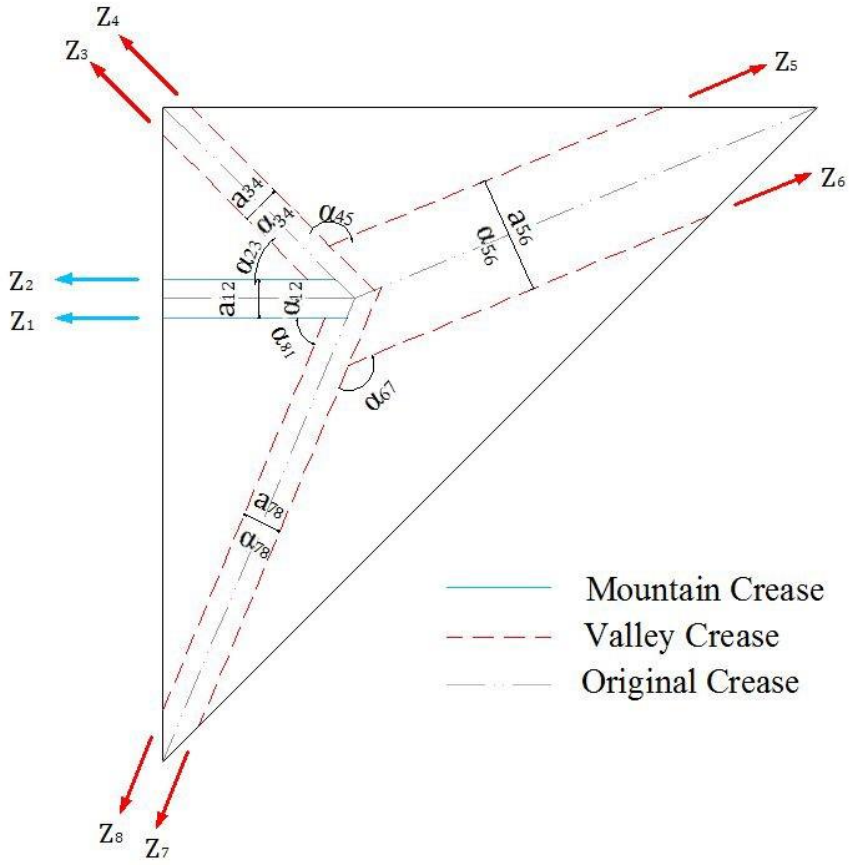

Figure 3.1 The crease pattern of an 8R Spatial Linkage.

Each new crease moves away from its previous position, and thus the distances between Z axes, also known as crease widths a_{ij}, are no longer zero. The relationship between these distances for the assembly in Figure 3.1 is

$$a_{12}+a_{34}+a_{78} = a_{56}. \tag{3.2}$$

The offset distances, equivalent to a half of crease widths, are dependent on the material thickness and the configuration of assemblies. The optimized design should aim for a

minimum offset distance to achieve the most compact form in the fully stowed state. The method for determining a_{ij} for each crease will be given later in this section.

The existence of non-zero a_{ij} makes the creases fail to meet at a common point and the original flat-foldable 4R spherical linkage is thus transformed to an 8R spatial linkage (Figure 3.1). Despite this, the offset creases remain parallel to their parent creases,

thus the sum of sector angles remains unchanged, i.e.

$$\alpha_{23} + \alpha_{45} + \alpha_{67} + \alpha_{81} = 2\pi. \tag{3.3}$$

Flat foldability requires the condition

$$\alpha_{23} + \alpha_{67} = \alpha_{45} + \alpha_{81} = \pi \tag{3.4}$$

to be fulfilled. This linkage forms a closed loop with eight links, and applying DH notation gives

$$T_{12}T_{23}T_{34}T_{45}T_{56}T_{67}T_{78}T_{81} = I_4. \tag{3.5}$$

where, for example,

$$T_{12} = \begin{bmatrix} \cos\theta_1 & -\cos\alpha_{12}\sin\theta_1 & \sin\alpha_{12}\mathrm{Sin}\theta_1 & a_{\alpha_{12}}\cos\theta_1 \\ \sin\theta_1 & \cos\alpha_{12}\cos\theta_1 & -\sin\alpha_{12}\cos\theta_1 & a_{\alpha_{12}}\sin\theta_1 \\ 0 & \sin\alpha_{12} & \cos\alpha_{12} & 0 \\ 0 & 0 & 0 & 1 \end{bmatrix}. \tag{3.5a}$$

Alternatively, a simple conversion can produce a more useful form. There is

$$T_{12}T_{23}T_{34}T_{45}T_{56}T_{67}T_{78}T_{81}T_{81}^{-1}T_{78}^{-1}T_{67}^{-1}T_{56}^{-1} = T_{81}^{-1}T_{78}^{-1}T_{67}^{-1}T_{56}^{-1}. \tag{3.6}$$

Rearranging Eq. 3.6 yields

$$T_{12}T_{23}T_{34}T_{45} = T_{18}T_{87}T_{76}T_{65} \tag{3.7}$$

Multiplication of the matrices on both side generates sixteen equations. A complete set of the equations is given in Appendix A. For convenience, the elements (1.3), (2.3), (3.3) and (3.1) are selected from Appendix A to be further investigated, which are

$$\begin{aligned}\cos\alpha_{45}\sin\alpha_{23}\sin(2\theta_1) + \cos\alpha_{23}\cos(2\theta_3)\sin\alpha_{45}\sin(2\theta_1) + \\ \cos(2\theta_1)\sin\alpha_{45}\sin(2\theta_3) = \sin\alpha_{23}\sin(2\theta_7),\end{aligned} \tag{3.8}$$

$$\begin{aligned}-\cos\alpha_{45}\cos(2\theta_1)\sin\alpha_{23} - \cos\alpha_{23}\cos(2\theta_1)\cos(2\theta_3)\sin\alpha_{45} + \\ \sin\alpha_{45}\sin(2\theta_1)\sin(2\theta_3) = -\cos\alpha_{45}\cos(2\theta_7)\sin\alpha_{23} - \cos\alpha_{23}\sin\alpha_{45},\end{aligned} \tag{3.9}$$

$$\begin{aligned}\cos\alpha_{23}\cos\alpha_{45} - \cos(2\theta_3)\sin\alpha_{23}\sin\alpha_{45} \\ = \cos\alpha_{23}\cos\alpha_{45} - \cos(2\theta_7)\sin\alpha_{23}\sin\alpha_{45},\end{aligned} \tag{3.10}$$

$$\begin{aligned}\sin\alpha_{23}\sin(2\theta_3) = -\cos\alpha_{45}\sin\alpha_{23}\sin(2\theta_5) \\ -\cos\alpha_{23}\cos(2\theta_7)\sin\alpha_{45}\sin(2\theta_5) + \cos(2\theta_5)\sin\alpha_{45}\sin(2\theta_7).\end{aligned} \tag{3.11}$$

There are two main reasons for selecting the above elements. Firstly, these elements have relatively simple and non-trivial forms among all elements. Also, there exists similarity in forms with the elements used by Chen, Peng and You (2015) for deriving the relationship between rotations for the parent 4R spherical linkage, which means comparisons can be conducted easily.

From Eq. 3.10, it can be observed that

$$\cos(2\theta_3) = \cos(2\theta_7). \tag{3.12}$$

Both θ_3 and θ_7 represent rotational angles of valley creases, which means their range of angles are $[-\frac{\pi}{2}, 0]$, thus

$$\theta_3 = \theta_7. \tag{3.13}$$

The boudary value $-\frac{\pi}{2}$ is due to the special configuration of the pattern where each revolute joint from a parallel pair only needs to complete a half of the entire rotation. The trigonometric transformations

$$\sin(2\theta) = \frac{2\tan\theta}{\tan^2\theta + 1} \tag{3.14}$$

$$\cos(2\theta) = \frac{1 - \tan^2\theta}{1 + \tan^2\theta} \tag{3.15}$$

are then applied to Eqs. 3.8 and 3.9, respectively. For Eq. 3.9, there is

$$\begin{aligned}\sin\alpha_{45}\cos\alpha_{23} + \cos\alpha_{45}\sin\alpha_{23}\frac{\tan^2\theta_1 - 1}{\tan^2\theta_1 + 1} - \cos\alpha_{45}\sin\alpha_{23}\frac{\tan^2\theta_3 - 1}{\tan^2\theta_3 + 1} \\ + \frac{2\tan\theta_3}{\tan^2\theta_3 + 1}\frac{2\tan\theta_3}{\tan^2\theta_3 + 1}\sin\alpha_{45} - \sin\alpha_{45}\cos\alpha_{23}\frac{\tan^2\theta_1 - 1}{\tan^2\theta_1 + 1}\frac{\tan^2\theta_3 - 1}{\tan^2\theta_3 + 1} = 0.\end{aligned} \tag{3.16}$$

Simplifying Eq. 3.16, there is

$$\begin{aligned}\sin\alpha_{45}\cos\alpha_{23}(\tan^2\theta_1 + \tan^2\theta_3) + \cos\alpha_{45}\sin\alpha_{23}(\tan^2\theta_1 \\ -\tan^2\theta_3) + 2\tan\theta_1\tan\theta_3\sin\alpha_{45} = 0\end{aligned} \tag{3.17}$$

Rearranging Eq. 3.17 yields

$$\sin(\alpha_{45} + \alpha_{23})\frac{\tan^2\theta_1}{\tan^2\theta_3} + 2\sin\alpha_{45}\frac{\tan\theta_1}{\tan\theta_3} + \sin(\alpha_{45} - \alpha_{23}) = 0. \tag{3.18}$$

Solving the quadratic equation gives

$$\frac{\tan\theta_1}{\tan\theta_3} = \frac{-2\sin\alpha_{45} \pm \sqrt{4\sin^2\alpha_{45} - 4\sin(\alpha_{45} + \alpha_{23})\sin(\alpha_{45} - \alpha_{23})}}{2\sin(\alpha_{45} + \alpha_{23})}. \tag{3.19}$$

Adopting the trigonometric equation

$$\sin(\alpha_{23} + \alpha_{45})\sin(\alpha_{23} - \alpha_{45}) = \sin^2\alpha_{23} - \sin^2\alpha_{45} \tag{3.20}$$

allows Eq. 3.19 to be further simplified to

$$\frac{\tan\theta_1}{\tan\theta_3} = \frac{-2\sin\alpha_{45} \pm \sqrt{4\sin^2\alpha_{45} - 4\sin^2\alpha_{45} + 4\sin^2\alpha_{23}}}{2\sin(\alpha_{45} + \alpha_{23})}. \tag{3.21}$$

Hence the answer could be

$$\frac{\tan\theta_1}{\tan\theta_3} = \frac{-\sin\alpha_{45} \pm \sin\alpha_{23}}{\sin(\alpha_{45} + \alpha_{23})}. \tag{3.22}$$

This answer must be unique and satisfy all sixteen equations. To determine the exact solution, Eq. 3.8 is chosen and substituted with Eqs. 3.14 and 3.15, which gives

$$\begin{aligned} -\sin\alpha_{45}\frac{2\tan\theta_3}{\tan^2\theta_3 + 1}\frac{\tan^2\theta_1 - 1}{\tan^2\theta_1 + 1} - \sin\alpha_{45}\cos\alpha_{23}\frac{2\tan\theta_1}{\tan^2\theta_1 + 1}\frac{\tan^2\theta_3 - 1}{\tan^2\theta_3 + 1} \\ +\cos\alpha_{45}\sin\alpha_{23}\frac{2\tan\theta_1}{\tan^2\theta_1 + 1} - \sin\alpha_{23}\frac{2\tan\theta_3}{\tan^2\theta_3 + 1} = 0. \end{aligned} \tag{3.23}$$

Rearranging Eq. 3.23, we have

$$\begin{aligned} -2\sin\alpha_{45}\tan\theta_3(\tan^2\theta_1 - 1) - 2\sin\alpha_{45}\cos\alpha_{23}\tan\theta_1(\tan^2\theta_3 - 1) \\ +2\cos\alpha_{45}\sin\alpha_{23}\tan\theta_1(\tan^2\theta_3 + 1) - 2\sin\alpha_{23}\tan\theta_3(\tan^2\theta_1 + 1) = 0. \end{aligned} \tag{3.24}$$

It can be fully expanded to

$$\begin{aligned} \tan\theta_1\tan^2\theta_3\frac{\sin^2\alpha_{23} - \sin^2\alpha_{45}}{\sin(\alpha_{23} + \alpha_{45})} + \tan\theta_1\cos\alpha_{45}\sin\alpha_{23} \\ -\tan\theta_3\sin\alpha_{23}\tan^2\theta_1 - \tan\theta_3\sin\alpha_{23} - \sin\alpha_{45}\tan\theta_3\tan^2\theta_1 \\ +\sin\alpha_{45}\tan\theta_3 + \sin\alpha_{45}\cos\alpha_{23}\tan\theta_1 = 0. \end{aligned} \tag{3.25}$$

To get a more useful form, Eq. 3.25 can be rewritten as

$$\begin{aligned} (\cos\alpha_{45}\sin\alpha_{23} + \sin\alpha_{45}\cos\alpha_{23} - \tan\theta_1\tan\theta_3\sin\alpha_{23} \\ -\tan\theta_1\tan\theta_3\sin\alpha_{45})\left(\tan\theta_1 - \frac{\sin\alpha_{23} - \sin\alpha_{45}}{\cos\alpha_{45}\sin\alpha_{23} + \sin\alpha_{45}\cos\alpha_{23}}\tan\theta_3\right) = 0 \end{aligned} \tag{3.26}$$

Simplifying Eq. 3.26 yields

$$(\sin(\alpha_{23}+\alpha_{45})-\tan\theta_1\tan\theta_3(\sin\alpha_{23}+\sin\alpha_{45}))(\tan\theta_1-\frac{\sin\alpha_{23}-\sin\alpha_{45}}{\sin(\alpha_{23}+\alpha_{45})}\tan\theta_3)=0 \tag{3.27}$$

Comparing Eq. 3.27 with Eq. 3.22, it can be noted that

$$\frac{\tan\theta_1}{\tan\theta_3}=\frac{\sin\alpha_{23}-\sin\alpha_{45}}{\sin(\alpha_{45}+\alpha_{23})} \tag{3.28}$$

satisfies both equations. According to trigonometric identities, there are

$$\sin\alpha_{23}-\sin\alpha_{45}=2\cos(\frac{\alpha_{23}+\alpha_{45}}{2})\sin(\frac{\alpha_{23}-\alpha_{45}}{2}) \tag{3.29}$$

and

$$\sin(\alpha_{23}+\alpha_{45})=2\sin\left(\frac{\alpha_{23}+\alpha_{45}}{2}\right)\cos\left(\frac{\alpha_{23}+\alpha_{45}}{2}\right). \tag{3.30}$$

Substituting Eqs. 3.25 and 3.26 to Eqs. 3.24 yields

$$\frac{\tan\theta_1}{\tan\theta_3}=\frac{2\cos(\frac{\alpha_{23}+\alpha_{45}}{2})\sin(\frac{\alpha_{23}-\alpha_{45}}{2})}{2\sin\left(\frac{\alpha_{23}+\alpha_{45}}{2}\right)\cos\left(\frac{\alpha_{23}+\alpha_{45}}{2}\right)}=\frac{\sin(\frac{\alpha_{23}-\alpha_{45}}{2})}{\sin(\frac{\alpha_{23}+\alpha_{45}}{2})}. \tag{3.31}$$

Similarly, for Eq. 3.11, Eq. 3.13 is substituted to eliminate θ_7. Applying trigonometric transformation gives

$$\sin\alpha_{23}\frac{2\tan\theta_3}{\tan^2\theta_3+1}=-\cos\alpha_{45}\sin\alpha_{23}\frac{2\tan\theta_5}{\tan^2\theta_5+1}$$
$$-\cos\alpha_{23}\frac{1-\tan^2\theta_3}{1+\tan^2\theta_3}\sin\alpha_{45}\frac{2\tan\theta_5}{\tan^2\theta_5+1}+\frac{1-\tan^2\theta_5}{1+\tan^2\theta_5}\sin\alpha_{45}\frac{2\tan\theta_3}{\tan^2\theta_3+1}. \tag{3.32}$$

Following the same simplification process of Eq. 3.8 yields an equation with a similar form to Eq. 3.31, which is

$$\frac{\tan\theta_5}{\tan\theta_3}=-\frac{\sin\left(\frac{\alpha_{23}-\alpha_{45}}{2}\right)}{\sin\left(\frac{\alpha_{23}+\alpha_{45}}{2}\right)}. \tag{3.33}$$

By comparison we found

$$\frac{\tan\theta_5}{\tan\theta_3} = -\frac{\tan\theta_1}{\tan\theta_3}. \tag{3.34}$$

Therefore it can be concluded that

$$-\theta_1 = \theta_5, \tag{3.35}$$

where

$$0 \leq \theta_1 \leq \frac{\pi}{2} \text{ (Mountain Crease)} \tag{3.36}$$

$$-\frac{\pi}{2} \leq \theta_5 \leq 0 \text{ (Valley Crease).} \tag{3.37}$$

Due to the inherent feature of the offset crease technique, an original crease is replaced by two identically parallel ones to complete a same turn angle. Therefore a turn angle of a 4R spherical linkage is twice of that of an 8R spatial linkage, which means

$$\theta_1^{4R} = 2\theta_1^{8R} \text{ and } \theta_2^{4R} = 2\theta_3^{8R}. \tag{3.38}$$

Given this condition, it can be seen that the results of an 8R spatial linkage (Eqs. 3.13, 3.33 and 3.35) exactly tally with those of a spherical 4R linkage concluded by Chen, Peng and You (2015) (Eqs. 2.15a, 2.15b and 2.16), as reviewed in Section 2.3.1. The relationships between rotations θ_1^{4R} (or $2\theta_1^{8R}$) and θ_2^{4R} (or $2\theta_3^{8R}$) are then plotted in Figure 3.2 to track the full range of motions. The curves I, II and III represent the relationships based on three groups of sector angles. The curves of the 8R spatial linkage overlap with the original one from the 4R counterpart, which means this modified crease pattern is kinematically equivalent to its origami source pattern throughout the folding process. Consequently, it can be concluded that adding finite thickness to a flat-foldable four-crease single vertex origami pattern by offsetting creases does not alter its kinematics regardless of how thick the attached panels are.

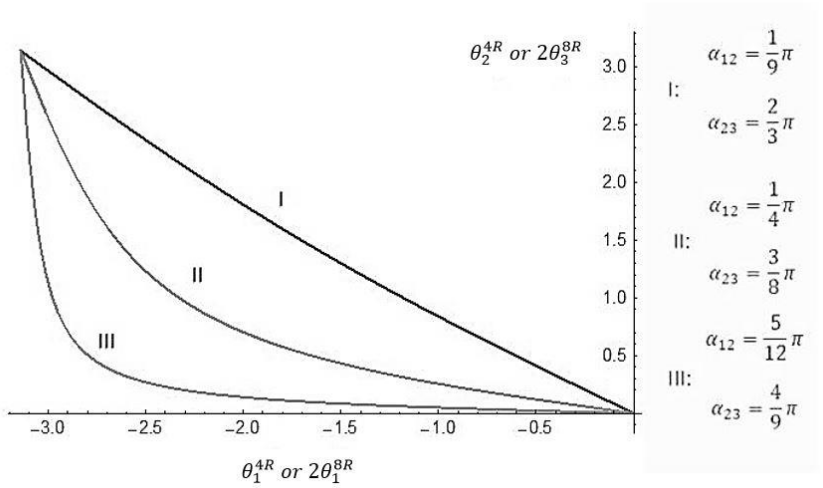

Figure 3.2 Relationships between rotations for the 4R spherical linkage and the 8R spatial linkage.

The positive result from the 4R spherical linkage provides an inspiration to extend the comparison to the spherical linkages containing five and six revolute joints. There exists a considerable number of 5R and 6R spherical linkages, and two particular configurations from each category are selected where their trajectories of motion are clearly defined by Chen, Pen and You (2015), as reviewed in Section 2.3.1.

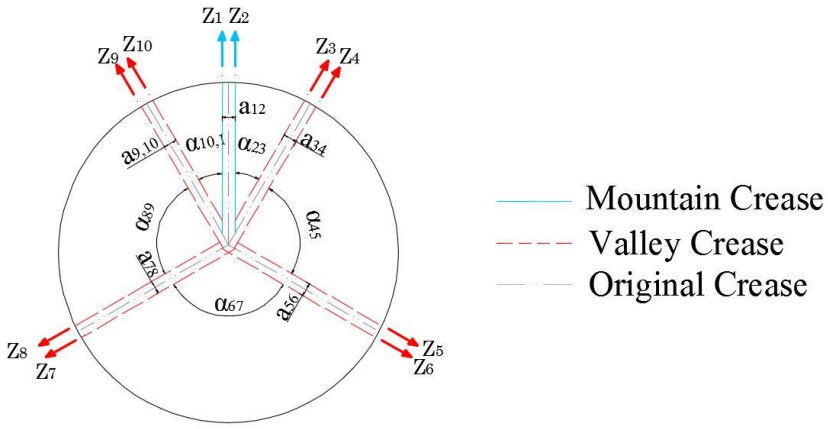

Figure 3.3 The 10R spatial linkages.

Through the offset crease technique, the two specific 5R and 6R spherical linkages are transformed to a 10R (Figure 3.3) and 12R (Figure 3.4) spatial linkages, respectively, to accommodate material thickness. The mobility of the spatial linkage is halved to match

that of their parent assemblies by imposing symmetry, i.e. ensuring rotations of revolute joints in each pair to be identical.

For the 10R spatial linkage, the pairs of rotation angles are

$$\theta_1 = \theta_2, \theta_3 = \theta_4, \theta_5 = \theta_6$$
$$\theta_7 = \theta_8 \text{ and } \theta_9 = \theta_{10}. \tag{3.39}$$

The angular configuration remains unchanged from its zero-thickness source pattern, so we have

$$\alpha_{23} = \alpha_{10,1}, \alpha_{45} = \alpha_{89} = \frac{\pi}{2}, \alpha_{67} = \pi - 2\alpha_{12}, \tag{3.40}$$

$$\theta_3 = \theta_9, \theta_5 = \theta_7. \tag{3.41}$$

The loop-closure condition gives

$$T_{12}T_{23}T_{34}T_{45}T_{56}T_{67}T_{78}T_{89}T_{9,10}T_{10,1} = I_4. \tag{3.42}$$

Similar to the 8R spatial linkage, Eq. 3.42 can be rearranged as

$$T_{12}T_{23}T_{34}T_{45}T_{56}T_{67} = T_{1,10}T_{10,9}T_{98}T_{87}. \tag{3.43}$$

Expanding the matrices multiplication yields sixteen equations, and the completed results are put in Appendix B. For convenience the elements (2.1) and (3.3) in Appendix B are selected for further investigation, which are

$$\begin{gathered}\cos(2\theta_5)(\sin(2\theta_1)\cos(2\theta_3) + \cos\alpha_{23}\cos(2\theta_1)\sin(2\theta_3)) \\ -\sin\alpha_{23}\cos(2\theta_1)\sin(2\theta_5) = -\cos\alpha_{23}\sin(2\theta_3)\cos(2\theta_5) + \sin\alpha_{23}\sin(2\theta_5)\end{gathered} \tag{3.44}$$

$$\begin{gathered}\cos(2\alpha_{23})\sin\alpha_{23}\cos(2\theta_3) - \sin(2\alpha_{23})\cos\alpha_{23}\cos(2\theta_5) \\ +\sin(2\alpha_{23})\sin\alpha_{23} = -\sin\alpha_{23}\cos(2\theta_3)\end{gathered} \tag{3.45}$$

Similar to the 8R linkage, Eqs. 3.14 and 3.15 are substituted so the Eqs. 3.44 and 3.45 become

$$(\tan^2\theta_5 - 1)(2\tan\theta_1(\tan^2\theta_3 - 1) + \cos\alpha_{23}(\tan^2\theta_1 - 1)2\tan\theta_3) \\ -\sin\alpha_{23}(\tan^2\theta_1 - 1)2\tan\theta_5(\tan^2\theta_3 + 1) - \cos\alpha_{23}2\tan\theta_3(\tan^2\theta_5 \\ -1)(\tan^2\theta_1 + 1) - \sin\alpha_{23}2\tan\theta_5(\tan^2\theta_1 + 1)(\tan^2\theta_3 + 1) = 0 \quad (3.46)$$

$$\cos(2\alpha_{23})\sin\alpha_{23}(1 + \tan^2\theta_5)(1 - \tan^2\theta_3) \\ -\sin(2\alpha_{23})\cos\alpha_{23}(1 - \tan^2\theta_5)(1 + \tan^2\theta_3) \\ +4\sin(2\alpha_{23})\sin\alpha_{23}\tan\theta_3\tan\theta_5 + \sin\alpha_{23}\cos(2\theta_3) = 0 \quad (3.47)$$

For Eq. 3.47, the double-angle formulas,

$$\cos(2\alpha) = 2\cos^2\alpha - 1, \quad (3.48)$$

$$\sin(2\alpha) = 2\sin\alpha\cos\alpha, \quad (3.49)$$

are utilised, so we have

$$(2\cos^2\alpha_{23} - 1)\sin\alpha_{23}(1 + \tan^2\theta_5)(1 - \tan^2\theta_3) - 2\sin\alpha_{23}\cos^2\alpha_{23}(1 \\ -\tan^2\theta_5)(1 + \tan^2\theta_3) + 8\sin^2\alpha_{23}\cos\alpha_{23}\tan\theta_3\tan\theta_5 + \sin\alpha_{23}\cos(2\theta_3) = 0 \quad (3.50)$$

Simplifying Eq. 3.50 yields

$$4\sin\alpha_{23}\cos\alpha_{23}(-\cos\alpha_{23}\tan^2\theta_3 + 2\sin\alpha_{23}\tan\theta_3\tan\theta_5 + \cos\alpha_{23}\tan^2\theta_5) = 0. \quad (3.51)$$

Solving Eq. 3.51 gives

$$\frac{\tan\theta_5}{\tan\theta_3} = \frac{\pm 1 - \sin\alpha_{23}}{\cos\alpha_{23}} \quad (3.52)$$

Since the rotations θ_3 and θ_5 are both around valley crease, they have same signs. Therefore, we have

$$\frac{\tan\theta_5}{\tan\theta_3} = \frac{1 - \sin\alpha_{23}}{\cos\alpha_{23}}. \quad (3.53)$$

Substituting Eq. 3.53 into Eq. 3.46 eliminates θ_5, which is

$$\frac{1}{(\tan^2\theta_1+1)(\tan^2\theta_3+1)\left(1+\left(\frac{1-\sin\alpha_{23}}{\cos\alpha_{23}}\right)^2\tan^2\theta_3\right)}\times\left(1-\left(\frac{1-\sin\alpha_{23}}{\cos\alpha_{23}}\right)^2\tan^2\theta_3\right)$$

$$\times\left(2(1-\tan^2\theta_3)\tan\theta_1+4\tan\theta_1\cos\alpha_{23}\right)-4\frac{1-\sin\alpha_{23}}{\cos\alpha_{23}}\sin\alpha_{23}(1+\tan^2\theta_3))=0. \tag{3.54}$$

Rearranging Eq. 3.54 produces a more useful form,

$$\frac{E_1E_2}{E_3}=0, \tag{3.55}$$

where

$$E_1=2(\tan^2\theta_3-1), \tag{3.56a}$$

$$E_2=\cos^2\alpha_{23}\tan\theta_1+\tan\theta_1\tan^2\theta_3(\cos^2\alpha_{23}+2\sin\alpha_{23}-2)$$
$$+2\cos\alpha_{23}\tan\theta_3-2\cos\alpha_{23}\sin\alpha_{23}\tan\theta_3, \tag{3.56b}$$

$$E_3=(\tan^2\theta_1+1)(\tan^2\theta_3+1)(\sin\alpha_{23}-1)$$
$$(1+\sin\alpha_{23}-\sin\alpha_{23}\tan^2\theta_3+\tan^2\theta_3). \tag{3.56c}$$

Eq. 3.55 requires at least one factor equals to zero. Equating E_1 to zero requires the value of θ_3 to be $\pm45°$, which is not attainable for this 10R linkage. This means E_2 must be zero, which is

$$\cos^2\alpha_{23}\tan\theta_1+\tan\theta_1\tan^2\theta_3(\cos^2\alpha_{23}+2\sin\alpha_{23}-2)$$
$$+2\cos\alpha_{23}\tan\theta_3-2\cos\alpha_{23}\sin\alpha_{23}\tan\theta_3=0. \tag{3.57}$$

Rearranging Eq. 3.57 gives the relationship between θ_1 and θ_3, so we have

$$\tan^2\theta_3-\frac{2\tan\theta_3}{\tan\theta_1}\frac{\cos\alpha_{23}}{1-\sin\alpha_{23}}-\frac{1+\sin\alpha_{23}}{1-\sin\alpha_{23}}=0. \tag{3.58}$$

By comparison it can be found that Eqs. 3.53 and 3.58 precisely match Eqs. 2.18 and 2.19 as the sum of rotations in each pair is two times of that from a single parallel joint.

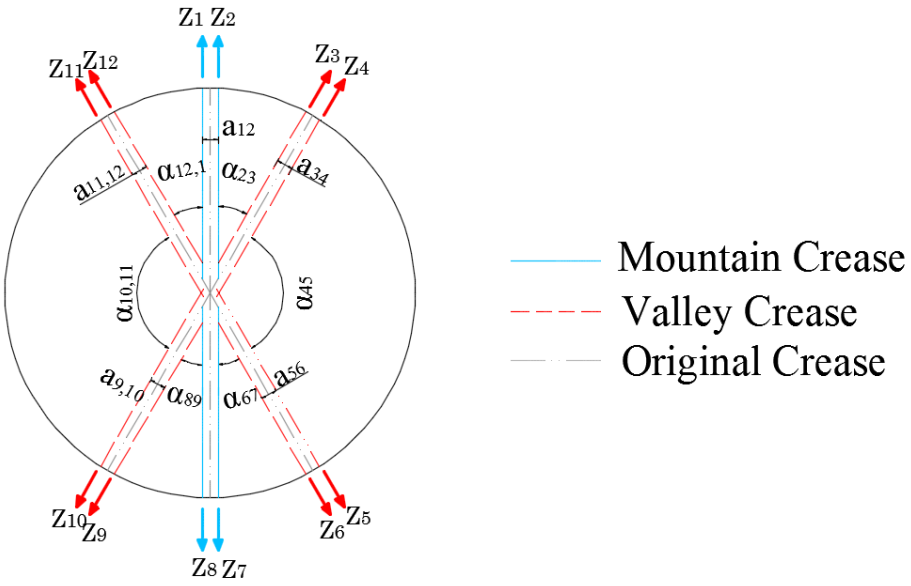

Figure 3.4 The 12R spatial linkages

The same algorithm is applied to the 12R spatial linkage. Again the symmetric pairs of rotation angles are imposed as

$$\theta_1 = \theta_2, \theta_3 = \theta_4, \theta_5 = \theta_6$$
$$\theta_7 = \theta_8, \theta_9 = \theta_{10} \text{ and } \theta_9 = \theta_{10}. \tag{3.59}$$

The angular configuration is kept identical to its parent origami pattern, which is

$$\alpha_{23} = \alpha_{67} = \alpha_{89} = \alpha_{12,1}, \alpha_{45} = \alpha_{10,11} = \pi - 2\alpha_{23}, \tag{3.60}$$

$$\theta_1 = \theta_4, \theta_2 = \theta_3 = \theta_5 = \theta_6. \tag{3.61}$$

The loop-closure equation gives

$$T_{12}T_{23}T_{34}T_{45}T_{56}T_{67}T_{78}T_{89}T_{9,10}T_{10,11}T_{11,12}T_{12,1} = I_4. \tag{3.62}$$

Similarly, it can be rearranged as

$$T_{12}T_{23}T_{34}T_{45}T_{56}T_{67} = T_{1,12}T_{12,11}T_{11,10}T_{10,9}T_{98}T_{87}. \tag{3.63}$$

For convenience, the completed results of Eq. 3.63 are listed separately in Appendix C. From the element (1.3) in Appendix C, we obtain

$$2\sin\alpha_{23}(\cos^2\alpha_{23} + \cos(2\theta_3) - \cos^2\alpha_{23}\cos(2\theta_3))(-\cos\alpha_{23}\sin(2\theta_1) + \cos(2\theta_1)\sin(2\theta_3) + \cos\alpha_{23}\cos(2\theta_3)\sin(2\theta_1)) = 2\sin\alpha_{23}\sin(2\theta_3)(\cos^2\alpha_{23} + \cos(2\theta_3) - \cos^2\alpha_{23}\cos(2\theta_3)) \quad (3.64)$$

Again, Eqs. 3.14 and 3.15 is substituted into Eq. 3.64, which gives

$$2\sin\alpha_{23}(\cos^2\alpha_{23} + \frac{1-\tan^2\theta_3}{1+\tan^2\theta_3} - \cos^2\alpha_{23}\frac{1-\tan^2\theta_3}{1+\tan^2\theta_3})(-\frac{2\tan\theta_3}{1+\tan^2\theta_3} - \cos\alpha_{23}\frac{2\tan\theta_1}{1+\tan^2\theta_1} + \frac{1-\tan^2\theta_1}{1+\tan^2\theta_1}\frac{2\tan\theta_3}{1+\tan^2\theta_3} + \cos\alpha_{23}\frac{1-\tan^2\theta_3}{1+\tan^2\theta_3}\frac{2\tan\theta_1}{1+\tan^2\theta_1}) = 0 \quad (3.65)$$

Simplifying Eq. 3.65 yields

$$8\sin\alpha_{23}\tan\theta_1\tan\theta_3(\tan\theta_1 + \tan\theta_3\cos\alpha_{23})(\tan^2\theta_3\cos(2\alpha_{23}) + 1) = 0. \quad (3.66)$$

Therefore the relationship between θ_1 and θ_3 can be obtained as

$$\tan\theta_1 + \cos\alpha_{23}\tan\theta_3 = 0. \quad (3.67)$$

It matches Eq. 2.21 from its 6R counterpart.

The equality of the above equations suggests that the spherical linkages consisting of four, five and six revolute joints and their thickened version are kinematically equivalent throughout the folding process. It is thus conjugated that adopting the offset crease technique for an arbitrary single vertex origami with zero-thickness does not alter its original kinematics, regardless of the number of creases.

3.2 Design approach for adopting the offset crease technique to physical models

Most engineering applications are developed from a rigid origami tessellation consisting of multiple vertices. It requires a series of single vertices origami patterns to be combined by merging common creases shared by neighbouring units. Generally, the units are repeated through translations or rotations to achieve an extended surface. The aim of this

section is to develop a design method for adding material thickness to origami tessellations via the offset crease technique. To intuitively aid this illustration, the traditionally well-known tessellation, the Miura-ori, as introduced in Section 2.3.2, is selected as an example. This highly over-constrained mechanism can be folded rigidly and flatly with an overall mobility of one. The assembly is made of a group of 4R spherical linkages, which can be transformed to a group of 8R spatial linkages. Therefore it is deemed as a proper parent pattern to adopt the offset crease technique.

3.2.1 Crease widths assignments

This approach starts by defining offset distance for each crease. In other words, each widened crease needs to be assigned with a width to accommodate panel thickness, which is twice of an offset distance for each crease.

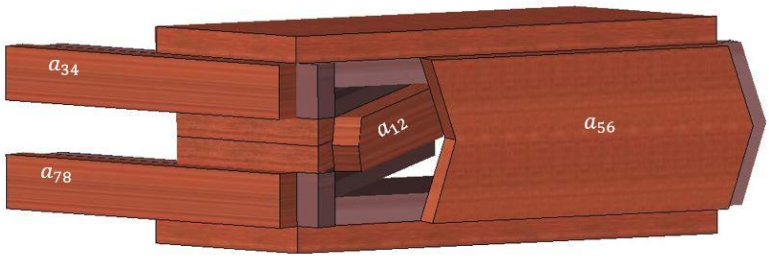

Figure 3.5 Topological diagram of a single vertex 8R spatial linkage with thick panels at the folly folded state.

The common goal of most deployable structures is to achieve a most compact form in a fully stowed state, which requires the widths of creases to be minimum to reduce voids. Furthermore, the offset crease technique demands two thick layers, with same thickness λ, to ensure integral stiffness and flatness. This configuration implies a minimum possible width of 2λ. According to Eq. 3.2, the width of the widest crease a_{56} equals to 6λ, i.e. the sum of widths of the rest three narrower creases. This is due to the geometry at the fully folded state as shown by the detailed topology in Figure 3.5. The widest crease a_{56} needs

to span a total gap created by a combination of a_{12}, a_{34} and a_{78}. If a_{56} is chosen too large, a desired compact form is not achievable. In contrast, if the width of this enveloping crease is too small, it will restrict the full range motion, and thus the model cannot be folded flat.

The crease widths of the Miura-ori are determined in the same way with a sortable crease ordering. Notably, for a widened crease that does not envelop any other creases at a fully stowed state, such as a_{12}, it can be assigned with the minimum width 2λ. It applies to all widths of creases along zigzag lines, noted as C^Z. For widths of ceases along horizontal paths, noted as C^H, the narrowest creases are the ones on the top right corner and the bottom left corner. The ordering starts from these two creases as No.1 and the rest creases along this line are then numbered in a sequence (2, 3, 4,…, μ) (Figure 3.6). Summing up the total widths of three narrower creases around a single vertex leads to a value of C_2^H of 6λ. Similarly, the widths of C_3^H, C_4^H and C_5^H are 10λ, 14λ and 18λ, respectively. It is therefore concluded for the Miura-ori, there is

$$C_\mu^H = (4\mu - 2)\lambda. \tag{3.68}$$

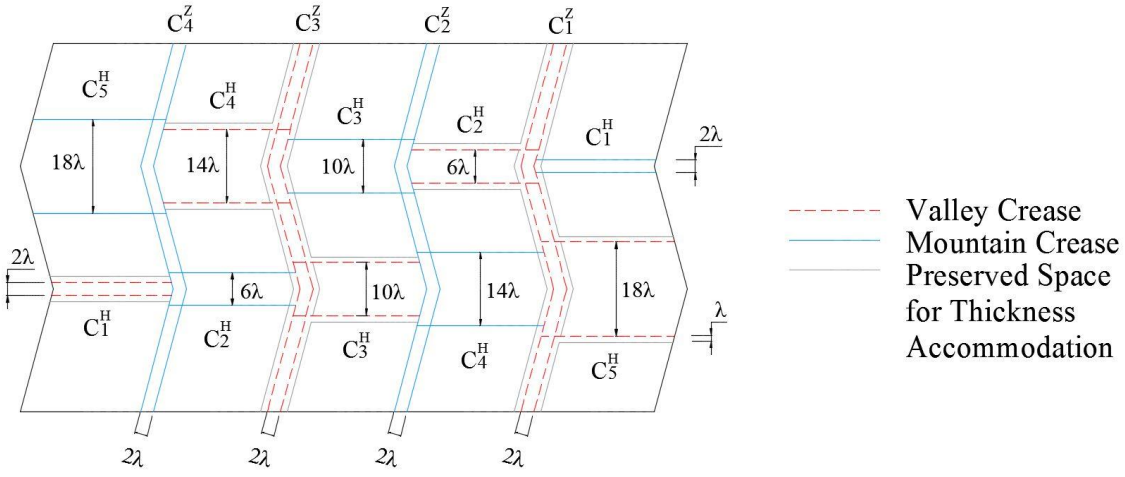

Figure 3.6 Schematic diagram of an offset crease pattern of the Miura-ori.

It is noteworthy that Eq. 3.68 cannot be generalised to all crease patterns, the width determination for each particular tessellation requires vertex-by-vertex analyses.

Nonetheless, the previousely metioned accumulation and crease ordering rules can be applied to all configurations for the width assignment, providing a comprehensive guidence for adopting the offset crease method.

3.2.2 Clipping area determination

Once widths of all creases have been assigned, the offset creases pose another problem since they are no longer able to meet in a concurrent point. The subsequent modification will entail surrounding materials around an apex to be discarded, in order to avoid local self-intersections. In the design process, a series of polygons are formed to represent the trimmed areas, with each polygon enveloping one vertex. A close look of facets around a sample vertex is given in Figure 3.7.

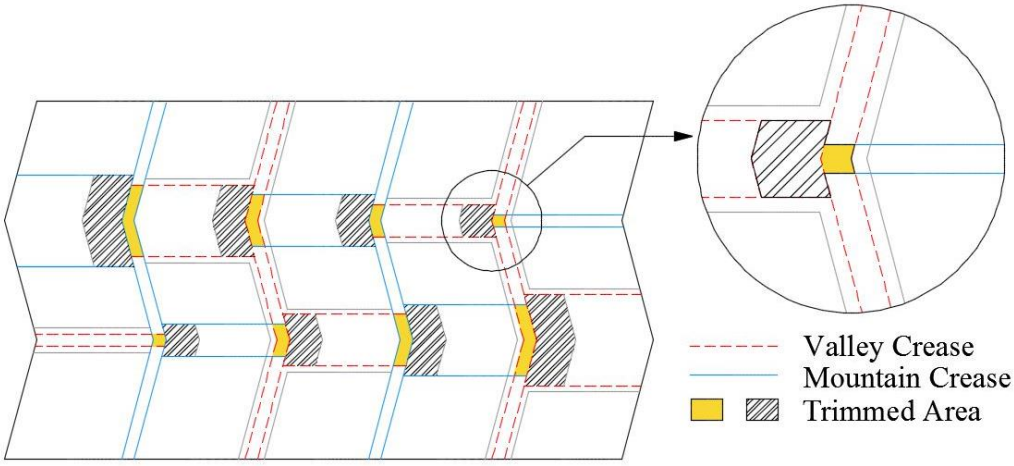

Figure 3.7 Schematic diagram of trimmed areas.

A clipping zone generally involves two types of polygons. The polygon hatched by yellow contains the original vertex, which needs to be trimmed first to enable movement. This area is relatively easy to be defined through simply enclosing the facet bounded by offset creases. For the rest part (as denoted by the shaded area), however, its shape depends on a combinations of three key factors: panel thickness λ, crease widths C and sector angles α. In addition, different configurations and panel thickness will produce completely diverse

situations. This indicates an intrinsically high complexity to quantitatively define geometry and area of discarded polygons. Moreover, the accurate analysis of the polygons is considered to be trivial in physical models. Consequently, this report does not attempt to develop a rigorous algorithm for determining trimmed zones. Instead, these zones will be qualitatively estimated to suffice the need for developing physical implementation, leaving the quantitative analysis as an open question.

For the offset crease pattern of the Miura-ori (Figure 3.7), the shaded area is assigned to be on the wider creases only, leaving the narrower creases and adjacent panels unaffected. Therefore, the ability to fold completely flat only depends on how much a wider crease will be clipped. Ideally, an optimal design requires the trimmed polygons to be as small as possible, as a reduced facet with relatively large hollow sections is not desired for majority of engineering applications. However, if the polygons are chosen too small, self-intersections are expected when the assembly is stowed. Figure 3.8 illustrates an offset crease Miura-ori model. The insufficiently trimmed materials cause collisions between panels and inhibit further movements towards the complete folded configuration. This problem can be solved by simply shorten wider creases from the near-vertex side.

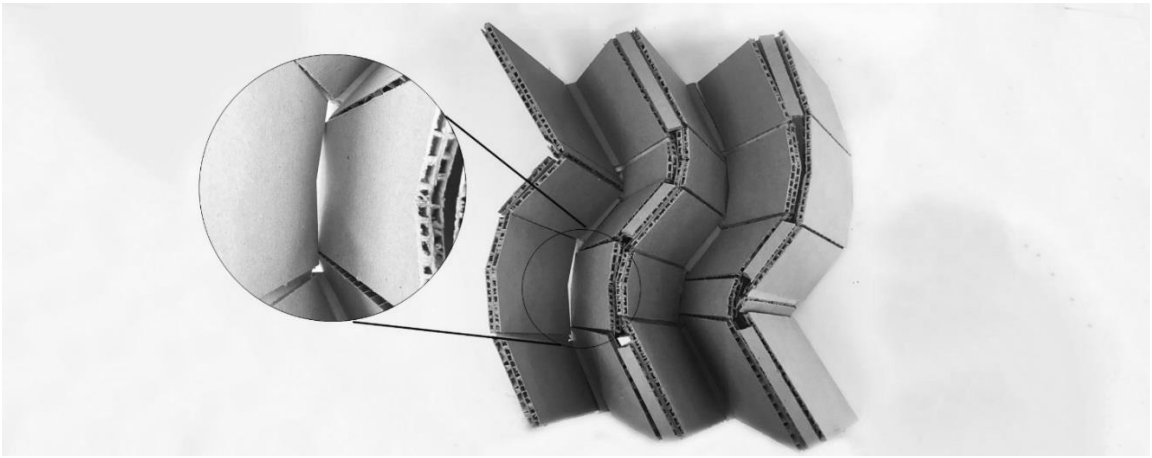

Figure 3.8 Local-intersections impede the full range motion.

3.2.3 Adding thickness

So far, based on the offset crease technique, an altered crease pattern with significant thickness has been developed from its origami source pattern. The altered pattern can be printed on a thin layer. In order to aid manufacturing, this layer can be used, not necessarily though, as an intermediate membrane where thick panels can be simply attached to both sides of it.

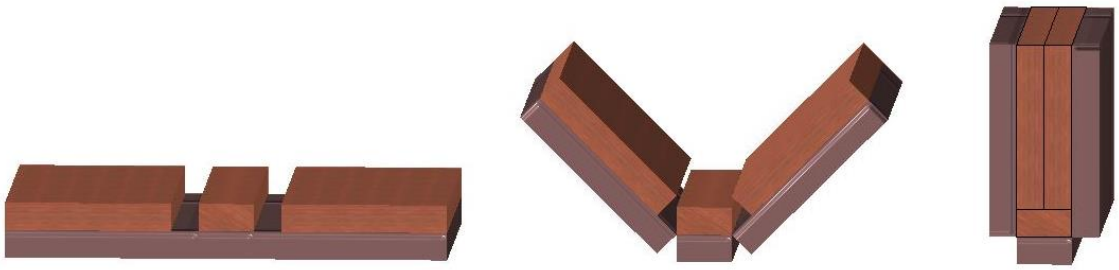

Figure 3.9 Schematic diagram of a valley crease with discarded strips.

It is noteworthy that two strips in the vicinity of valley creases with width λ needs to be trimmed to accommodate thickness of creases (Figure 3.9). The discarded materials in these zones eliminate local intersections and should be pre-assigned before attaching thick panels on the modified thin layer, as marked by grey lines in Figure 3.7.

Generally, most engineering applications, e.g., furniture surfaces, solar panels, expect surfaces of panels to be flat wherever possible. Therefore a constant two-layer layout is adopted through the entire configuration, with exception of discarded areas. Such uniformity ensures higher stiffness since the region with a single thick layer or a membrane only will be extremely vulnerable. In fact, this two-layer layout can be deemed as a single layer with a thickness of 2λ, where the rotational hinges lie right in the middle of the layer.

However, it does not mean that a non-uniform thickness are inapplicable for sufficing particular needs. As the crease widths are positively proportional to the maximum panel thickness λ, other panels can be assigned with arbitrary thickness within the attainable

range $[0, \lambda]$. On this occasion, the thickness can still be accommodated by the widened creases, although gaps between layers may be generated accordingly.

3.2.4 Solutions for non-flat-foldable models

Figure 3.10 Adopting the offset crease method to alternative dihedral angles: (A) 120˚ and (B) 60˚

For non-flat-foldable assemblies, there must exist some creases whose dihedral angles do not reduce to zero in the fully stowed state. This indicates that motion of these creases needs to be inhibited at a particular point, instead of allowing the complete range $[0, \pi]$ to be achieved. To meet this requirement, the offset creases are slightly modified to ensure the correct folding range. Figure 3.10 shows two examples with alternative dihedral angles, which can be achieved by simply changing the shape of the inside layers. Therefore a non-flat-foldable origami with significant thickness can be constructed by utilising the modification according to different folding ranges. A specific illustration is given by Figure 3.11, where a five crease vertex origami with diverse dihedral angels is thickened via the offset crease technique.

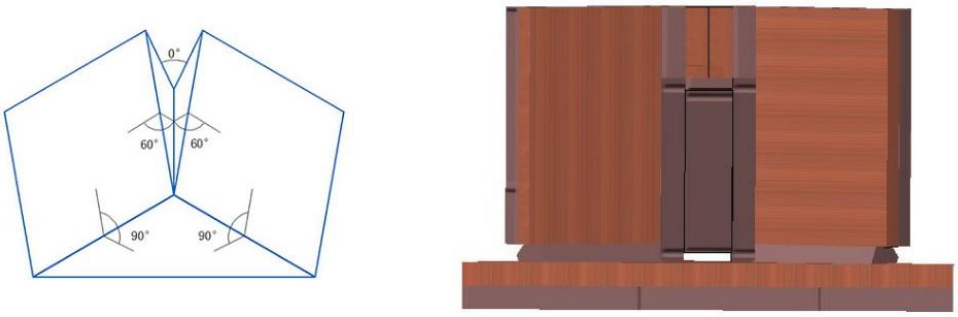

Figure 3.11 An example of a non-flat-foldable thick origami pattern.

3.3 Models

The above approach leads to a design guidance on how the offset crease technique can be applied to accommodate thickness. Following this guidance, attempts has been made to test its applicability on a number of existing origami tessellations. This section illustrates a number of tessellations which are suitable parent patterns for the technique. The corresponding physical models with rigid thick panels are presented in multiple states. On the other hand, some specific crease patterns are tested to be inadaptable for the technique. Detailed reasons are analysed with the aid of computer modelling.

3.3.1 Eligible applications

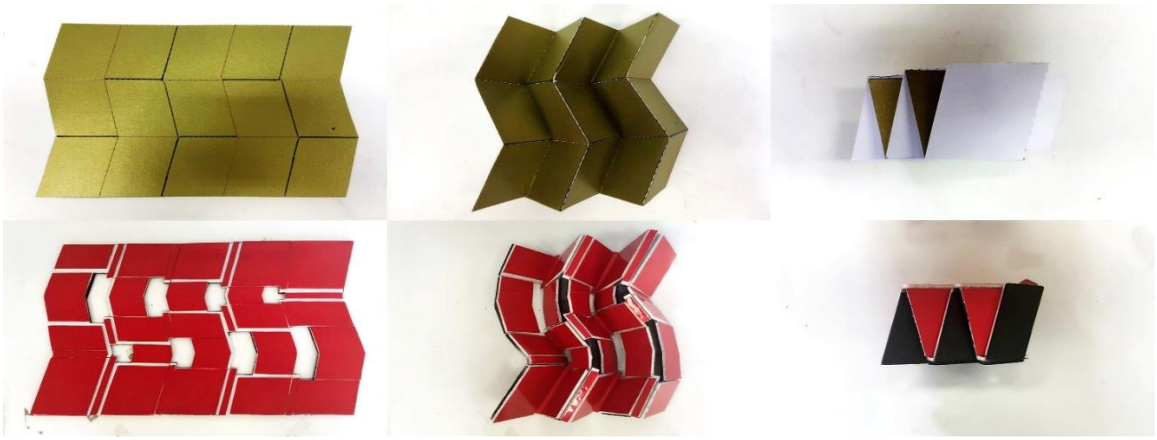

Figure 3.12 Folding sequence of a Miura-ori pattern with thick panels based on the offset crease technique and its zero-thickness source pattern.

Firstly, a physical implementation of a Miura-ori pattern has been constructed with 5mm foam boards. The folding process of the thick model are given in Figure 3.12, with respect to its zero-thickness parent origami pattern. This model has a neatly even surface once fully collapsed, presenting great applicable potential. However, it can be seen that crease widths are incremental along the horizontal sides and remain constant along zigzag sides as described in Section 3.2.1. This property confines the extension along horizontal direction as some creases will be excessively wide.

Figure 3.13 Folding sequence of a square-twist pattern with thick panels based on the offset crease technique and its zero-thickness source pattern.

Another commonly used rigid tessellation is the square-twist pattern. Four flat-foldable four-crease vertices are combined in a rotationally symmetric configuration, and it has a single mobility. The paper pattern with negligible thickness and its thick counterpart are given in Figure 3.13. The maximum width is, again, 6λ, which confirms the proposed accumulation rules for the width assignment.

However, the most ideal configuration requires all creases to have the minimum possible width 2λ constantly for the entire tessellation. In this occasion, the fully folded compact form will not be excessively thick and thus a smaller volume is achievable. Furthermore, the offset crease approach requires rotations of two parallel creases in each pair to be kept

identical throughout the folding process. Also, one mobility from each pair must be frozen to ensure no extra mobility to be introduced by offset creases. Both conditions can be satisfied through placing a pair of gears to match the motion of parallel twin creases (Figure 3.14-A) However, these gears are only suitable for constant minimum widths since wider creases demand larger gears, where the protruded part will collide with panels in stowed state, as illustrated on Figure 3.14-B.

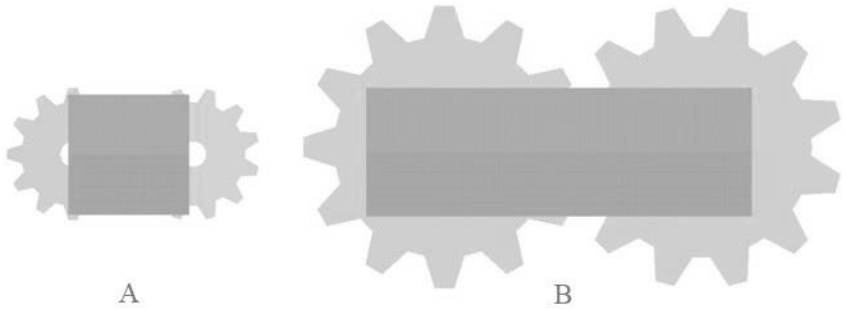

Figure 3.14 Sizes of gears depend on widths of creases.

These reasons make the tessellation with wider creases inferior to those with constant minimum widths when adopting the offset crease technique. Therefore a tessellation known as the diamond pattern, which composes of six crease vertices has been developed. The assembly adopted an identical angular configuration set by Eqs. 3.60 and 3.61, where plane-symmetry constrains the assembly with mobility one. As illustrated in Figure 3.15, this tessellation has been transformed to a series of 12R spatial linkages with thickness being added. This model ensures the width to be 2λ for each crease, which is the most desirable crease pattern for the technique.

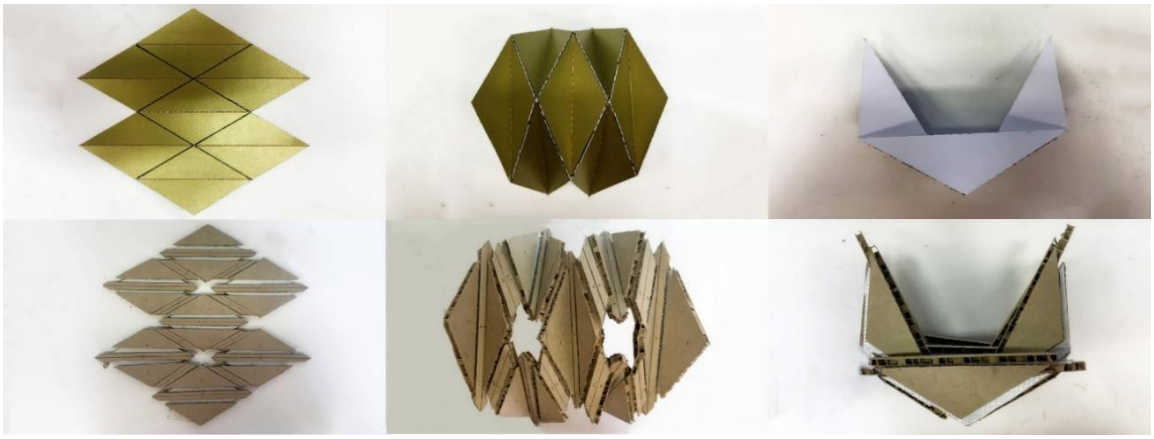

Figure 3.15 Folding sequence of a diamond pattern with thick panels based on the offset crease technique and its zero-thickness source pattern.

3.3.2 Ineligible applications

Despite being able to be applied to all single-vertex origami, the offset crease technique is proven to be unsuitable for some specific tessellations containing multiple vertices.

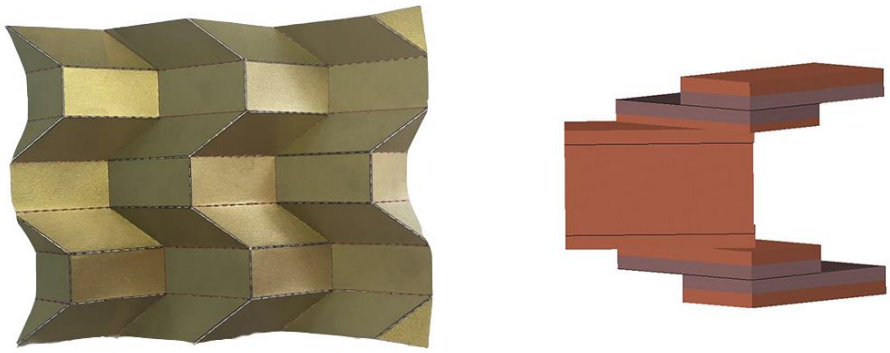

Figure 3.16 The accumulation of heights nullifies the original crease pattern.

A typical example is given by Figure 3.16. This configuration consists of a group of non-flat-foldable four crease vertices, which can be seen as another modified version of the Miura-ori. When applying the offset crease technique, the next unit needs to be moved away from its original position in order to accommodate the thickness of the previous panel. This movement forces the height of the assembly to be accumulated and thus nullifies the original crease pattern.

Another example is the winding membrane pattern, as reviewed in Section 2.5.2. The pattern is designed for an ideal zero-thickness condition where the layers are coplanar with the verge of the hub when fully stowed. In reality, however, the outer layers of panels are stacked atop of the inner layers, which suggests that adopting the offset crease technique will cause self-interferences between layers. A topographic diagram showing the collisions is given in figure 3.17.

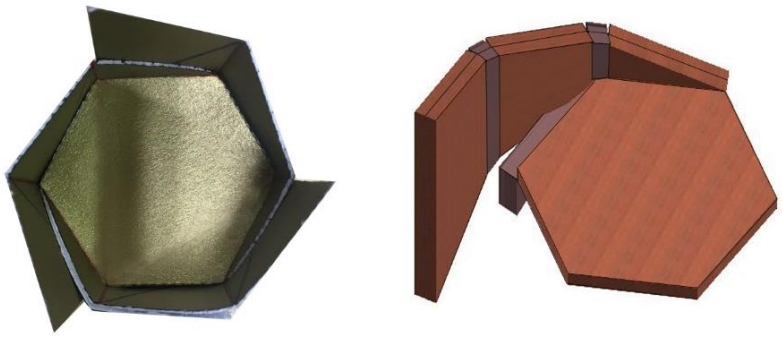

Figure 3.17 The collisions between layers impede the motion.

Consequently, these two patterns are proven to be ineligible for applying the offset crease technique.

3.4 The anisotropic Miura-ori tessellation

Over the last few decades, the traditional Miura-ori has been utilised in a wide range of applications, due to its single mobility, rigid foldability and elegant trajectories of motion. Despite being the most commonly used crease pattern, the Miura-ori possesses obvious limitations for application with thick panels. Its isotropic geometry results in a over-stacked configuration once folded, i.e., the next zigzag unit envelopes the previous one. Therefore, difficulty is encountered when the Miura-ori is adopted with thickness-accommodating techniques. For instance, the offset crease technique may require excessively wide creases to avoid self-intersections, which produces a relatively large

volume at the fully stowed state. In response to these limitations, in this section we propose a derivative tessellation based on the traditional Miura-ori.

3.4.1 Crease pattern design

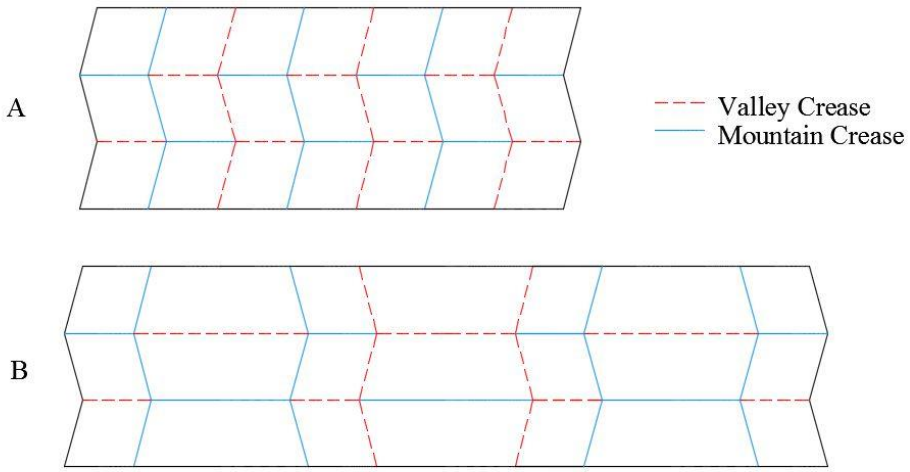

Figure 3.18 The crease pattern of (A) the traditional Miura-ori and (B) the anisotropic Miura-ori.

To overcome the above mentioned limitations, the stacked configuration must be avoided. This is done by reversing a portion of zigzag creases to form an anisotropic layout, as shown by Figure 3.18. The pattern is thus divided into a series of identical folding units with symmetry being imposed for each single unit. Instead of producing an over-stacked layout, this modification allows the folded panels to be separated unit by unit once fully stowed. The schematic diagram of the traditional Miura-ori and the anisotropic Miura-ori is illustrated in Figure 3.19 for comparison.

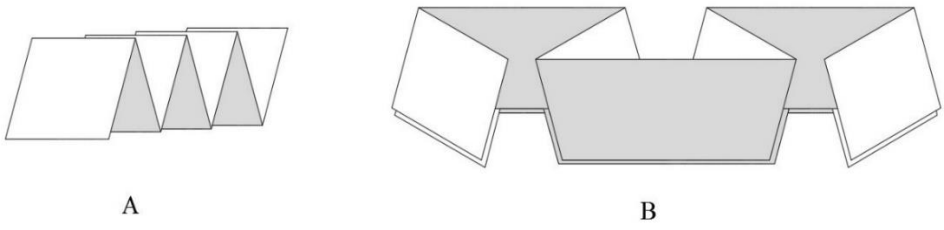

Figure 3.19 The fully stowed configuration of (A) the traditional Miura-ori and (B) the anisotropic Miura-ori.

Although the original kinematics has been altered, the anisotropic Miura-ori still keeps the advantages possessed by the traditional one. Firstly, the assembly can be actuated with a single degree of freedom, which guarantees the simplicity in control. Consisting of a number of 4R linkages, the tessellation can be folded flatly without requiring any facets to be deflected. Finally, it presents negative Poisson's ratio. In other words, the projected extent can be shrunk in both orthogonal directions. This presents great application potential.

3.4.2 Prototype optimization

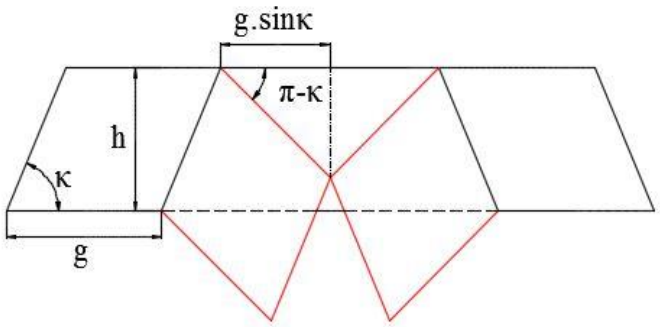

Figure 3.20 Schematic diagram of a unit cell from the anisotropic Miura-ori tessellation.

Generally, an optimized design requires a relatively large deployed-to-stowed ratio. In this tessellation, the ratio is dependent on three major parameters within a folding unit, the height h, the width g and the inner sector angle κ of the parallelogram, as illustrated in Figure 3.20. It should be noted that to achieve the most compact form, the two folded parallelograms, as denoted by the red lines, are supposed to be sufficiently close. Therefore the dimensions of the trapezium can be related to the three above mentioned parameters of side parallelograms.

This geometric connection allows us to qualitatively analyse the global deployed-to-stowed ratio. Given a consistent number of unit cells, comparisons can be carried out by simply altering a single variable from the parameters and the results are show in Figure 3.21. As can be visually observed; larger values of h and g yield a massive increase in

surface area, with slight growth on the stowed volume. This allows the two parameters to be assigned according to the diverse requirements of applications. Moreover, as κ approaches to $\frac{\pi}{2}$, the zigzag creases tend to become near straight lines. This variation produces a more desired ratio, although the less skewed configuration could generate an extra degree of freedom.

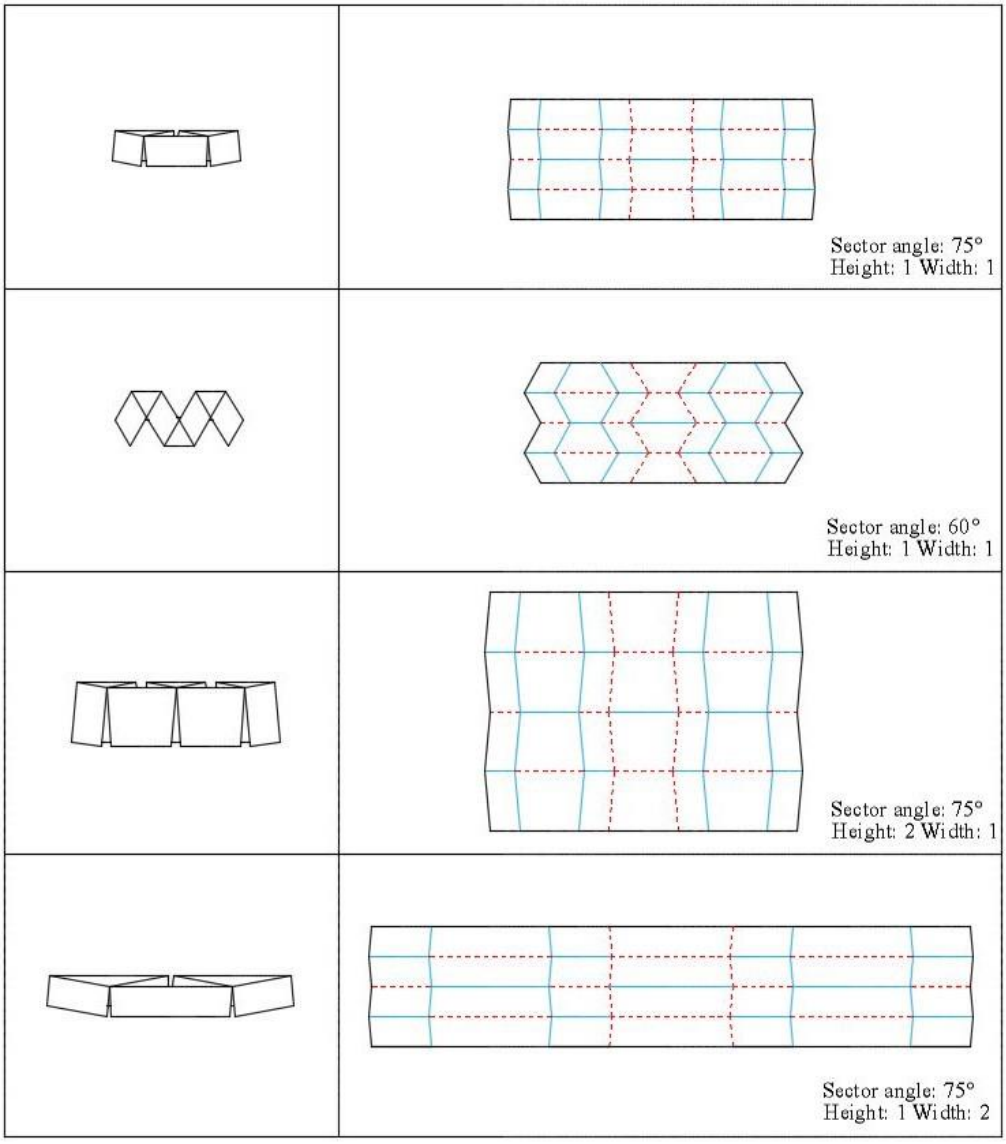

Figure 3.21 The modified anisotropic Miura-ori tessellations in completely folded and deployed state.

3.4.3 Applying thickness accommodation techniques

Although the anisotropic Miura-ori tessellation applies to a number of possible applications, a motivating driver for this derivation was the development for adopting thickness-accommodation techniques. In particular, the excessively wide creases from the traditional Miura-ori, resulting from the offset crease method, are expected to be avoided.

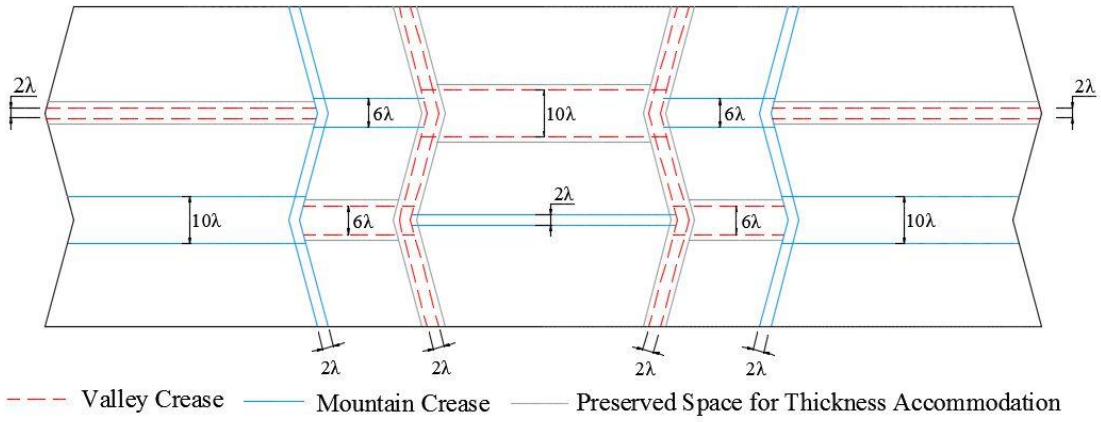

Figure 3.22 Crease pattern of an anisotropic Miura-ori tessellation with the offset crease technique.

Under the design approach proposed in Section 3.2, a modified crease pattern based on the traditional Miura-ori has been proposed, as shown in Figure 3.22. Instead of being accumulated in the traditional Miura-ori, the layers are separated into a number of identical unit cells. In this case, the crease widths are only up to ten times of panel thickness λ. This modified configuration allows the tessellation to be extended infinitely by simply repeating a unit cell, which greatly reduces the stowed volume. A physical implementation of the tessellation with the offset crease technique is shown in Figure 3.23.

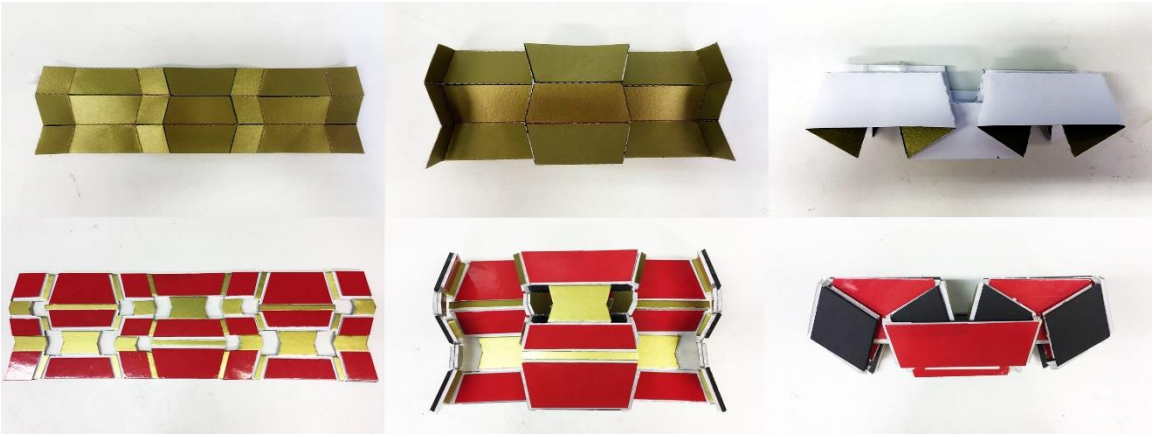

Figure 3.23 Folding sequence of an anisotropic Miura-ori pattern with thick panels based on the offset crease technique and its zero-thickness source pattern.

Besides the offset crease technique, this tessellation also presents applicability for other thickness accommodating methods which maintain the original kinematics. For convenience, the improved hinge shift method proposed by Chen, Peng and You (2015) was selected as a demonstrative example for the adoption of this tessellation.

For the anisotropic Miura-ori tessellation which consists of a series of 4R linkages, the hinge shift method requires axes of revolute joints to be separated from the original concurrent layout, as reviewed in Chapter 2.4. Therefore the spherical linkages are transformed to spatial linkages with four revolute joints. To ensure rigid foldability, this assembly must be a Bennett linkage, as it is the only known spatial 4R linkage. The Bennett linkage requires special geometrical restrictions, which are

$$a_{12} = a_{34}, a_{23} = a_{41} \text{ and } \frac{a_{12}}{a_{23}} = \frac{\sin\alpha_{12}}{\sin\alpha_{23}}. \tag{3.69}$$

Therefore extra layers of trapeziums are utilized to satisfy Eq. 3.69 for each single linkage, as illustrated in Figure 3.24.

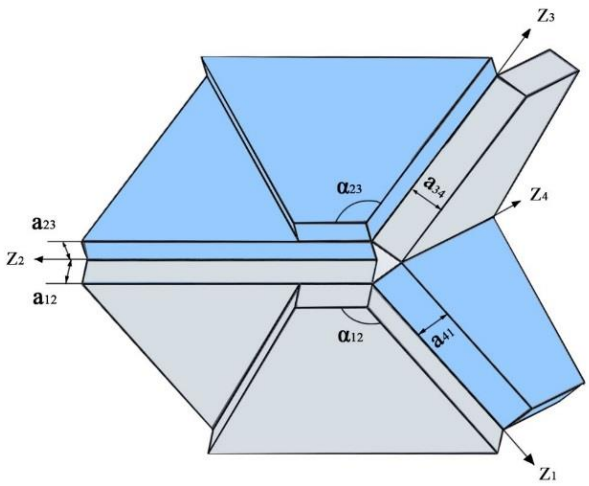

Figure 3.24 Topography of a 4R spatial linkage from the anisotropic Miura-ori tessellation.

Repetitively implanting this arrangement allows the thickness to be added to the entire tessellation. The folding sequence of the thickened assembly via the hinge shift method is shown in Figure 3.25. Therefore, applications with a large surface area such as solar panel arrays or retractable roofs might be achievable without radically altering the kinematics of the traditional Miura-ori.

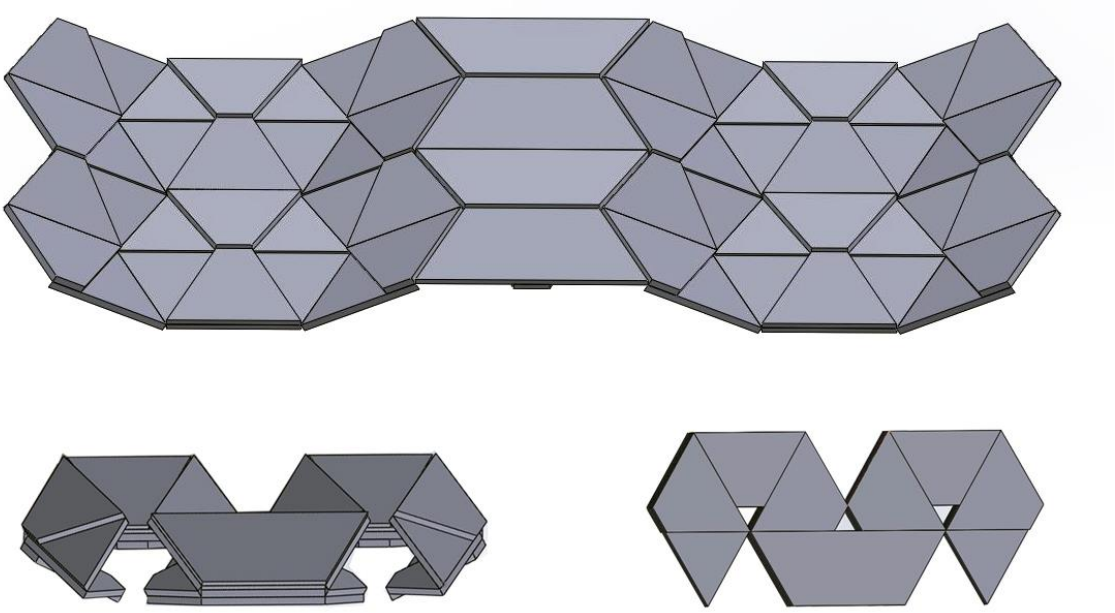

Figure 3.25 Folding sequence of an anisotropic Miura-ori pattern with thick panels based on the modified hinge shift technique.

3.5 Conclusions and discussions

This chapter has presented a comprehensive analysis on developing rigid origami with thick panels. It mainly focuses on the offset crease technique, which presents great potential for application, but with unclear kinematics and adoption methodology.

Firstly, I have identified the motion trajectories of thickened versions from three commonly used single-vertex origami patterns. The patterns have been modified through the offset crease method; with their angular configuration remaining unchanged. This allows us to conduct comparisons between 8R, 10R and 12R spatial linkages and their source patterns, i.e. the corresponding 4R, 5R and 6R spherical linkages. The results prove analytically that, given the rotations from a pair of parallel folds are identical; the motions of the former assemblies strictly imitate those of the latter ones. This means single-vertex offset crease patterns and their parent origami patterns are kinematically equivalent. In other words, the offset crease technique enables material thickness to be accommodated without altering the original motions.

A detailed design approach for adapting the offset crease technique has been proposed. The development of the thickness accommodating patterns was based on their source origami pattern with zero thickness, as their motions are exactly alike. The design process started with crease width assignment. In order to accommodate material thickness, creases are offset from their original positions. An offset distance depends on the inherent geometry of the tessellations, which is equivalent to a half of a crease width. The materials in the vicinity of each crease need to be discarded to avoid self-intersection. In this report I have only empirically defined the approximate scope of the clipping area, leaving the quantitative analysis as an open question. The thick panels should then be attached on both sides of a thin membrane with a modified crease pattern to complete the fabrication process.

A number of physical models with significant thickness have been presented following the proposed design guidance. Successful implementation proves that the guidance is able to be generalised to all eligible tessellations. Moreover, the ineligible patterns for using the offset crease method have been illustrated and the reasoning explained accordingly.

Finally, a novel crease pattern derived from the traditional Miura-ori has been proposed. The pattern adopts an anisotropic arrangement by reversing a portion of zigzag creases. Despite being modified, the pattern retains the key properties from the traditional Miura-ori with a single mobility. Attempts have been made to optimize the design with a high deployed-to-stowed ratio, which can be achieved by increasing the values of the three parameters of the side parallelograms. We have also shown that this anisotropic Miura-ori tessellation is an adequate pattern to be thickened with two existing thickness-accommodating methods, the offset crease and the hinge shift technique.

4. Inextensional Deployable Patterns

In response to the demand within aerospace engineering to develop rigid deployable solar receivers, considerable attempts have been made to discover adequate models. The solar panel arrays require the prototype to be capable of accommodating material thickness, whereas the design of solar sails allows the thickness to be neglected as the film is just 1/100 of standard paper thickness.

In this chapter, the different patterns which enable the facets to be wrapped around a central hub are investigated first. The hexagonal prototype invented by Guest and Pellegrino (1992), i.e. the winding membrane, is examined to determine whether an inextensional transition is possible. Two modified origami prototypes based on the winding membrane are proposed and transformed into pin-jointed frames for numerical validation of their rigid-foldability. The mechanical modelling method is used to simulate the folding process, and the trajectories of motion are obtained. The eligible wrapping prototypes are then developed further, which leads to a method that enables material thickness to be accommodated. Subsequently, the two layer hexagon-hub patterns are extended to prototypes with multiple layers or square-hubs. In this process, the complex algorithms are simplified and generalised for simulating all types of rigid origami patterns. With custom coding, user-friendly software has been developed as a rigid origami simulator. In addition to the wrapping patterns, a sequential square-twist origami is presented and examined for the application of solar sails. Finally, the strengths and weaknesses of this work are discussed, which concludes this chapter.

4.1 Verifying the existence of a rigid transition for the winding membrane

According to the negative mobility from the Kutzbach criterion, the winding membrane (Ω_1) shown in Figure 2.13 is a static structure where the model is only inextensional in the

fully flat and the fully deployed forms. However, the mobility count alone cannot deny the capability of motion because the assembly might be an over-constrained mechanism if special geometrical conditions are met. This requires a strict numerical verification to prove whether the radical symmetric configuration enables rigid foldability without flexing any facets.

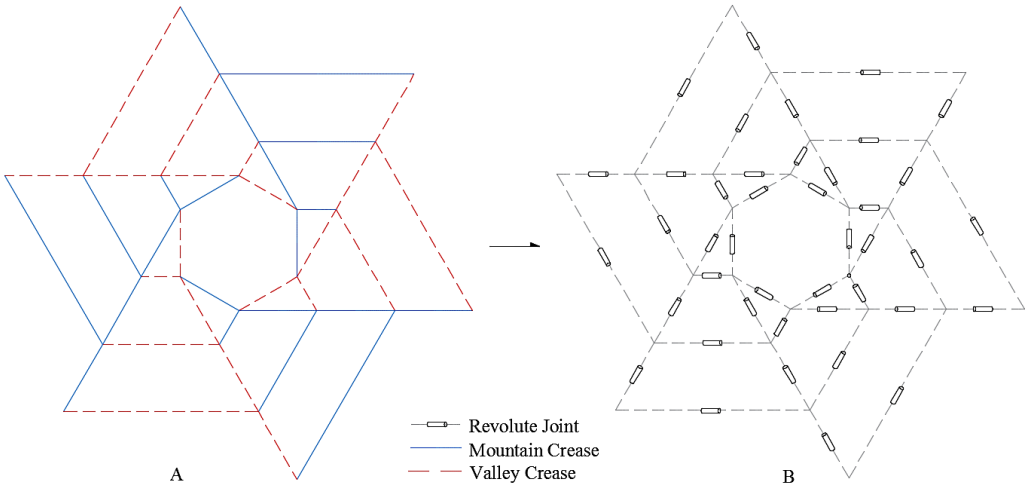

Figure 4.1 (A) The winding membrane pattern (Ω1) is transformed to (B) a frame with a series of spherical linkages.

To examine the existence of a rigid transition, this four-crease vertex origami pattern shown in Figure 4.1-A is firstly converted to a frame containing a series of spherical 4R linkages in which the panels and creases are represented by links and revolute joints, respectively (Figure 4.1-B). Therefore this complex system is decomposed to a series of subsystems, with each subsystem containing a single vertex.

Again, the matrix method is selected to transform coordinates from one link to another around a vertex with the DH notation, and thus all geometric relationships between links can be accounted for. By hypothesizing that a rigid transition exists, we can treat the winding membrane (Ω_1) as a mechanism. Therefore loop-closure conditions can be established for each spherical linkage, which brings the concatenation of 3D

transformation matrices to an identity matrix. For a single vertex with four links in Ω_1 there is

$$Q_{12}Q_{23}Q_{34}Q_{41} = I_3, \tag{4.1}$$

which can be rearranged as

$$Q_{12}Q_{23} = Q_{14}Q_{43}. \tag{4.2}$$

Substituting Eqs. 2.4a and 2.4b into Eq. 4.2 yields a series of non-linear equations composed of rotational angle θ_i and sector angle $\alpha_{i(i+1)}$. For convenience, three loop-closure equations are selected from the results of Eq. 4.2 for calculation, which are

$$\cos\alpha_{12}\cos\alpha_{23} - \cos\theta_2\sin\alpha_{12}\sin\alpha_{23} = \cos\alpha_{34}\cos\alpha_{41} - \cos\theta_4\sin\alpha_{34}\sin\alpha_{41}, \tag{4.3a}$$

$$\begin{aligned} -\cos\alpha_{23}\cos\theta_1\sin\alpha_{12} - \cos\alpha_{12}\cos\theta_1\cos\theta_2\sin\alpha_{23} + \sin\alpha_{23}\sin\theta_1\sin\theta_2 \\ = \cos\alpha_{41}\cos\theta_4\sin\alpha_{41} + \cos\alpha_{34}\sin\alpha_{41}, \end{aligned} \tag{4.3b}$$

$$\begin{aligned} \sin\alpha_{12}\sin\theta_2 = \cos\alpha_{41}\sin\alpha_{34}\sin\theta_3 \\ +\cos\alpha_{34}\cos\theta_4\sin\alpha_{41}\sin\theta_3 + \cos\theta_3\sin\alpha_{41}\sin\theta_4. \end{aligned} \tag{4.3c}$$

The sector angles $\alpha_{i(i+1)}$ of the winding membrane are known conditions. According to Eq. 2.24, the sector angles of a 6 sided wrapping pattern are calculated as

$$\eta = 120°, \beta = 30°, \omega = 120° \text{ and } \delta = 90°. \tag{4.4}$$

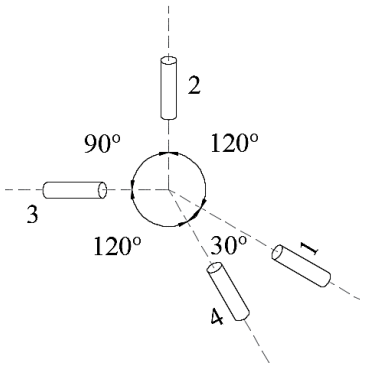

Figure 4.2 Sector angles around a vertex from Ω_1.

Consider a spherical linkage from the winding membrane, as shown by Figure 4.2, the sector angles are assigned to

$$\alpha_{12} = 120°, \alpha_{23} = 90°, \alpha_{34} = 120° \text{ and } \alpha_{41} = 30°. \tag{4.5}$$

So far, rotational angle θ_i is the only unknown parameter in Eq. 4.3. If a value of an arbitrary θ_i has been assigned as an input angle, the remaining three unknown rotational angles can be solved as output angles and the answers should satisfy all the equations.

Subsequently, the outputs can be used as inputs for the adjacent subsystem, enabling the other unknown rotational angles to be determined. Thus a forward transformation path can be created by linking adjacent subsystems. This path is then encircled to obtain a closed loop in which the final output returns to the position of the previous input. This allows the calculated angle of a revolute joint to be compared with the known value of itself. If and only if identical values are obtained within attainable ranges, the global compatibility of the assembly can be verified. In other words, a rigid transition is expected throughout the folding process. Otherwise the panels must be flexed to complete stowage and deployment.

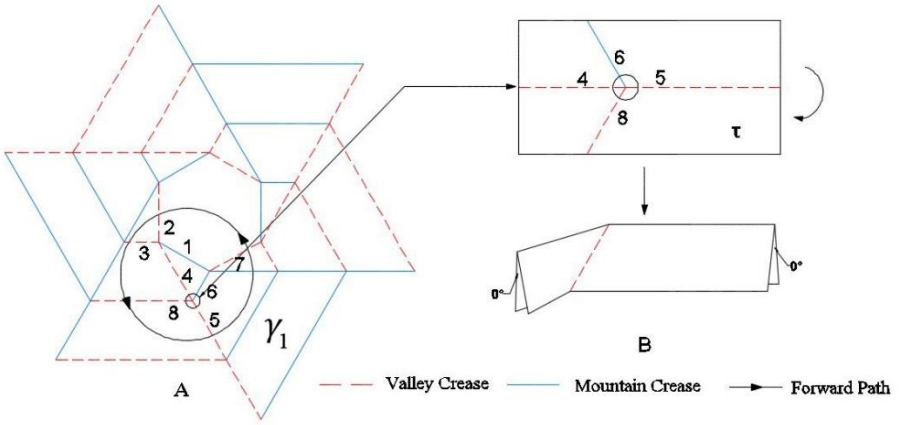

Figure 4.3 Schematic diagram of (A) the forward path γ_1 and (B) the pattern τ.

Consider the winding membrane in Figure 4.3, this configuration is formed by imposing rotational symmetry with units being repeated. This allows the global compatibility to be tested in a localised unit. Starting from the linkage with the revolute joints R_1 to R_4, a

forward path γ_1 is assigned. This path passes through all types of linkages and returns to R_1 to complete a closed loop.

According to measurements from the physical models, the attainable ranges of the four types of revolute joints are

$$-90° \leq \theta_1 \leq 0°, \tag{4.6a}$$

$$0° \leq \theta_2 \leq 90°, \tag{4.6b}$$

$$0° \leq \theta_3 \leq 60°, \tag{4.6c}$$

$$0° \leq \theta_4 \leq 180°. \tag{4.6d}$$

For convenience, stipulate θ_2 as an input angle, whose values are chosen evenly to span the range of motion. Substituting the sector angles and rotational angel θ_2 into Eq. 4.3 imparts the results of all outputs within the subsystem. By converting the output as the known conditions for the next subsystem, the turn angles along path γ_1 can be determined with the same algorithm. The complete results are listed in Table 4.1 below.

Table 4.1 Rotational angles along path γ_1 during the folding

$\boldsymbol{\theta_2}$	**0˚**	**10˚**	**50˚**	**70˚**	**90˚**
θ_1	0˚	-4.51˚	-25.23˚	-40.97˚	-90˚
θ_3	0˚	3.19˚	17.77˚	28.65˚	60˚
θ_4	0˚	14.16˚	73.41˚	108.42˚	180˚
θ_5	0˚	14.16˚	73.41˚	108.42˚	180˚
θ_6	0˚	-	-	-	-60˚
θ_1	0˚	-	-	-	-90˚
θ_2	*0˚*	-	-	-	*90˚*

In Table 4.1, figures in bold represent the input angles, and figures in red are the final outputs from the same component. According to Table 4.1, inputting the boundary condition of θ_2 yields the range of motion from all types revolute joints. By comparison, the values obtained are consistent with the data measured from the physical model. This confirms the method is correct. Achieving local compatibility requires the equality of θ_2. However, it only exists when the input angle is either 0˚ or 90˚, representing the fully flat and stowed states, respectively. The sequential steps cease at θ_6 when the assembly is in transition between the two final states. This is due to the special geometry of the four crease-vertex pattern τ, as given in Figure 4.3. The rotations of two inclined creases R_6 and R_8 are inhibited until the R_4 and R_5 are completely folded. In other words, the motions of the two pairs of creases are completely independent, introducing an extra mobility. Nonetheless, a rigid transition of Ω_1 requires the entire assembly to move simultaneously with only one degree of freedom. It means the locally obstructive pattern τ has to be eliminated to pursue rigid foldability. The modifications are made in two ways.

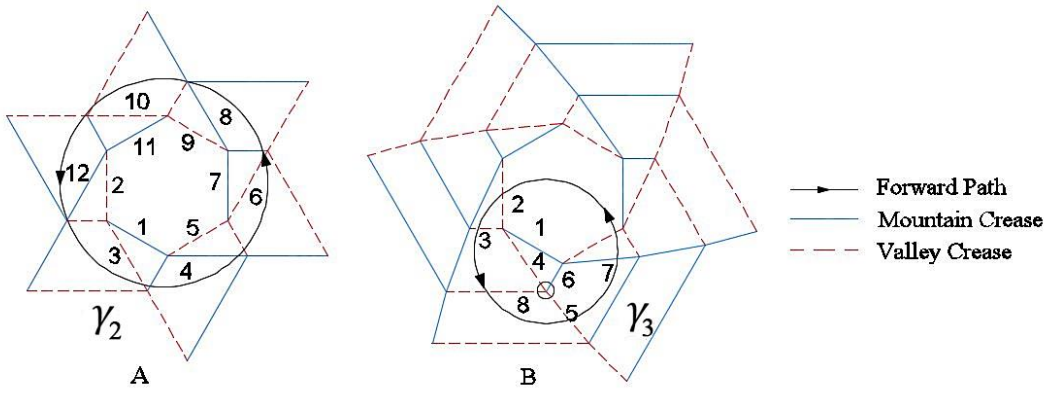

Figure 4.4 Schematic diagram of forward path γ_2 and forward path γ_3

Firstly, a different path γ_2 is adopted with the outmost panels being removed, as shown in Figure 4.4. Despite being undesired for most applications, as the surface area is significantly reduced, it breaks the pattern τ. Alternatively, it can be changed by replacing

the straight line with piecewise lines. This model was initially invented by Guest and Pellegrino (1992) for the purpose of thickness accommodation, as reviewed in Section 2.5.4. In this case, the modification is made to enable the synchronized motion from the previous pattern, τ. By introducing a skewed angle of 5˚ for R_5, the slight asymmetry provides a preferential collapsing direction. Therefore all of the creases can be rotated simultaneously, allowing the global compatibility to be verified along path γ_3.

Applying the same algorithm for the two paths yields all output angles. For path γ_2, the inputs and outputs are given in Table 4.2.

Table 4.2 Rotational angles along path γ_2 during the folding

$\boldsymbol{\theta_2}$	**0˚**	**10˚**	**50˚**	**70˚**	**90˚**
θ_1	0˚	-4.51˚	-25.23˚	-40.97˚	-90˚
θ_3	0˚	14.16˚	73.41˚	108.42˚	180˚
θ_4	0˚	-6.38˚	-35.98˚	-59.33˚	-180˚
θ_5	0˚	2.03˚	11.65˚	19.84˚	90˚
θ_6	0˚	2.87˚	16.51˚	28.20˚	180˚
θ_7	0˚	-0.91˚	-5.27˚	-9.07˚	-90˚
θ_8	0˚	-1.29˚	-7.45˚	-12.83˚	-180˚
θ_9	0˚	0.41˚	2.37˚	4.09˚	90˚
θ_{10}	0˚	0.58˚	3.35˚	5.78˚	180˚
θ_{11}	0˚	-0.18˚	-1.07˚	-1.84˚	-90˚
θ_{12}	0˚	-0.26˚	-1.51˚	-2.60˚	-180˚
θ_2	*0˚*	*0.08˚*	*0.48˚*	*0.83˚*	*90˚*

As shown in table 4.2, above, the inequality of θ_2 suggests the pattern is globally incompatible. In other words, a closed loop cannot be formed. It means that a rigid transition cannot be completed by this pattern since loop-closure is a necessary condition for folding rigidly. This result is confirmed by a rigid physical model made of 1mm thick

aluminium sheet (Figure 4.5). The winding membrane disallows even slight movements from two globally compatible states: fully flat and fully stowed.

Figure 4.5 A rigid physical model for the winding membrane pattern in (A) the fully flat state and (B) the fully stowed state.

Similarly for path γ_3, the angles are listed in Table 4.3.

Table 4.3 Rotational angles along path γ_3 during the folding

$\boldsymbol{\theta_2}$	**0˚**	**10˚**	**50˚**	**70˚**	**90˚**
θ_1	0˚	-5.94˚	-34.11˚	-59.42˚	-
θ_3	0˚	4.35˚	22.61˚	38.69˚	-
θ_4	0˚	15.84˚	83.89˚	130.24˚	-
θ_5	0˚	16.09˚	85.50˚	134.23˚	-
θ_6	0˚	-6.03˚	-55.27˚	-86.65˚	-
θ_1	0˚	-1.36˚	-14.27˚	-12.16˚	-
θ_2	*0˚*	*0.76˚*	*4.93˚*	*23.47˚*	-

Again the inconsistency in values of θ_2 denies the likelihood of a rigid transition. Albeit the introduction of a skewed angle removes the impediment posed by the pattern τ, it introduces evident drawbacks accordingly. Firstly, this modification breaks the original configuration that can guarantee rigidity in the fully stowed condition. Substituting $\theta_2 = 90°$ to Eq. 4.3a, the value of $\cos\theta_4$ is approximately -1.5, which means the equation is not solvable. Therefore the original maximum rotational angle 90˚ cannot be reached. This

suggests a less compact form, where obvious deflections on panels are expected, when the pattern is stowed. In fact, a larger skewed angle generates more undesired deformations.

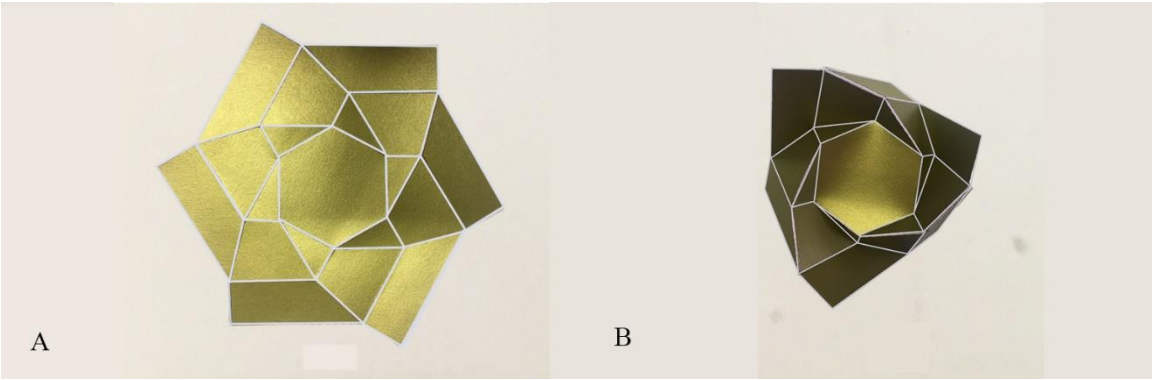

Figure 4.6 A physical model of path γ_3 in (A) the fully flat state and (B) the stowed state

This is confirmed by the physical model, as shown in Figure 4.6. The clearance between panels may be utilised to accommodate material thickness, but this only applies to flexible materials such as a membrane. Finally, the surface area of the outside panels is dramatically reduced as the radius of this near circular pattern increases, which is unsuitable for large solar arrays.

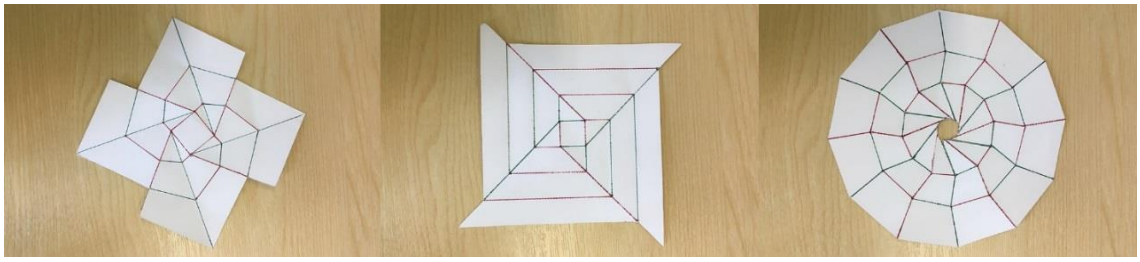

Figure 4.7 A portion of physical models with the square hub and the dodecagonal hub

It is noted that the non-rigid transition for the hexagonal pattern above also applies to patterns with a polygonal hub based on the original prototype proposed by Guest and Pellegrino (1992). This is due to the same configuring principle as reviewed earlier. Besides that, considerable attempts with diverse design strategies have been made to discover an inextensional wrapping pattern. Figure 4.7 illustrates a portion of these patterns. However, none of them are capable of strain-free wrapping. This is confirmed by physical

models and the corresponding numerical analysis with the same algorithm. By comparison, the original winding membrane has the smallest deformation during the transition and a strain-free compact form. Consequently, it is considered the most proximal pattern to wrap around a hub inextensionally and thus has been chosen as the foundational pattern for further modification.

4.2 Developing rigid foldable wrapping patterns

With the existence of a rigid transition being denied, the original winding membrane is concluded unsuitable for inextensional wrapping. Yet the pattern Ω_2 proposed by Kumar and Pellegrino (2000), as reviewed in Section 2.5.3 is the only approach known to achieve rigid-foldability. Literature review suggests evident drawbacks of this approach, including being unsuitable for particular applications where extra folds are not allowed. Therefore, a novel rigid-foldable prototype, created without any new folds, is keenly desired.

4.2.1 Prototype design

The design of a prototype will be based on the Ω_1, as it is considered as the most proximal pattern to achieve our objective to date. For this pattern, the Kutzbach criterion imparts a negative mobility, -9, and the results from the previous section suggest the geometry disallows it to be an over-constrained mechanism. Therefore the configuration is confirmed as a statically indeterminate structure. Consequently, efforts were made to convert the structure to a conventional mechanism through reducing the number of constraints. The quantity of removed constraints is determined by the target mobility, which must be greater than zero for a mechanism. In general, an optimum design demands a single input to actuate the whole assembly. Moreover, with fewer degrees of freedom, it is easier to control the assembly, which is a particularly desired feature for space structures. Therefore the target mobility is set to one.

With the radial symmetry being preserved, two prototypes have been proposed, which are depicted in Figure 4.8. The first one is called the *Absent Panels Pattern*, denoted as Ω_4, which removes facets from the circumambient panels. The other one is called the *Trimmed Creases Pattern* (Ω_5), where some creases are broken to isolate neighbouring panels. Note that the gaps on Ω_5 are deliberately created for clarity and their actual positions are denoted by grey dashed lines. Both designs have triangulated the hexagonal hub and eliminated the locally obstructive elements τ to enable rigid deployment.

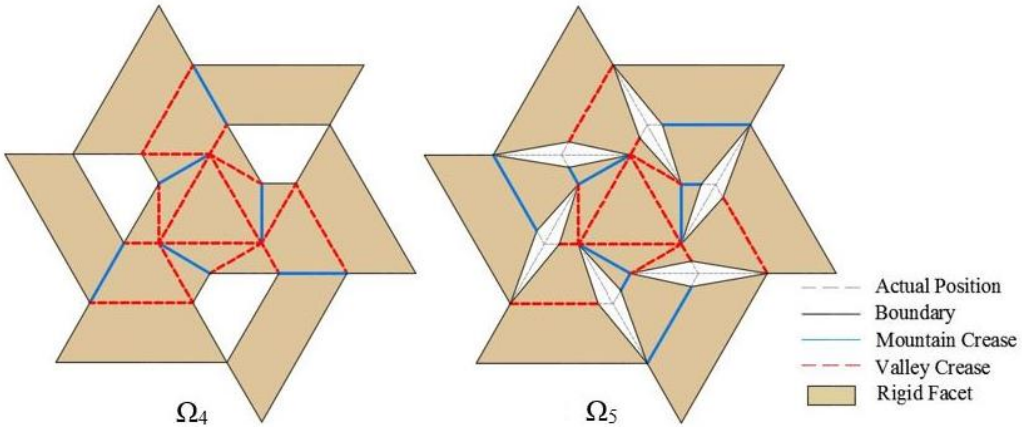

Figure 4.8 The proposed origami prototypes: (Ω_4) the Absent Panels Pattern and (Ω_5) the Trimmed Creases Pattern.

4.2.2 Pin-jointed frame construction

Next, the rigid foldability of the proposed prototypes will be examined using the mechanical modelling method proposed by Kumar and Pellegrino (2000), as reviewed in Section 2.2. With some facets being removed, the loop closure condition around each vertex will be broken. The assembly is therefore turned into a system consisting of multiple open loops. If the matrix method is applied, it will demand a large quantity of input variables to be assigned. However, the mechanical modelling method can deal with open loop problems with ease, due to its independence on loop-closure conditions. This is done by transforming origami patterns to pin-jointed frames, where the fold lines are modelled as links and the vertices as ball joints.

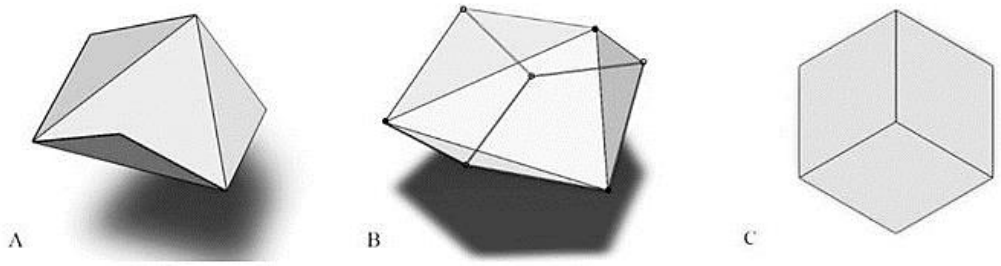

Figure 4.9 The hexagonal hub design

There are some key points that need to be noted for this transformation. First, a different transformation principle is applied to the hexagonal hub. According to the preliminary design, the hub should allow out-of-plane motion with one degree of freedom. Whereas by replacing creases and vertices with links and ball joints, the transformed frame of the hub possesses three independent mechanisms, where the three obtuse triangles may be turned upwards or downwards independently as illustrated in Figure 4.9-A. Therefore a new layout has been applied where three rigid bars are interconnected at the centre of the hexagon (Figure 4.9-B). With the three joints on the hub periphery being fully constrained, the centre node is allowed vertical movement only. This arrangement synchronizes the movement of the three obtuse triangles and leads to a single mobility. Conversely, if these three bars are directly transformed to creases of an origami pattern, the whole assembly will become a rigid structure (Figure 4.9-C) which equates to an intact hexagon. Consequently, the layout shown in Figure 4.9-B is selected.

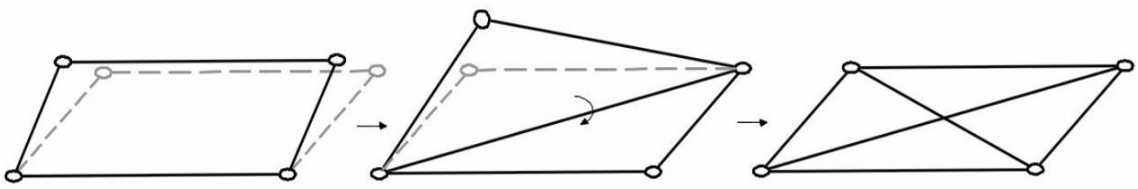

Figure 4.10 A quadrangular frame is constrained with a pair of cross links to eliminate internal distortion

Another notable point for frame construction is the measures required to restrain the trivial internal movement. Due to the instability of quadrangles, the facets are commonly triangulated by adding diagonals to eliminate lateral movement. However, a triangulated facet can still be bent along the diagonal bar unless a second rigid bar has been applied to inhibit the variation of distance between the other two diagonal nodes (Figure 4.10). Compared to Schenk and Guest (2011) who utilized extra vector inspection, this method only adds a pair of crossed links, which reduces computational time significantly.

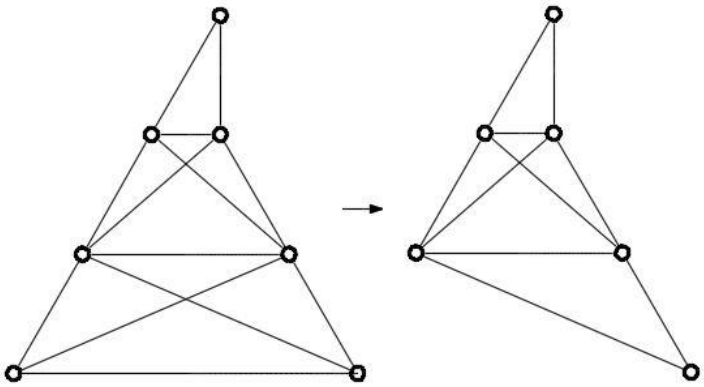

Figure 4.11 Simplification of the pin-jointed frame

Finally, the outmost trapeziums can be replaced with triangles for the sake of simplicity. Literature review indicates that the mechanical modelling method requires a prolonged period of time for manual work to define the geometric relationship for each bar. This means complexity is positively correlated with the quantity of the bars. The outmost facets have two free ends, and thus, they can have any shape as long as rigidity is preserved. By substituting trapeziums with triangles, a total of eighteen bars are removed without affecting the kinematics of the assembly (Figure 4.11). Therefore the computation process has been greatly simplified.

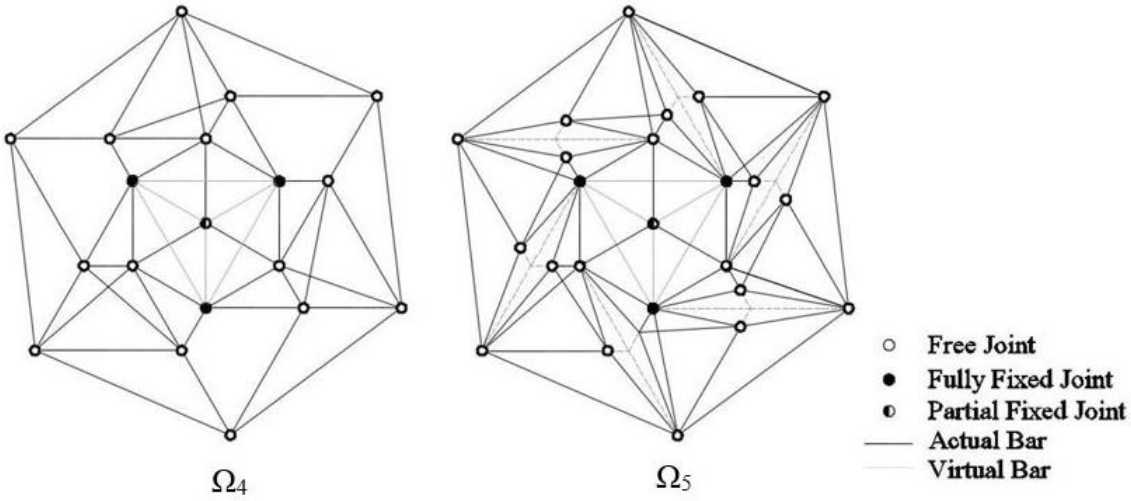

Figure 4.12 The pin-jointed frames transformed from the proposed origami prototypes: (Ω_4) the Absent Panels Pattern and (Ω_5) the Trimmed Creases Pattern.

With these points being considered, the two proposed prototypes have been transformed to pin-jointed frames (Figure 4.12). It is noted that all fixed points should be virtually connected to each other for the mobility calculation (denoted by grey solid lines in Figure 4.12). The central node has one special mobility as it is allowed to move only in and out the paper. Now $n = 51, j = 83$ and $f_i = 3$. The mobility of both assemblies is verified by the Kutzbach criterion, with the idle degrees of freedom being removed. Substituting the number of bars and joints into Eq. 2.1b, the mobility of Ω_4 is calculated as

$$m = 6(n - j - 1) + \sum_{i=1}^{j} f_i = 6 \times (51 - 83 - 1) + (3 \times 83 + 1) - 51 = 1. \quad (4.7)$$

Similarly, for Ω_5 where $n = 69, j = 113$ and $f_i = 3$, the mobility is

$$m = 6 \times (69 - 113 - 1) + (3 \times 113 + 1) - 69 = 1. \quad (4.8)$$

Consequently, both configurations have a single mobility, which is ideal for solar receiver structures.

4.2.3 Folding simulation of *the Absent Panels Pattern*

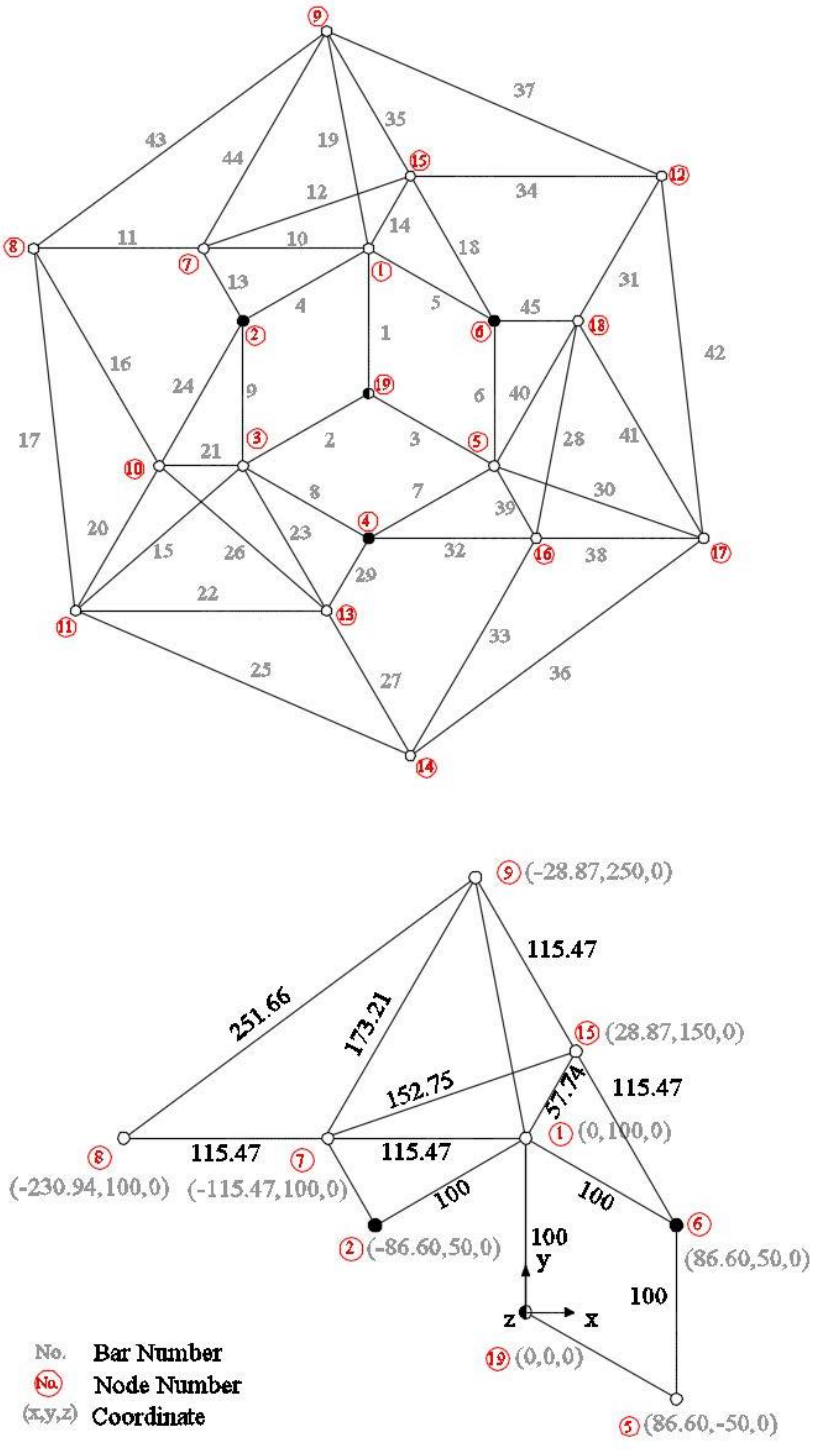

Figure 4.13 Schematic diagram of the pin-jointed frame from Ω_4.

The first step, in order to carry out numerical simulation, is to construct an equilibrium matrix **H** in the fully flat state. The framework is then made into a Cartesian coordinate

system, where bar lengths, axis and origin are defined, respectively, as shown by Figure 4.13. With the nodes 2, 4 and 6 being fully fixed to the ground, this assembly consists of $j_n = 15$ free nodes, a partially constrained node 19 and $b = 45$ bars. Therefore, this giant matrix has $3 \times 15 + 1 = 46$ rows and 45 columns. Since no external load $\mathbf{p}$ is applied, Eq. 2.8 becomes

$$\mathbf{Ht} = \mathbf{0}. \tag{4.9}$$

For convenience, the conventional bar forces $\boldsymbol{t}$ are replaced with force coefficient $\boldsymbol{\varepsilon}$. This is done by dividing the force $\boldsymbol{t}$ of each bar by its length, as

$$\boldsymbol{\varepsilon} = \frac{\boldsymbol{t}}{\boldsymbol{l}}. \tag{4.10}$$

The equilibrium matrix $\mathbf{H}$ is then simplified to a new matrix $\mathbf{H}'$ with multiple pairs of nodal coordinates only and thus Eq. 4.9 becomes

$$\mathbf{H}'\boldsymbol{\varepsilon} = \mathbf{0}. \tag{4.11}$$

Expanding Eq. 4.11 gives a system of equilibrium equations, which are

$$(x_v - x_r) \times \varepsilon_{vr} + (x_v - x_u) \times \varepsilon_{vu} + \cdots + (x_v - x_w) \times \varepsilon_{vw} = 0, \tag{4.12a}$$

$$(y_v - y_r) \times \varepsilon_{vr} + (y_v - y_u) \times \varepsilon_{vu} + \cdots + (y_v - y_w) \times \varepsilon_{vw} = 0, \tag{4.12b}$$

$$(z_v - z_r) \times \varepsilon_{vr} + (z_v - z_u) \times \varepsilon_{vu} + \cdots + (z_v - z_w) \times \varepsilon_{vw} = 0. \tag{4.12c}$$

The analysis is carried out node by node. Starting from node 1, as shown by Figure 4.13, this free node is connected to the nodes 19, 2, 6, 7, 15 and 9 via the bars 1, 4, 5, 10, 14 and 19. The equilibrium equations are therefore

$$\begin{aligned}(x_1 - x_{19}) \times \varepsilon_1 + (x_1 - x_2) \times \varepsilon_4 + (x_1 - x_6) \times \varepsilon_5 + (x_1 - x_7) \times \varepsilon_{10} \\ + (x_1 - x_{15}) \times \varepsilon_{14} + (x_1 - x_9) \times \varepsilon_{19} = 0,\end{aligned} \tag{4.13a}$$

$$(y_1 - y_{19}) \times \varepsilon_1 + (y_1 - y_2) \times \varepsilon_4 + (y_1 - y_6) \times \varepsilon_5 + (y_1 - y_7) \times \varepsilon_{10} + (y_1 - y_{15}) \times \varepsilon_{14} + (y_1 - y_9) \times \varepsilon_{19} = 0, \tag{4.13b}$$

$$(z_1 - z_{19}) \times \varepsilon_1 + (z_1 - z_2) \times \varepsilon_4 + (z_1 - z_6) \times \varepsilon_5 + (z_1 - z_7) \times \varepsilon_{10} + (z_1 - z_{15}) \times \varepsilon_{14} + (z_1 - z_9) \times \varepsilon_{19} = 0. \tag{4.13c}$$

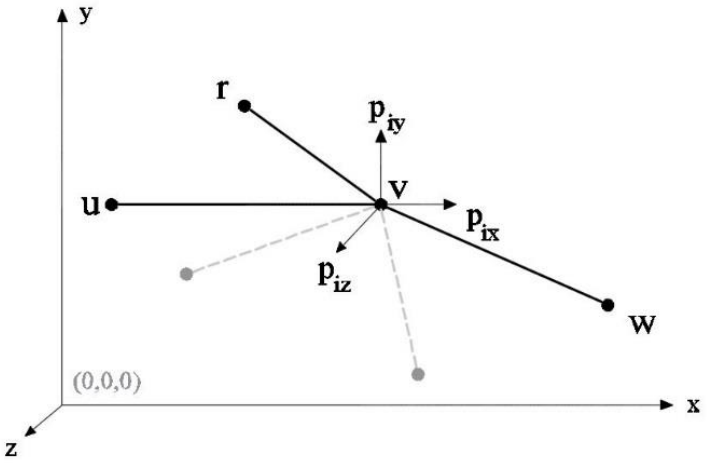

Figure 4.14 The sum of internal forces in equilibrium with external loads.

Transforming these linear equations into a matrix form requires the force coefficients to be separated, forming a vector $\boldsymbol{\varepsilon}$ with size 45×1, which is

$$\boldsymbol{\varepsilon} = [\varepsilon_1, \varepsilon_2, \varepsilon_3, \dots, \varepsilon_{44}, \varepsilon_{45}]^T. \tag{4.14}$$

Accordingly, the corresponding pairs of coordinates are listed in the k^{th} column in the matrix $\mathbf{H}'$, where k is the sequential number of bars. For example, for bar 4 ($k = 4$), the entries are

$$\mathbf{H}'_{(1,4)} = x_1 - x_2, \tag{4.15a}$$

$$\mathbf{H}'_{(2,4)} = y_1 - y_2, \tag{4.15b}$$

$$\mathbf{H}'_{(3,4)} = z_1 - z_2. \tag{4.15c}$$

The completed equilibrium matrix for node 1 is listed as follows,

*Table 4.4 The matrix **H'** for node 1*

H′	**1**	**…**	**4**	**5**	**…**	**10**	**…**	**14**	**…**	**19**	**…**
$\boldsymbol{F_{1x}}$	$x_1 - x_{19}$	0	$x_1 - x_2$	$x_1 - x_6$	0	$x_1 - x_7$	0	$x_1 - x_{15}$	0	$x_1 - x_9$	0
$\boldsymbol{F_{1y}}$	$y_1 - y_{19}$	0	$y_1 - y_2$	$y_1 - y_6$	0	$y_1 - y_7$	0	$y_1 - y_{15}$	0	$y_1 - y_9$	0
$\boldsymbol{F_{1z}}$	$z_1 - z_{19}$	0	$z_1 - z_2$	$z_1 - z_6$	0	$z_1 - z_7$	0	$z_1 - z_{15}$	0	$z_1 - z_9$	0

The coordinates of every nodes are substituted into the matrix H'. The results are shown in Table 4.5.

*Table 4.5 The matrix **H'** for node 1 with substituted coordinates*

H′	**1**	**…**	**4**	**5**	**…**	**10**	**…**	**14**	**…**	**19**	**…**
$\boldsymbol{F_{1x}}$	0	0	86.60	−86.60	0	115.47	0	−28.87	0	28.87	0
$\boldsymbol{F_{1y}}$	100	0	50	50	0	0	0	−50	0	−150	0
$\boldsymbol{F_{1z}}$	0	0	0	0	0	0	0	0	0	0	0

The same procedure was then followed with each free node occupying three rows in $\mathbf{H}'$. For the partially constrained node 19, however, it contributes a single row as the node is allowed to move along the z-direction only. Hence we have

$$(z_{19} - z_1) \times \varepsilon_1 + (z_{19} - z_3) \times \varepsilon_2 + (z_{19} - z_5) \times \varepsilon_3 = 0. \tag{4.16}$$

So far, the matrix $\mathbf{H}'$ with size 46×45 has been constructed. Dividing each column by its corresponding bar length *l* gives the original equilibrium matrix **H**. To carry out the matrix calculation, the lengths of 45 bars are firstly formed in a 1×45 vector $\mathbf{L}'$, where

$$\mathbf{L}' = [100, 100, 100, 100, \dots, 251.66, 251.66, 173.21, 57.74]. \tag{4.17}$$

Matrix division requires the dimensions of both matrices to agree, thus $\mathbf{L}'$ is repeated 46 times vertically to form the matrix **L** with size 46×45. So we have

$$\mathbf{H} = \frac{\mathbf{H}'}{\mathbf{L}}. \tag{4.18}$$

The entries for node 1 are shown in Table 4.6.

*Table 4.6 The matrix **H** for node 1*

H	**1**	**...**	**4**	**5**	**...**	**10**	**...**	**14**	**...**	**19**	**...**
$\boldsymbol{F_{1x}}$	0	0	0.87	−0.87	0	1	0	−0.50	0	0.19	0
$\boldsymbol{F_{1y}}$	1	0	0.50	0.50	0	0	0	−0.87	0	−0.98	0
$\boldsymbol{F_{1z}}$	0	0	0	0	0	0	0	0	0	0	0

Based on the kinematic-static duality, the compatibility matrix $\mathbf{C} = \boldsymbol{H^T}$. Substituting $\mathbf{C}$ to Eq. 2.9 yields

$$\mathbf{Cd} = \mathbf{0}. \tag{4.19}$$

The nodal displacement $\mathbf{d_i}$ has a size of 46×1. Each entry suggests a displacement of a non-fully-fixed node along a particular direction, which is

$$\mathbf{d_i} = [\mathrm{d}_{1x}, \mathrm{d}_{1y}, \mathrm{d}_{1z}, \mathrm{d}_{3x}, \mathrm{d}_{3y}, \mathrm{d}_{3z}, \dots, \mathrm{d}_{18z}, \mathrm{d}_{19z}]^T. \tag{4.20}$$

By solving the null space of the matrix **C**, we have

$$\mathbf{d_1} = [0, 0.0028, 0.1384, -0.0024, -0.0014, \dots, 0.1775, -0.1384]^T. \tag{4.21}$$

Then a parameter Δ_i is introduced to control the magnitude and direction of the nodal displacement, $\mathbf{d_i}$. Generally, a smaller displacement indicates a higher accuracy for this predictor step but it also requires a larger number of iterations. Through a number of tests, it can be founded that, in this case, when the step length is smaller than or equal to 0.2, the designated acceptable error range can be achieved, where the detailed error range determination will be explained later in this chapter. Therefore, to minimize the number of

iterations, $\Delta_1 = 0.2$ is stipulated. Hence, from Eq. 2.13, the next configuration $\mathbf{\Psi_2}$ is predicted by

$$\mathbf{\Psi_2} = \mathbf{\Psi_1'} + \Delta_1 \times \mathbf{d_1}. \tag{4.22}$$

For successive iterations, the direction of motion is supposed to keep consistent so the assembly moves along a desired forward path. However, it is not guaranteed that solving the null space of the compatibility matrix **C** automatically generates direction-constant displacement $\mathbf{d_i}$ for each step. Thus, a detection step is introduced by checking the dot product of two successive predictor steps. If

$$\mathbf{d_{i-1}} \cdot \mathbf{d_i} < 0, \tag{4.23}$$

the sign of Δ is reversed as

$$\Delta_i = -\Delta_{i-1}. \tag{4.24}$$

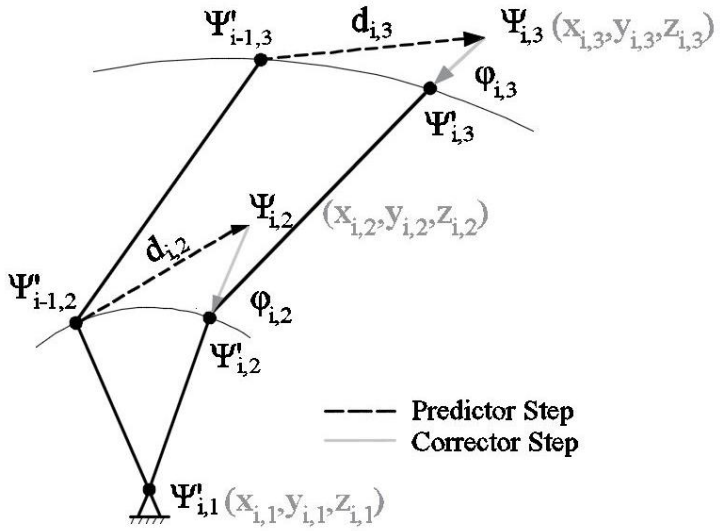

Figure 4.15 Schematic diagram of the predict-correct approach

Before proceeding to the next step, the bar lengths need to be checked to ensure rigidity. Consider a fully constrained node 1 and two free nodes 2 and 3 are connected by two bars with length $l_{i-1,12}$ and $l_{i-1,23}$ (Figure 4.15). After the i^{th} predictor step, as denoted by the dashed line, the two unconstrained nodes 2 and 3 are displaced to the new positions

$\boldsymbol{\Psi_{i,2}}(x_{i,2}, y_{i,2}, z_{i,2})$ and $\boldsymbol{\Psi_{i,3}}(x_{i,3}, y_{i,3}, z_{i,3})$. In this process, the bars may be extended or shortened to attain the predicted positions. Therefore correctors $\varphi_{i,2}$ and $\varphi_{i,3}$ are applied to drag the two nodes to the strain-free positions $\boldsymbol{\Psi'_{i,2}}$ and $\boldsymbol{\Psi'_{i,3}}$. For convenience, we stipulate that these nodes are dragged towards the reference points $\boldsymbol{\Psi_{i,1}}$ and $\boldsymbol{\Psi_{i,2}}$. Therefore, the coordinates of $\boldsymbol{\Psi'_{i,2}}$ are

$$(x_{i,2} - \frac{x_{i,2} - x_{i,1}}{l_{i-1,12}}\varphi_{i,2}, y_{i,1} - \frac{y_{i,2} - y_{i,1}}{l_{i-1,12}}\varphi_{i,2}, z_{i,1} - \frac{z_{i,2} - z_{i,1}}{l_{i-1,12}}\varphi_{i,2}). \quad (4.25)$$

Similarly, the coordinates of $\boldsymbol{\Psi'_{i,3}}$ are

$$(x_{i,3} - \frac{x_{i,3} - x_{i,2}}{l_{i-1,23}}\varphi_{i,3}, y_{i,1} - \frac{y_{i,3} - y_{i,2}}{l_{i-1,23}}\varphi_{i,3}, z_{i,1} - \frac{z_{i,3} - z_{i,2}}{l_{i-1,23}}\varphi_{i,3}). \quad (4.26)$$

The optimum corrector should enable the bar length to remain unchanged, which is

$$l_{i,23} = l_{i-1,23}, \quad (4.27)$$

where

$$\begin{aligned} l_{i,23} = \sqrt{\left(\left(x_{i,3} - \frac{x_{i,3} - x_{i,2}}{l_{i-1,23}}\varphi_{i,3} - x_{i,2} + \frac{x_{i,2} - x_{i,1}}{l_{i-1,12}}\varphi_{i,2}\right)^2\right.} \\ + \left(y_{i,3} - \frac{y_{i,3} - y_{i,2}}{l_{i-1,23}}\varphi_{i,3} - y_{i,2} + \frac{y_{i,2} - y_{i,1}}{l_{i-1,12}}\varphi_{i,2}\right)^2 \\ \left. + \left(z_{i,3} - \frac{z_{i,3} - z_{i,2}}{l_{i-1,23}}\varphi_{i,3} - z_{i,2} + \frac{z_{i,2} - z_{i,1}}{l_{i-1,12}}\varphi_{i,2}\right)^2\right). \end{aligned} \quad (4.28)$$

Rearranging Eq. 4.28, we have

$$\begin{aligned} f(\varphi_{i,2}, \varphi_{i,3}) = \left(x_{i,3} - \frac{x_{i,3} - x_{i,2}}{l_{i-1,23}}\varphi_{i,3} - x_{i,2} + \frac{x_{i,2} - x_{i,1}}{l_{i-1,12}}\varphi_{i,2}\right)^2 \\ + \left(y_{i,3} - \frac{y_{i,3} - y_{i,2}}{l_{i-1,23}}\varphi_{i,3} - y_{i,2} + \frac{y_{i,2} - y_{i,1}}{l_{i-1,12}}\varphi_{i,2}\right)^2 \\ + \left(z_{i,3} - \frac{z_{i,3} - z_{i,2}}{l_{i-1,23}}\varphi_{i,3} - z_{i,2} + \frac{z_{i,2} - z_{i,1}}{l_{i-1,12}}\varphi_{i,2}\right)^2 - l_{i,23}^2 = 0. \end{aligned} \quad (4.29)$$

To solve the correctors, Eq. 4.29 is linearised by the Taylor series with respect to two variables $\varphi_{i,2}$ and $\varphi_{i,3}$. As the amplitudes of the correctors are very small, the function is approximated in the region of zero for both variables. Keeping the linear terms only, we have

$$f(\varphi_{i,2}, \varphi_{i,3}) = f(0,0) + \frac{\partial f(0,0)}{\partial \varphi_{i,2}} \varphi_{i,2} + \frac{\partial f(0,0)}{\partial \varphi_{i,3}} \varphi_{i,3}, \tag{4.30}$$

where

$$f(0,0) = (x_{i,3} - x_{i,2})^2 + (y_{i,3} - y_{i,2})^2 + (z_{i,3} - z_{i,2})^2 - l_{i,23}^2, \tag{4.31a}$$

$$\frac{\partial f(0,0)}{\partial \varphi_{i,2}} = 2\left(\frac{x_{i,2} - x_{i,1}}{l_{i-1,12}}\right)(x_{i,3} - x_{i,2}) + 2\left(\frac{y_{i,2} - y_{i,1}}{l_{i-1,12}}\right)(y_{i,3} - y_{i,2}) + 2\left(\frac{y_{i,2} - y_{i,1}}{l_{i-1,12}}\right)(y_{i,3} - y_{i,2}), \tag{4.31b}$$

$$\frac{\partial f(0,0)}{\partial \varphi_{i,3}} = -2\left(\frac{x_{i,3} - x_{i,2}}{l_{i-1,23}}\right)(x_{i,3} - x_{i,2}) - 2\left(\frac{y_{i,3} - y_{i,2}}{l_{i-1,23}}\right)(y_{i,3} - y_{i,2}) - 2\left(\frac{z_{i,3} - z_{i,2}}{l_{i-1,23}}\right)(z_{i,3} - z_{i,2}). \tag{4.31c}$$

Substituting Eq. 4.31 into Eq. 4.30 gives

$$\begin{aligned} &-\frac{2\varphi_{i,2}}{l_{i-1,12}}\big((x_{i,2} - x_{i,1})(x_{i,3} - x_{i,2}) + (y_{i,2} - y_{i,1})(y_{i,3} - y_{i,2}) + (z_{i,2} - z_{i,1}) \\ &(z_{i,3} - z_{i,2})\big) + \frac{2\varphi_{i,3}}{l_{i-1,23}}\big((x_{i,3} - x_{i,2})^2 + (y_{i,3} - y_{i,2})^2 + (z_{i,3} - z_{i,2})^2\big) \\ &= (x_{i,3} - x_{i,2})^2 + (y_{i,3} - y_{i,2})^2 + (z_{i,3} - z_{i,2})^2 - l_{i,23}^2. \end{aligned} \tag{4.32}$$

Similarly, for the bar between the fixed node O_1 and the free node O_2, the length can be correct by simply setting $\varphi_{i,1} = 0$. The linear equation for $l_{i,12}$ is

$$\begin{aligned} &\frac{2\varphi_{i,2}}{l_{i-1,12}}\big((x_{i,2} - x_{i,1})^2 + (y_{i,2} - y_{i,1})^2 + (z_{i,2} - z_{i,1})^2\big) \\ &= (x_{i,2} - x_{i,1})^2 + (y_{i,2} - y_{i,1})^2 + (z_{i,2} - z_{i,1})^2 - l_{i,12}^2. \end{aligned} \tag{4.33}$$

So far, we have a system of two linear equations with two unknown correctors $\varphi_{i,2}$ and $\varphi_{i,3}$, which can be solved simultaneously. For convenience, the equations are transformed into a matrix form

$$\mathbf{A_i \Phi_i = B_i}. \tag{4.34}$$

$\mathbf{A_i}$ is a 2×2 matrix, the entries are

$$A_{(1,1)} = \frac{2}{l_{i-1,12}}\left(\left(x_{i,2} - x_{i,1}\right)^2 + \left(y_{i,2} - y_{i,1}\right)^2 + \left(z_{i,2} - z_{i,1}\right)^2\right), \tag{4.35a}$$

$$A_{(1,2)} = 0, \tag{4.35b}$$

$$A_{(2,1)} = -\frac{2}{l_{i-1,12}}\left(\left(x_{i,2} - x_{i,1}\right)\left(x_{i,3} - x_{i,2}\right) + \left(y_{i,2} - y_{i,1}\right)\left(y_{i,3} - y_{i,2}\right) + \left(z_{i,2} - z_{i,1}\right)\left(z_{i,3} - z_{i,2}\right)\right), \tag{4.35c}$$

$$A_{(2,2)} = \frac{2}{l_{i-1,23}}\left(\left(x_{i,3} - x_{i,2}\right)^2 + \left(y_{i,3} - y_{i,2}\right)^2 + \left(z_{i,3} - z_{i,2}\right)^2\right). \tag{4.35d}$$

$\mathbf{\Phi_i}$ is a 2×1 matrix, where

$$\mathbf{\Phi_i} = \begin{bmatrix}\varphi_{i,2} \\ \varphi_{i,3}\end{bmatrix}. \tag{4.36}$$

$\mathbf{B_i}$ is a 2×1 matrix, where

$$\mathbf{B_i} = \begin{bmatrix}\left(x_{i,2} - x_{i,1}\right)^2 + \left(y_{i,2} - y_{i,1}\right)^2 + \left(z_{i,2} - z_{i,1}\right)^2 - l_{i,12}^2 \\ \left(x_{i,3} - x_{i,2}\right)^2 + \left(y_{i,3} - y_{i,2}\right)^2 + \left(z_{i,3} - z_{i,2}\right)^2 - l_{i,23}^2\end{bmatrix}. \tag{4.37}$$

Therefore the corrector matrix $\mathbf{\Phi_i}$ can be solved by using the inverse matrix, which is

$$\mathbf{\Phi_i = B_i A_i^{-1}}. \tag{4.38}$$

Substituting the nodal coordinates of $\mathbf{\Psi_2}$ into Eq. 4.38 gives

$$\boldsymbol{\Phi_2} = 10^{-5} \times [\begin{matrix} \text{-2.11} & \text{-2.14} & 0.34 & 6.26 & 0.91 & 4.76 & 2.18 & 5.31 \\ 3.27 & 7.42 & 4.25 & 0.29 & 0.85 & 4.21 & 3.46 & \text{-73.11} \end{matrix}]^T. \quad (4.39)$$

It is noted that this linear system does not guarantee equal numbers of equations and unknowns. Generally, an assembly consists of *b* linearly independent equations, which are greater than or equal to the number of unknown correctors, j_n. For instance, Ω_4 contains 45 bars and 16 non-fully-constrained nodes. The linearly independent equations are more than the unknown parameters thus an overconstrained system is formed. In this occasion, the inverse of the non-square matrix $\mathbf{A_i}$ does not exist. The corrector matrix $\boldsymbol{\Phi_i}$ is obtained by

$$\boldsymbol{\Phi_i} = \mathbf{B_i A_i^+}. \quad (4.40)$$

$\mathbf{A_i^+}$ is the Moore–Penrose pseudo inverse matrix of $\mathbf{A_i}$, which can be calculated by using the singular value decomposition (SVD). If a b $\times$ j_n matrix $\mathbf{A_i}$ has the SVD, it can be factorized as

$$\mathbf{A_i} = \boldsymbol{U_i W_i V_i^T}, \quad (4.41)$$

where $\boldsymbol{U_i}$ and $\mathbf{V_i}$ are two square matrices and $\boldsymbol{W_i}$ is a rectangular matrix with size b $\times$ j_n. The matrix $\mathbf{A_i^+}$ can be calculated as

$$\mathbf{A_i^+} = \boldsymbol{V_i^T W_i^{-1} U_i}. \quad (4.42)$$

Substituting Eq. 4.42 to Eq. 4.40 yields an approximate solution of $\boldsymbol{\Phi_i}$ in the least square sense.

With the correctors being determined, a strain-free configuration $\boldsymbol{\Psi_2'}$ is obtained from

$$\boldsymbol{\Psi_2'} = \boldsymbol{\Psi_2} + \boldsymbol{\Phi_2}. \quad (4.43)$$

Note that as a numerical simulation approach, this produces an approximate answer, which involves inevitable errors. Therefore, an inspection step of bar length is introduced before proceeding to the next step. The strain of k^{th} bar at i^{th} step, ϵ_{ik}, is stipulated as

$$\epsilon_{ik} = \frac{|l_{ik} - l_{1k}|}{l_{1k}}. \tag{4.44}$$

To ensure accuracy, the corrector step may be repeated until a designated range of strain ϵ_{ik} is attained.

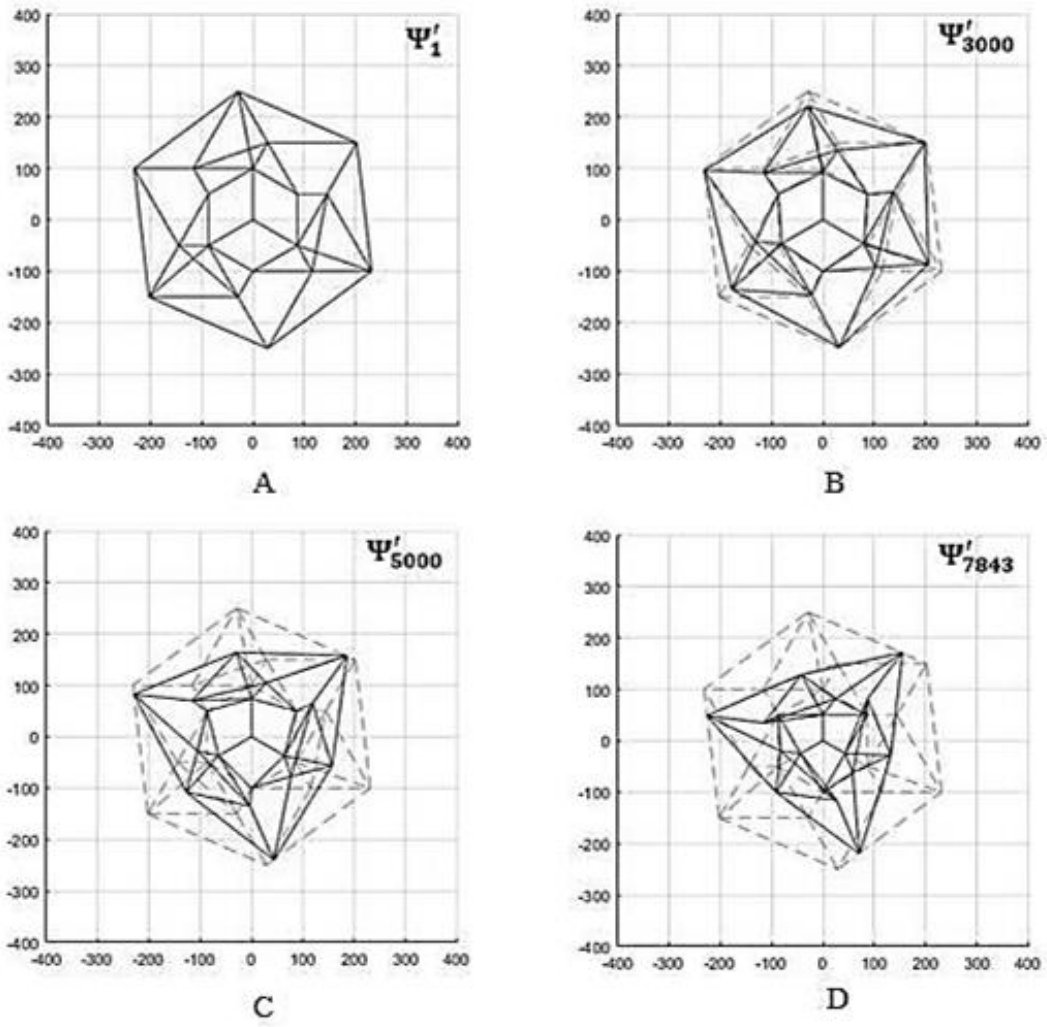

Figure 4.16 The folding sequence of Ω_4, projected on the x-y plane.

So far, a single predictor-corrector step has been completed, and the full range motion of Ω_4 is then simulated by successively iterating this algorithm. The starting configuration $\boldsymbol{\Psi}'_{\mathbf{1}}$

for Ω_4 is illustrated in Figure 4.16-A, which is in the fully flat state. The rank deficiency of equilibrium matrix $\mathbf{H}$ at $\boldsymbol{\Psi}_1'$ is 16, suggesting the assembly is at a bifurcation point with a large number of kinematic paths. A relatively desired path which preserves rotational symmetry is then selected through all aspects of contrast. Along this path, the pin-jointed frame takes 7843 steps to reach the most stowed configuration, given that the central node is allowed to have out-of-plane motion. The lengths of bars of this wrapping pattern range from 100.00 to 251.66. Based on this dimension, we stipulate an acceptable strain ϵ_{ik} of 10^{-5} to guarantee a high degree of accuracy. By inspection, the lengths of bars stay within the designated strain range throughout the entire process. Therefore, single-mobility wrapping of Ω_4 is considered to be inextensional. The trajectories of nodal displacement are illustrated in Figure 4.17.

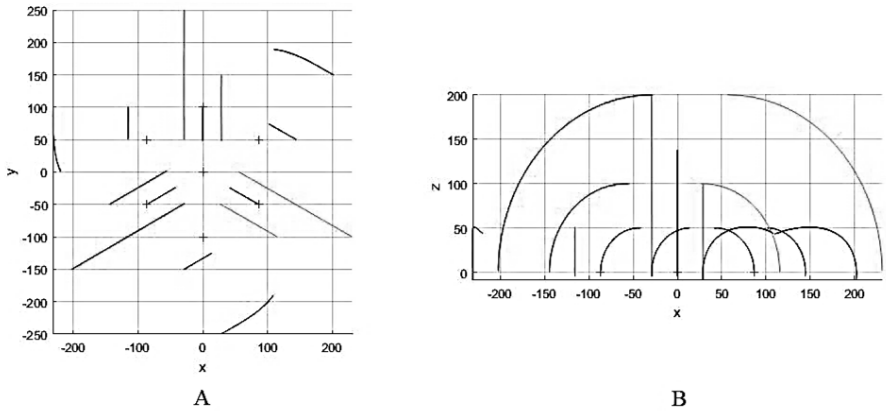

Figure 4.17 Projection of the trajectories of motion from Ω_4 on (A) the x-y plane and (B) the x-z plane.

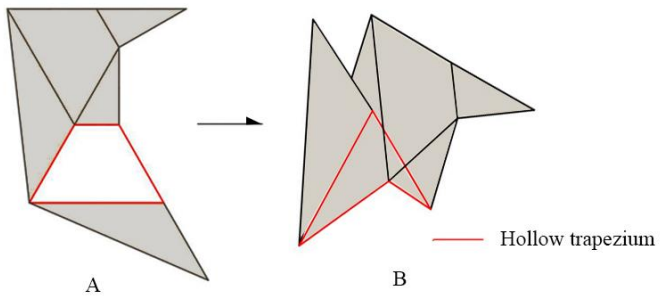

Figure 4.18 One of the three identical unit patterns in (A) the fully flat state and (B) the fully stowed state.

However, Ω_4 pattern has a number of drawbacks. The final configuration $\boldsymbol{\Psi'_{7843}}$ ends up with a less compact shape and a relatively small deployed-to-stowed ratio. This is due to the unbalanced arrangement, where only three out of six trapezoidal panels have been removed. Constraints on mobility and geometry only allow three panels to be removed out of six units from this rotationally symmetric assembly. Therefore the original six-unit layout is re-divided into three parts and the rigid deployment/folding is in fact reliant on the distortion of the three hollow trapeziums (Figure 4.18). During the folding process, all facets move upwards, as can be seen from the projection on the x-z plane. Consequently, a near-triangular shape is generated, which is clearly unsuitable for installation within a cylindrical rocket. Nonetheless, an ideal prototype enables the regular alternation of units moving up and down. Regardless of the opposite direction, the six units should have the same kinematics so a perfect hexagon can be expected in the fully folded state.

4.2.4 Folding simulation of *the Trimmed Creases Pattern*

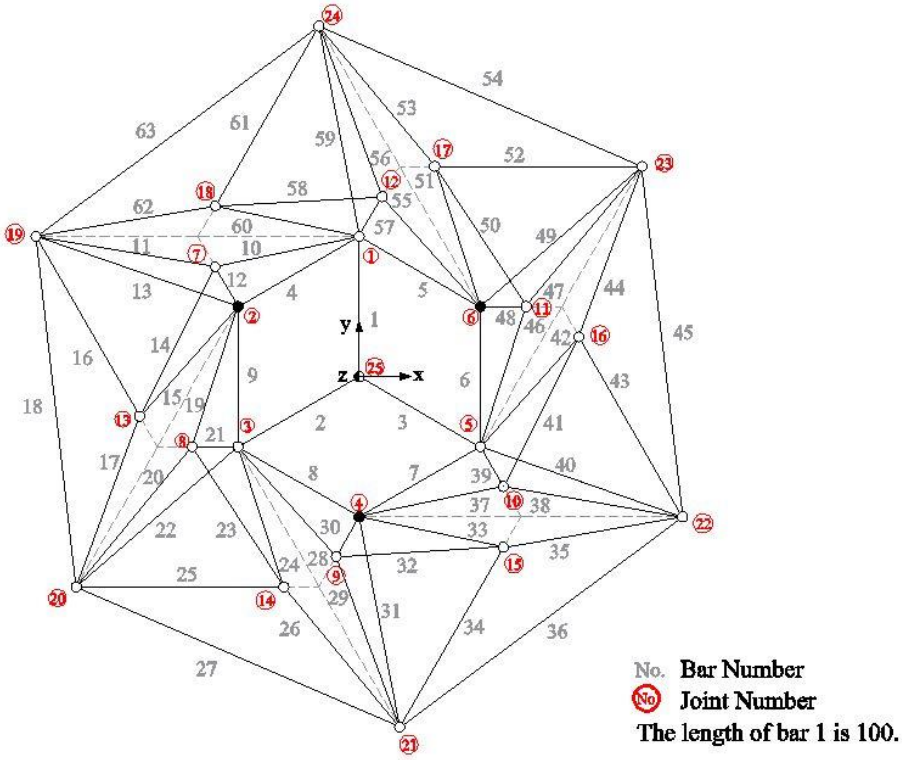

Figure 4.19 Schematic diagram of the pin-jointed frame of Ω_5

The Trimmed Creases Pattern (Ω_5) introduces gaps into circumjacent panels along six creases. As can been seen from Figure 4.19, a trimmed crease has been replaced by two identical folds overlapped at the original position of the fully deployed configuration. The actual positions are denoted by grey dashed lines, where the gaps are created for illustration. Thus the pattern has been divided into six units with rotational symmetry being preserved. Besides the three fully fixed nodes 2, 4 and 6, this assembly consists of 63 bars, 21 free nodes and 1 partially fixed node 25, forming an equilibrium matrix with size 64×63. Considering the whole assembly, generally, this prototype has one degree of freedom for general configurations. However, the 21 rank deficiencies in the starting configuration suggest the flat state is at a bifurcation point. According to the analysis of a paper model, a desired path was selected out of all potential inextensional mechanisms. It is noted that within each of the six units, there exists two locally internal mechanisms. The bars 16, 25, 34, 43, 52 and 61 can be either mountain folds or valley folds without affecting rigid foldability, thus the rotation direction of these bars needs to be predefined. Carrying out the iterative predictor-corrector algorithm, the six circumjacent units were actuated synchronously. To achieve an acceptable accuracy of bar length, a step length $\Delta_1 = 0.2$ was applied. After 9377 steps, the assembly has reached the fully stowed configuration. The folding sequence and the trajectories of motion are shown by Figure 4.20 and Figure 4.21, respectively.

According to both figures, the zero-thickness pattern ended up with a stowed configuration where the circumambient facets coincides with the verge of the hexagonal hub. This is the most compact form that can be achieved where no clearance exists between adjacent facets. The pairs of twin nodes, 7-18, are separated during the folding process, and overlapped again at the final state. The neighbouring units are thus slightly detached to release the potential strain from the unbroken winding membrane and a rigid transition can be

achieved. This is confirmed by the bar length inspection where no bar has been deformed over the designated range of error $\epsilon_{ik} = 10^{-5}$ throughout the entire folding/deployment. Therefore it can be concluded that Ω_5 can be folded to the desired stowed shape without altering the bar length. Along with the pattern proposed by Kumar and Pellegrino (2000), as shown in Figure 2.14-Ω_2, both prototypes can achieve rigid foldability with slightly lower stiffness than the original winding membrane (Ω_1). However, compared to Ω_2, Ω_5 does not require any surface to be flexed. Therefore Ω_5 is more feasible for solar panel arrays which are made of rigid and brittle materials.

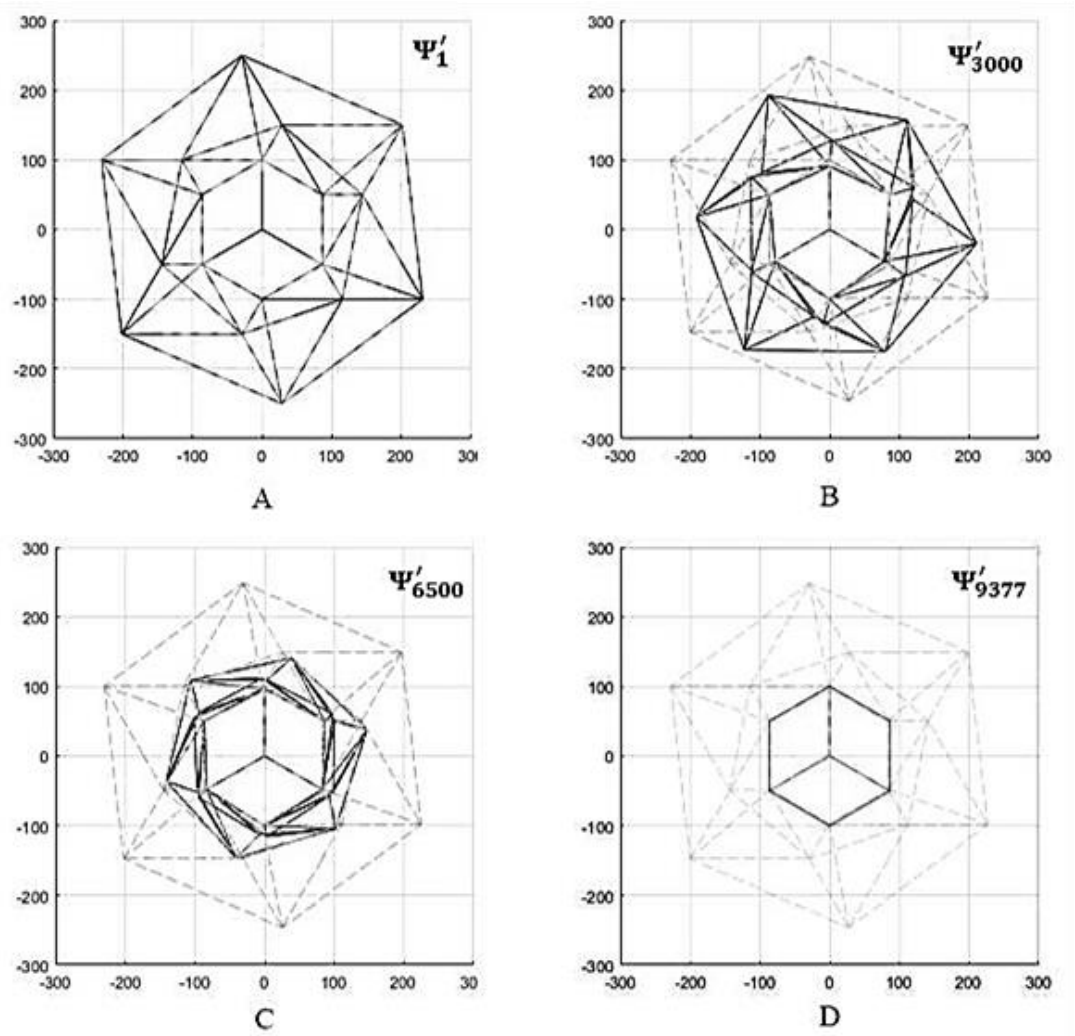

Figure 4.20 The folding sequence of Ω_5, projected on the x-y plane.

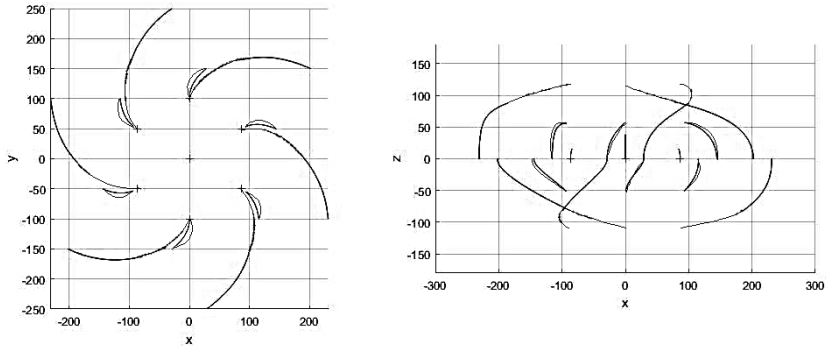

Figure 4.21 Projections of trajectories of motion from Ω_5 on (A) the x-y plane and (B) the x-z plane.

4.3 Extending the rigid foldable patterns to a multi-layer layout

Although both prototypes, Ω_2 and Ω_5, are capable of wrapping around a hexagonal hub inextensionally, their realisation on satellites requires a larger deployed-to-stowed ratio. Since the heights of the panels are constrained to equal to the side lengths of the hub, the surface area of a single panel is limited. Thus, the ratio can only be enlarged by increasing the quantities of panels. This is done by assigning more facets around the outer-ring of the previous two-layer layout. However, the rigid foldability and kinematics of the multi-layer assemblies are yet to be identified. Therefore, validation is firstly carried out for the three-layer layouts from the two inextensional wrapping prototypes.

Extending Ω_2 to three layers requires an extra 18 bars and 6 free nodes. In fact, this model requires consistently increased numbers of bars and nodes for each extended layer due to its strict radial symmetry. A three-layer layout of Ω_2 is illustrated in Figure 4.22, denoted as Ω_6 where $n = 69, j = 113$ and $f_i = 3$. The mobility of Ω_6 is calculated by the Kutzbach criterion, which is

$$m = 6 \times (69 - 113 - 1) + (3 \times 113 + 1) - 69 = 1. \qquad (4.45)$$

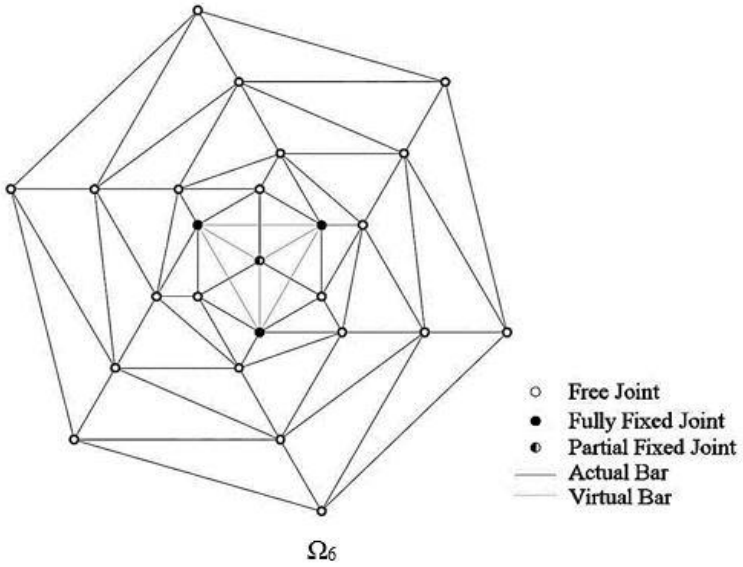

Figure 4.22 The pin-jointed frame of Ω_6.

The single degree of freedom is the optimum result for deployable membranes which can retain mobility and stiffness simultaneously. Again the mechanical modelling method is adopted to simulate the trajectories of motion and a larger equilibrium matrix with size 64×63 is obtained. Similarly, the predictor-corrector algorithm is applied with step length $\Delta_1 = 0.2$. The mobile assembly takes 10181 steps to reach the completely folded state. The folding sequence is illustrated in Figure 4.23.

The bar length inspection suggests that no bar has been deformed more than the acceptable range of strain $\epsilon_{ij} = 10^{-5}$ throughout the entire folding process. Thus, the assembly can be considered as strictly rigid foldable, with the hub node being permitted to move longitudinally. The rank deficiency of general configurations is one, confirming the single degree of freedom calculated from the Kutzbach criterion. Nonetheless, in the fully deployed configuration Ψ_1', the assembly has $q = 22$ independent mechanisms and $s = 21$ states of self-stress. This suggests the mobile structure is at a bifurcation point with numerous distinct potential paths.

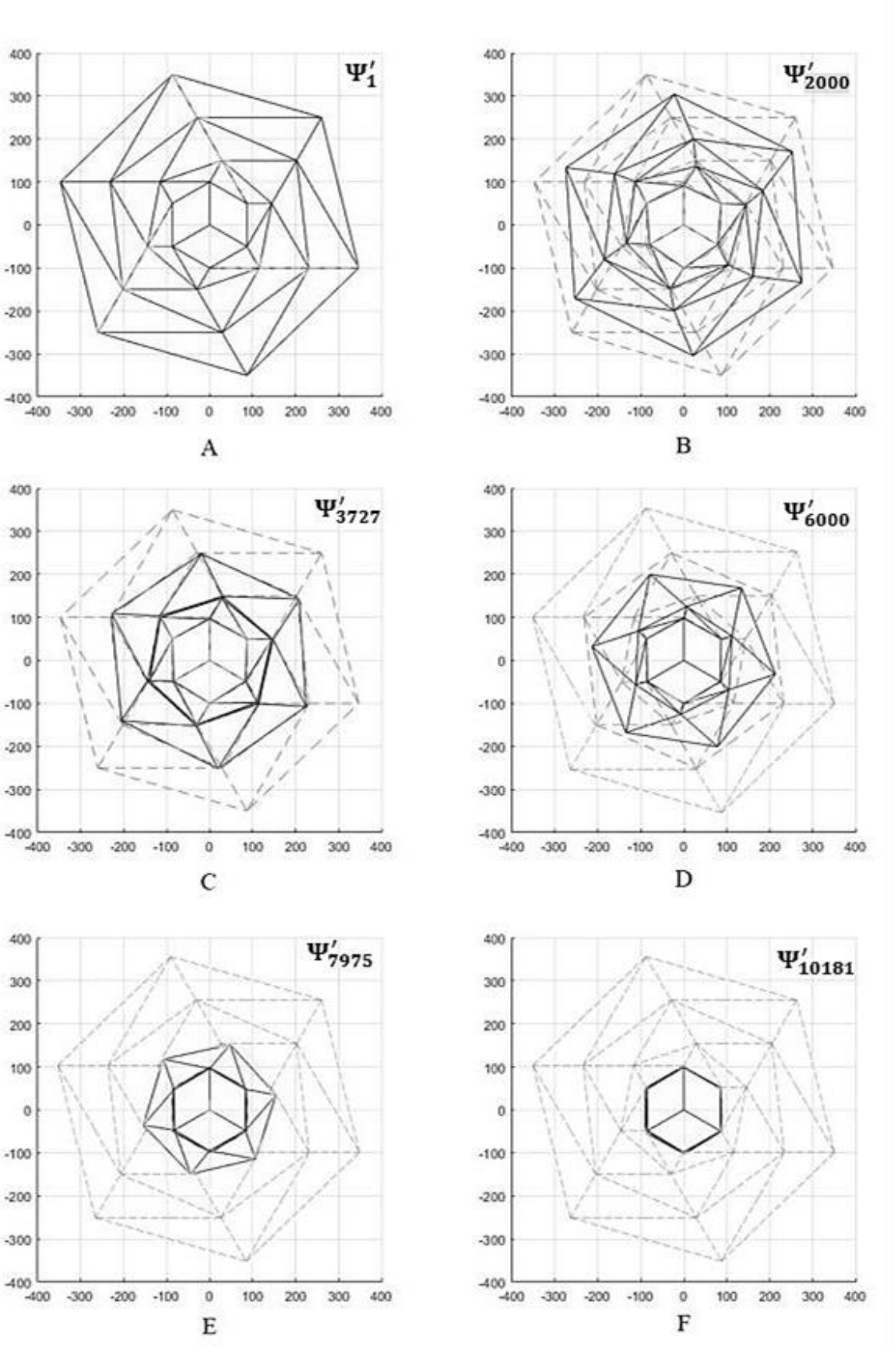

Figure 4.23 The folding sequence of Ω_6.

According to the motion of the physical model, a desired path was selected, where the diverse layers possess asynchronous motion. As illustrated in Figure 4.23, the middle loop of triangles is actuated first. The other two loops remain stationary until the motion of the middle loop has completely finished. The stowage of the middle loop terminates at the configuration Ψ'_{3727}, corresponding to the second kinematic bifurcation point. In fact, a bifurcation point is expected each time a loop stows completely, as denoted by Ψ'_{7975} and Ψ'_{10181}, respectively. It is noted that these bifurcation points cannot be avoided if the motion is reversed. When the pattern starts from stowed to expanded, it still preserves the strict rotational symmetric configuration, which will result in a kinematic bifurcation point before each loop deployment.

It is noted from the configuration that the circumambient loops presents the identical trajectories of motion with the previous two-layer layout. Alternative sequences of the loop folding are applicable, i.e. the movement could start from the inner layer or the outer layer without affecting the kinematics. This confirms the radial symmetry of the assembly. Therefore, Ω_6 is allowed to be extended to more than three layers to achieve a larger surface area. However, more loops of triangles lead to a greater number of bifurcation points. This is due to the strict rotational symmetry of the model where the corresponding bar lengths and sector angles are identical. Therefore, a path selection is required at each bifurcation point, which may cause faults when being deployed in space. This may be tackled by deliberately introducing imperfections in the designing process.

For Ω_5 which is cyclic asymmetric, the extension can be designed in a number of ways. The four possible extension schemes are shown in Figure 4.24.

To be mobile, the prototype has to impart positive degrees of freedom, where the optimum solution demands a single input to actuate the entire assembly. The pattern Ω_7 simply adds

a further layer of connected facets to the original two-layer Ω_5. Again, the mobility of Ω_7 is checked using the Kutzbach criterion.

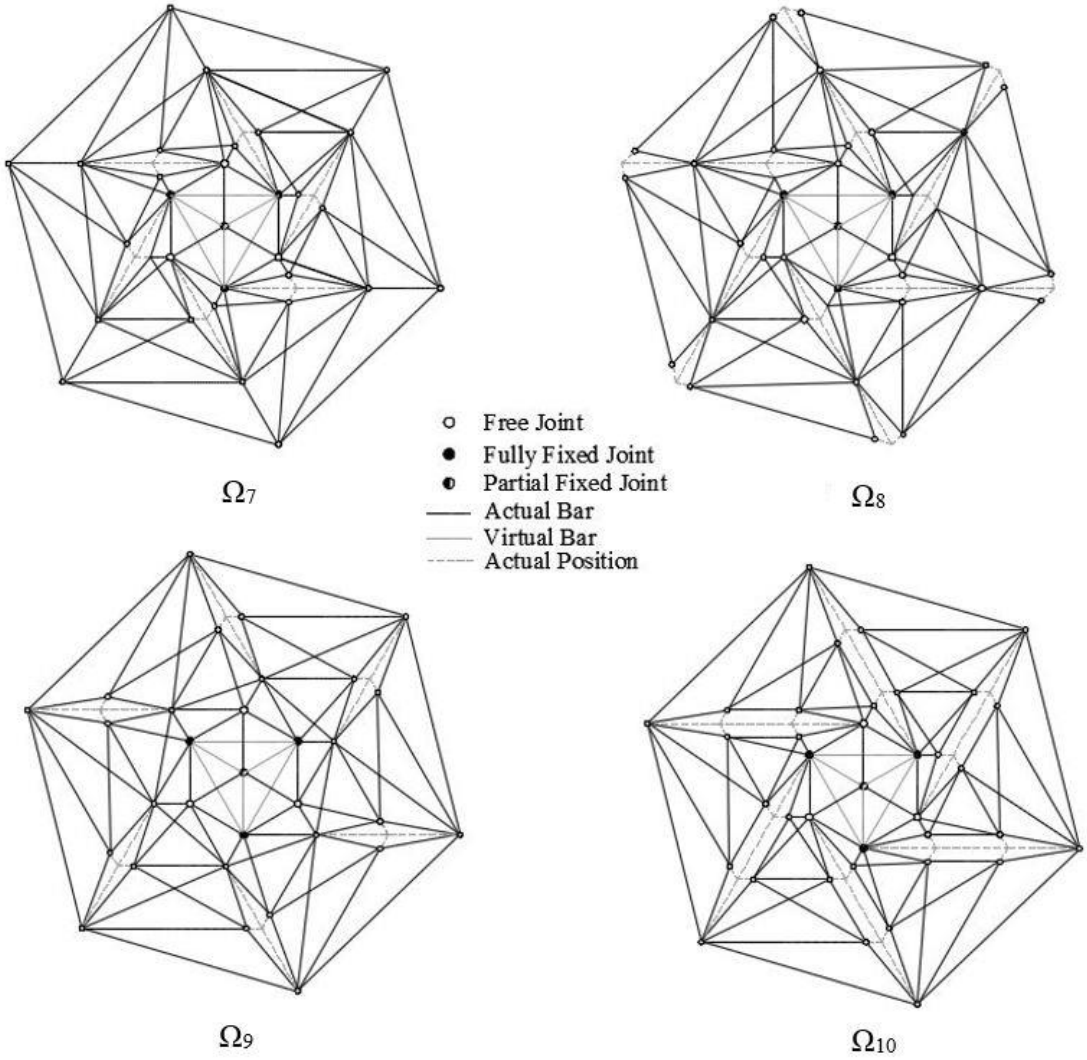

Figure 4.24 Designs of the three-layer Trimmed Crease Patterns.

For Ω_7 where $n = 93, j = 155$ and $f_i = 3$, the mobility is

$$m = 6 \times (93 - 155 - 1) + (3 \times 155 + 1) - 93 = -5. \qquad (4.46)$$

This suggests the newly added panels exert extra constraints on to the assembly, thus the pattern is turned into static structure. This is confirmed by the full rank of the equilibrium matrix **H**. Therefore the creases and nodes of the outmost panels have been sliced apart along the previous gashed line, as denoted by Ω_8. In this case, the outmost closed loop has

been broken and thus the mobility turns to 7. However, Ω_8 can be deemed as the six single triangular facets are directly connected to the original two-layer layout. The added panels each preserve an independent mechanism, which is considered as an invalid extension approach. Another pattern Ω_9 has been proposed by transforming the sliced area of Ω_7 to the outer layer but the negative mobility -5 remains unchanged. This means more constraints need to be eliminated to trigger inextensional movements. Therefore all three of the collinear radial creases have been gashed through, as denoted by Ω_{10} where $n = 99, j = 161$ and $f_i = 3$. The mobility of Ω_{10} is calculated as

$$m = 6 \times (99 - 161 - 1) + (3 \times 161 + 1) - 99 = 7. \quad (4.47)$$

The extra six degrees of freedom are generated from the internal mechanisms within the six constituting units, i.e., the crease can be either mountain or valley folds. Although more constraints are needed to eliminate the internal mechanisms, Ω_{10} is capable of wrapping inextensionally towards the most compact configuration. Thus, it is considered as a valid extension scheme.

Attempts have also been made to extend the Ω_5 to more than three layers. A small portion of the assemblies are illustrated in Figure 4.25, as denoted by Ω_{11} and Ω_{12}, but none of them achieve positive mobility. To enable inextensional wrapping, all of the radial creases are required to be gashed through. An example of these rigid foldable models is denoted by Ω_{13} with a six-layer layout. In fact, with radial symmetry being maintained, this extension approach imparts positive mobility regardless of the number of layers. The break of the radial creases permits the facets to be stowed towards the desired compact form and the connection of the outmost nodes enables holistic movements. Despite requiring extra constraints on the folds to provide predefined folding directions, this approach is kinematically eligible to be implemented on a large solar receiver.

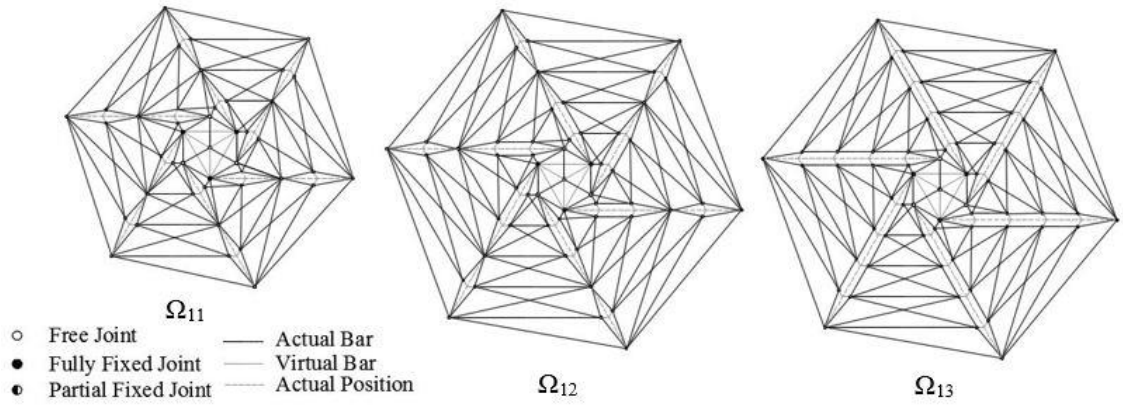

Figure 4.25 Examples of multi-layer Trimmed Crease Patterns.

4.4 Applying the rigid foldable patterns with a square hub

With the development of space technology, a miniaturized satellite named CubeSat has been proposed with advanced specification (Herner, Puig-Suari and Twiggs, 2012). As suggested by its name, this small spacecraft consists of a unit $10 \times 10 \times 10$ centimetres in volume, where square shapes are expected from its orthographic views. Since its inception, the CubeSat has gained a surge in research due to its superior practicality in space exploration, but a strictly inextensional solar soil is still yet to be discovered. In responding to this gap, the two rigid foldable patterns, Ω_2 and Ω_5, are thus modified to fit with a square hub. According to the design strategy proposed by Guest and Pellegrino (1992), as reviewed in Section 2.5.2, the modified pin-jointed frames with a four-sided hub are established and shown in Figure 4.26.

In order to achieve the desired mobility, the two diagonal hub nodes are fully fixed and the central node is allowed to move along the z-axis only. Again, the mobility of the two models is checked via the Kutzbach criterion. For Ω_{14} where $n = 33, j = 53$ and $f_i = 3$, the mobility is

$$m = 6 \times (33 - 53 - 1) + (3 \times 53 + 1) - 33 = 1. \qquad (4.48)$$

For Ω_{15} where $n = 45, j = 73$ and $f_i = 3$, there is

$$m = 6 \times (45 - 73 - 1) + (3 \times 73 + 1) - 45 = 1. \tag{4.49}$$

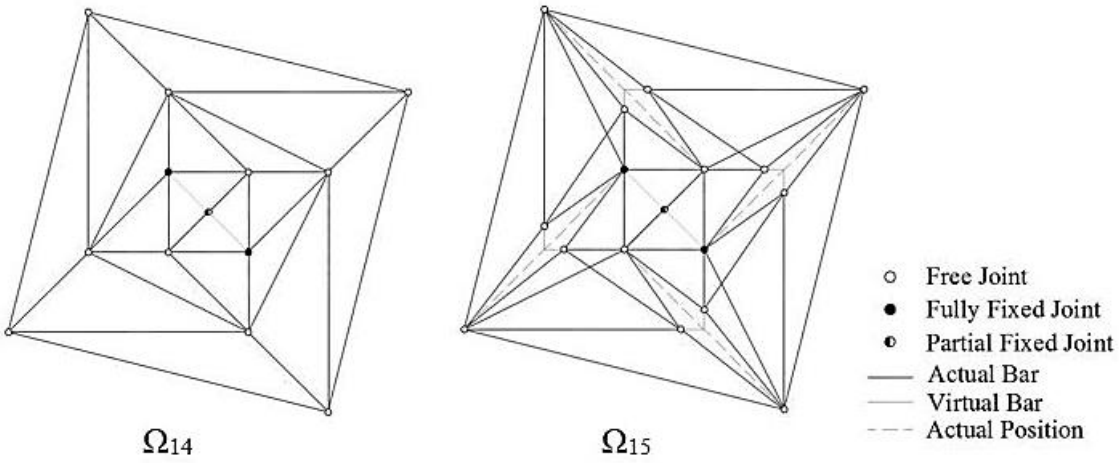

Figure 4.26 The two rigid foldable patterns are modified to fit with a square hub.

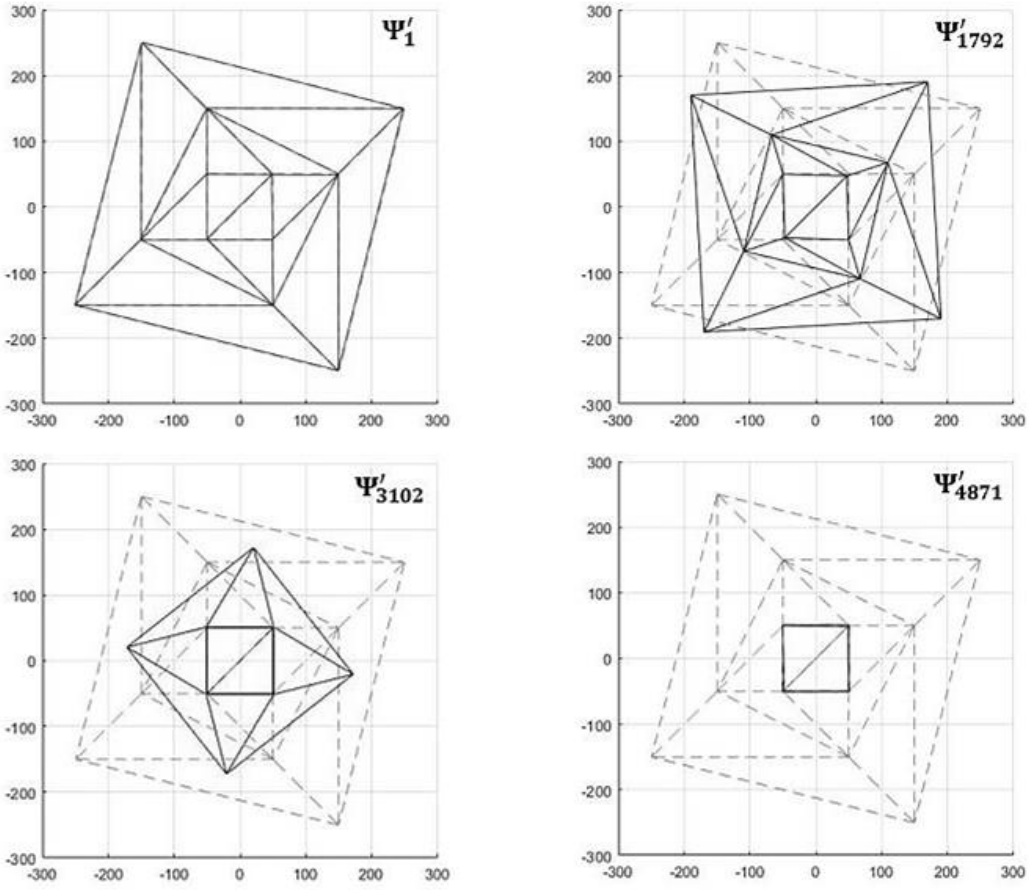

Figure 4.27 The folding Sequence of Ω_{14}.

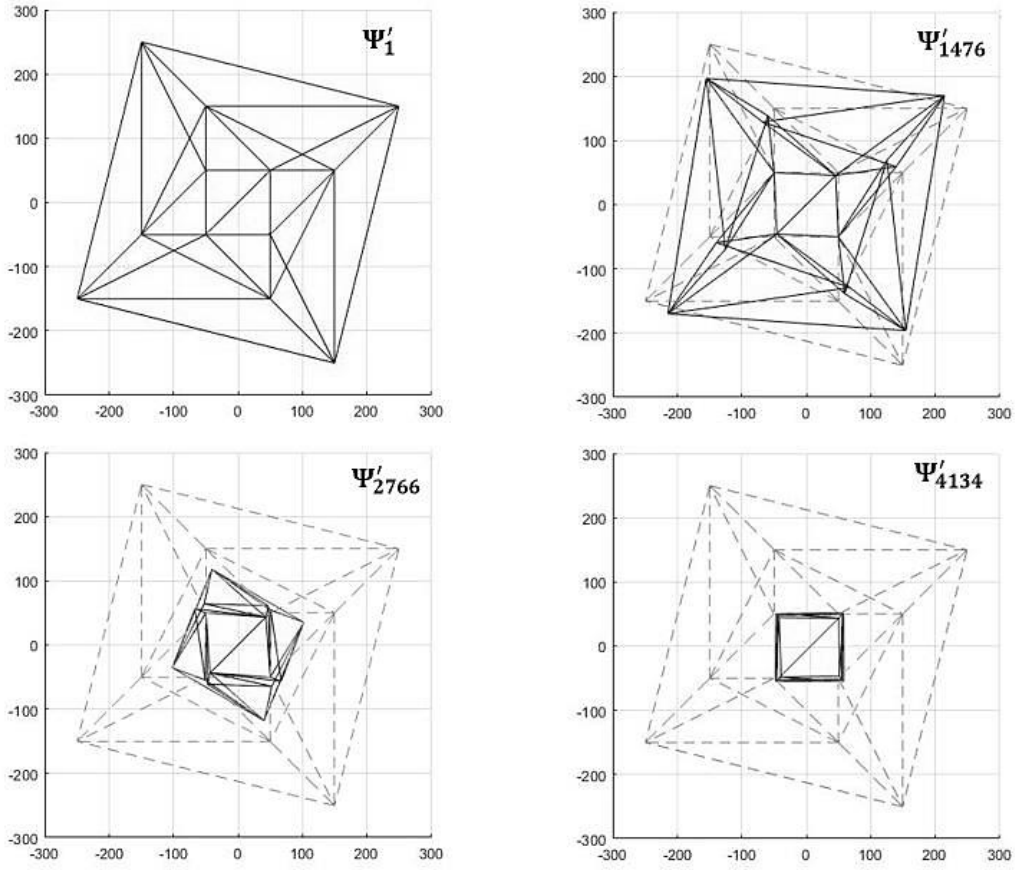

Figure 4.28 The folding Sequence of Ω_{15}.

Both models impart a single mobility, which are the optimum results for the design of deployable solar receivers. Similarly, applying the mechanical modelling method allows the models to be simulated throughout the attainable range. Carrying out the iterative predictor-corrector algorithm with the step length $\Delta_1 = 0.2$ for both configurations produces the most compact forms. The folding sequence of Ω_{14} and Ω_{15} are illustrated in Figure 4.27 and Figure 4.28, respectively. According to both figures, at the fully stowed configurations, the circumjacent layers coincide with the verge of the square hub, given the thicknesses of layers are assumed to be zero. The partial fixed central node moves vertically, actuating the hub to have out-of-plane motion. The two prototypes have diverse paths in the folding process. For Ω_{14}, the inner loop of triangular panels are stowed first, given the diagonal folds are rotated to a small degree to release the internal strain. For Ω_{15},

the adjacent units are slightly separated from the trimmed radial creases and thus the whole assembly moves synchronously. By inspection, no bar has been deformed more than the designated acceptable strain $\epsilon_{ij} = 10^{-5}$ for the entire folding process for both models. Therefore, it can be concluded that either inextensional approaches, the facets triangulation or the radial creases trim, can be applied to the wrapping patterns with the square hubs. The two patterns, Ω_{14} and Ω_{15}, are considered to be eligible for adoption for the solar receiver design of a CubeSat.

4.5 Thickness Accommodation

The previously simulated prototypes of origami stipulate zero thickness for the facets. Therefore, the stacked layers at the fully stowed configuration are mathematically coplanar at the verge of the hub. However, application to solar panel arrays will inevitably require materials with finite thickness. The original coplanar layers are therefore needed to be separated with significant spacing, which may force the original kinematics to be changed. Only a handful of layer thickening schemes have been conducted, as reviewed in Section 2.5.4, which have obvious drawbacks; the original zero-thickness idealization is required to be altered to a pattern with a less compact stowed configuration, and the model is only capable of accommodating tiny thickness. Consequently, in this section we attempt to develop a thickness accommodating model for a solar array panel that adopts any thickness.

4.5.1 Design approach

The optimum design requires the thickness to be accommodated without altering the original kinematics from its zero-thickness parent pattern. In this case, the models that are capable of wrapping inextensionally with neglected thickness are eligible with finite thickness. The thickness accommodating approach is thus selected from the techniques which are able to maintain the original motions, as reviewed in Section 2.4.

The geometry of the cylindrically winded facets produces a special configuration. In zero-thickness origami prototypes, all of the creases begin in a common plane and end in the coincident positions at the verge of the hexagonal hub. Taking the material thickness into account, the original coincident layers are isolated radially from one another. As illustrated in Figure 4.29-A, the outer panels from a wrapping unit are required to envelope the inner layers. This speciality in the structure nullifies potential adoptions of most existing thickness accommodation solutions due to self-intersections. The only exception is the offset panel technique, which thickens the idealized wrapping prototypes with the kinematic properties being kept.

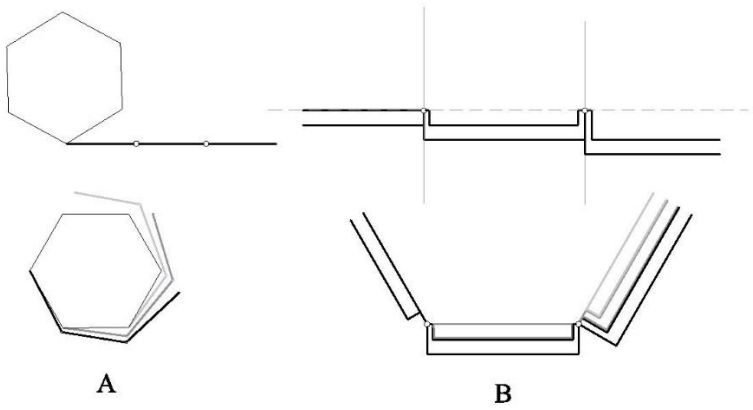

Figure 4.29 Adding thickness to the wrapping pattern in the fully flat and fully stowed state: (A) The zero-thickness pattern and (B) the offset panels designed for the wrapping pattern.

The offset panel technique requires the revolute axes to stay at the original positions to mimic the original motion. The thick panels, however, are offset a distance to create gaps for thickness accommodation. A virtual joint plane is therefore created, as denoted by the grey dashed line in Figure 4.29. Design commences from the innermost layer, where the thickened layers analogous to the paper with zero thickness can be simply attached to the joint plane. Then the panels of outer layers are stacked in a radial sequence and the offset distance is determined by the accumulated thickness. A series of rigid extensions are introduced to link the offset panels to the joint plane, and thus the panels are capable of

rotating around the virtual axes. The revolute joints of the thickened model completely coincide with the zero-thickness wrapping patterns, producing identical kinematics. The design of the thick panels is illustrated in Figure 4.30.

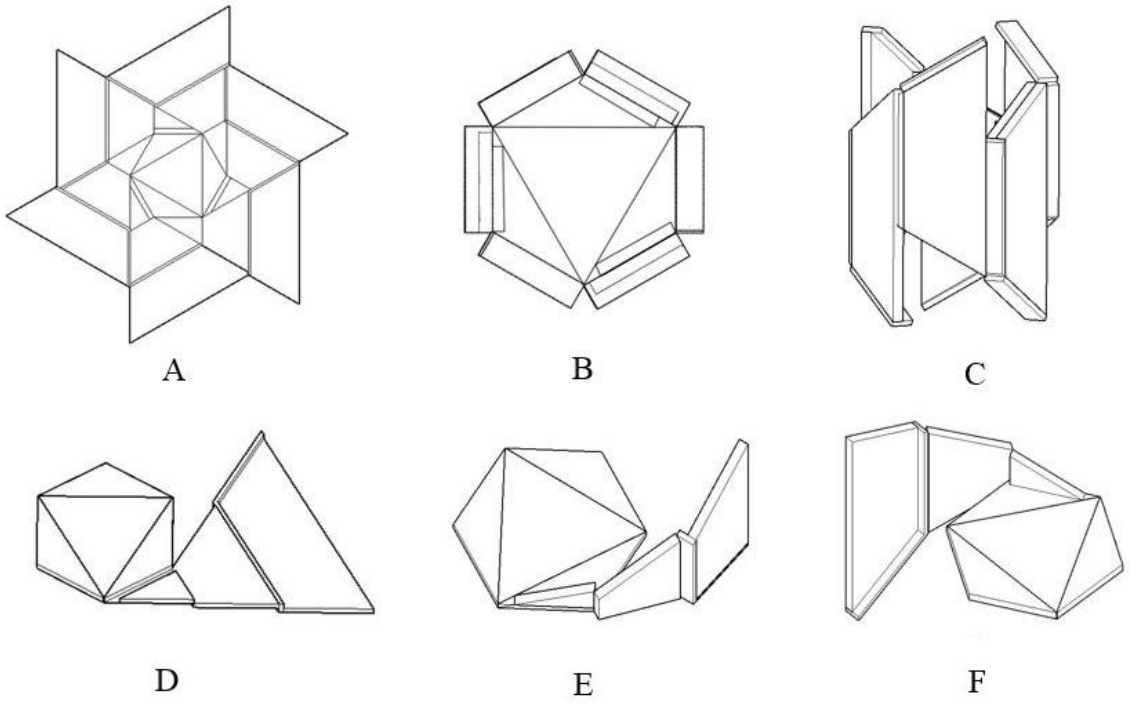

Figure 4.30 The design of the thickness-accommodating pattern with a hexagonal hub. Global design: (A) deployed form, top view; (B) stowed form, top view; (C) stowed form, side view. Local details: (D) deployed form; (E) partially stowed form, external viewpoint; (F) partially stowed form, internal view point.

There are several key points that should be noted in the design process. First, with arbitrary length of extensions, this approach applies to all inextensional wrapping models regardless of the number of layers. Despite the fact an uneven surface is expected in the fully deployed configuration, the thickened model presents a regular shape in the stowed state with rotational symmetry being preserved. Moreover, the kinematics is thickness-independent, which means the panels can be assigned with inconsistent thicknesses. To facilitate the model construction, the inner-most layer could be attached inside the virtual plane. In this case, the stacking sequence of layers could start form the second layer, which reduces the number of required extensions (Figure 4.31). Finally, in a physical implementation, the

extensions will inevitably have non-zero thickness. This means these rigid extensions have to be thickened to either side of the virtual rotational hinges, which may cause local intersections in the stowed configuration. This can be avoided by cutting grooves to allow the protruded part of the extensions to be embodied into the inner panels, and thus the self-intersections can be avoided, as shown in Figure 4.32.

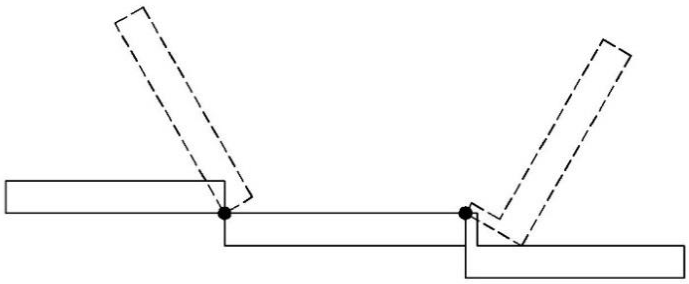

Figure 4.31 An alternative method of offset panels.

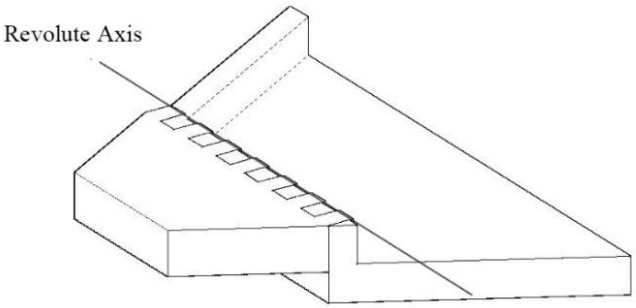

Figure 4.32 Introducing grooves to avoid self-intersections.

4.5.2 Physical model

Since the two rigid foldable patterns, Ω_2 and Ω_5, are modified from the six-sided winding membrane proposed by Guest and Pellegrino (1992), they have an identical shape in the fully deployed and folded configurations. Therefore, the same thickness-accommodating rule can be applied to both patterns.

The thickened prototype can be altered for facets with diverse thickness. Figure 4.33 illustrates a demonstrative example of a two-layer model in 4mm thick plastic fabricated

via 3D printing. A thin membrane was used as the intermediate layer to aid construction, located at the position of the virtual plane. Although the panels almost cover the entire pattern to maximize the surface area, three small gaps are reserved in the valley creases between the hub and the three surrounding triangles.

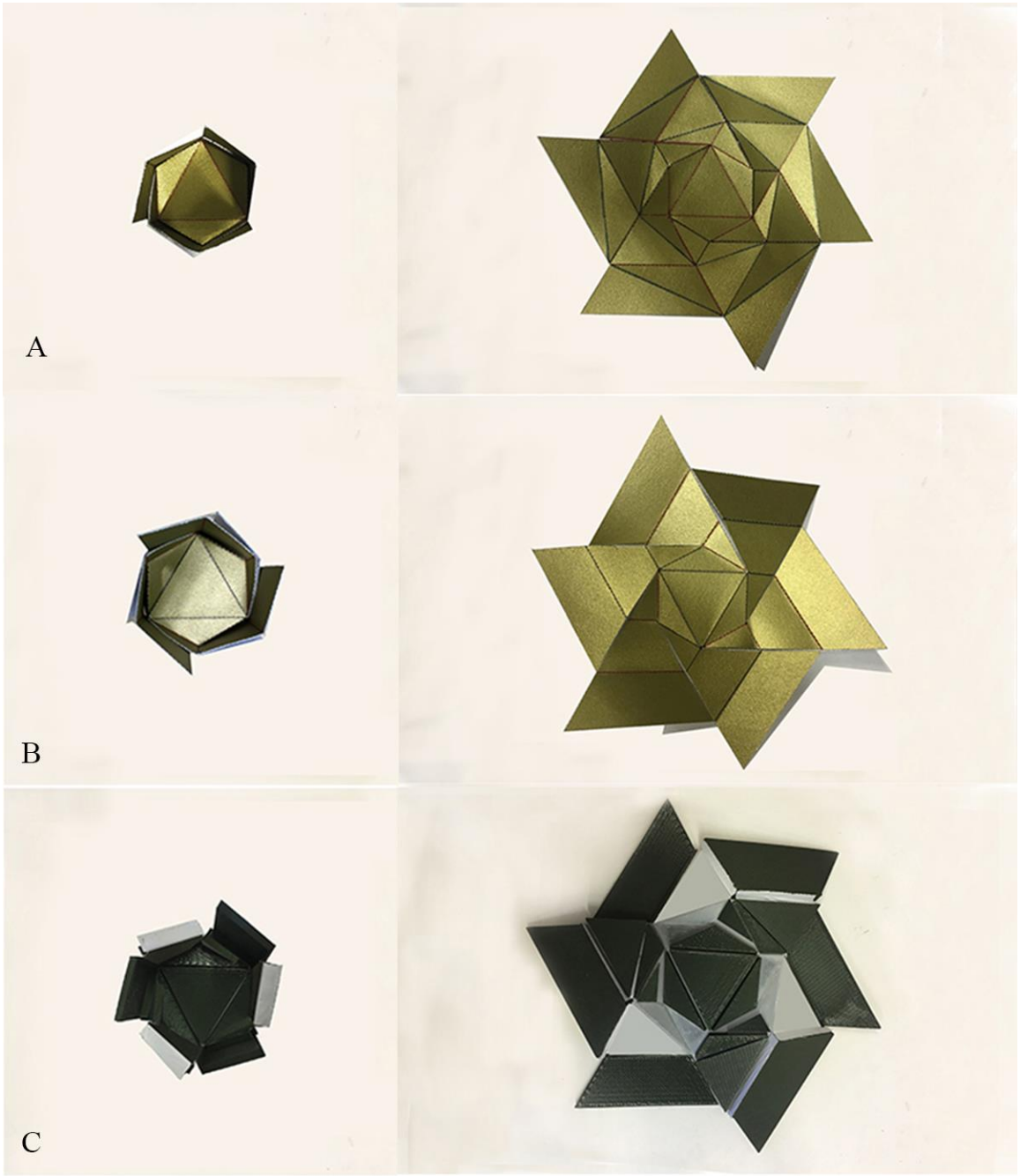

Figure 4.33 The two rigid-foldable origami source models (A) Ω_2, (A) Ω_5 and (C) their common thickened counterpart in the fully deployed and stowed configuration.

Despite it being possible to utilise this model to a number of wrapping applications, it is primarily designed to be applied in the solar panel arrays of a satellite. Figure 4.34 illustrates the model's potential implementation on a spacecraft.

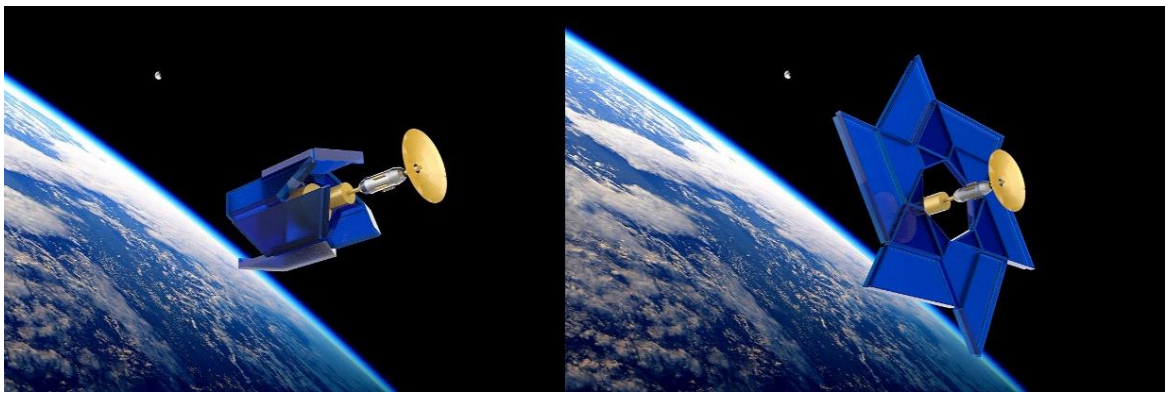

Figure 4.34 Rendering sketches of the deployment of solar panel arrays in space.

4.6 Rigid origami simulator

Interactive simulation of rigid origami plays a crucial role in modelling origami-inspired deployable structures. It provides the users with a visualised manipulation system that enables the assembly to be understood with ease. Remarkable examples of available software include 'FoldStar' and 'Origamizer', which manifest the interactive animation of folding a flat paper into a stowed state. However, none of the available software is capable of simulating rigid origami with the mechanical modelling method. In this section we present a new software system that detects the rigid foldability of a mechanism, as well as showing the animation of motion during the folding process, based on the mechanical modelling method.

As elaborated in Section 4.2.3, the mechanical modelling method represents the rigid origami with a pin-jointed framework. Subsequently, a forward kinematics is utilised with a corrector-predictor algorithm. In order to include geometric information, the algorithm requires the construction of the equilibrium matrix, which means an equilibrium equation

needs to be formulated for each non-foundation node. Since a single node may be related to a number of bars, the entries of the matrix could be very complex. Moreover, correcting bar lengths demands a linearized equation, consisting of a large number of nodal coordinates, to be formulated for every single bar. As a consequence, the matrices and equations could be huge when dealing with a slightly complicated assembly. The programming process is thus immensely time-consuming and presents great potential for making errors during the laborious work.

In light of these drawbacks, the computational algorithm has to be simplified before being developed into a user-friendly system. The simplification starts by assigning the relationship between nodes and bars via an input matrix **G**, as shown in Appendix D. Since a bar is constrained by two nodes, the sequential numbers of the two nodes are listed in pairs and put in the appropriate entries in matrix **G**. For example, if the nodes 4 and 5 are connected by the bar 7, 4 and 5 are put in the entries (7,1) and (7,2), respectively. Given the node-bar relationship is explicitly assigned, the equilibrium matrix **H** and the bar length equations can be generated automatically. It should be noted that the fully-fixed and partially fixed nodes need to be treated specially when constructing **H**. If nodal displacements along specific directions are constrained, the corresponding entries are excluded accordingly. Finally, all the required inputs are extracted to an assembly area before the algorithm. This manipulation enables all kinds of rigid origami to be simulated by simply altering the input parameters.

Next, the algorithm is implemented as a software system written in Matlab® with graphical user interface (GUI). The mobility is calculated first using the Kutzbach criterion, as guidance for designing the pin-jointed framework. The input variables, such as the initial nodal coordinates, the amplitude of the predictor steps and the number of iterations, are clearly recorded for the simulation. Lastly, the corresponding data is loaded and substituted

into the algorithm and two graphic interpretations are generated. One of them presents the trajectories of motion for each of the movable nodes, and the other exhibits an animation of the folding process. The screenshots of the interface design are shown in Figure 4.35 and the complete script are attached in Appendix D.

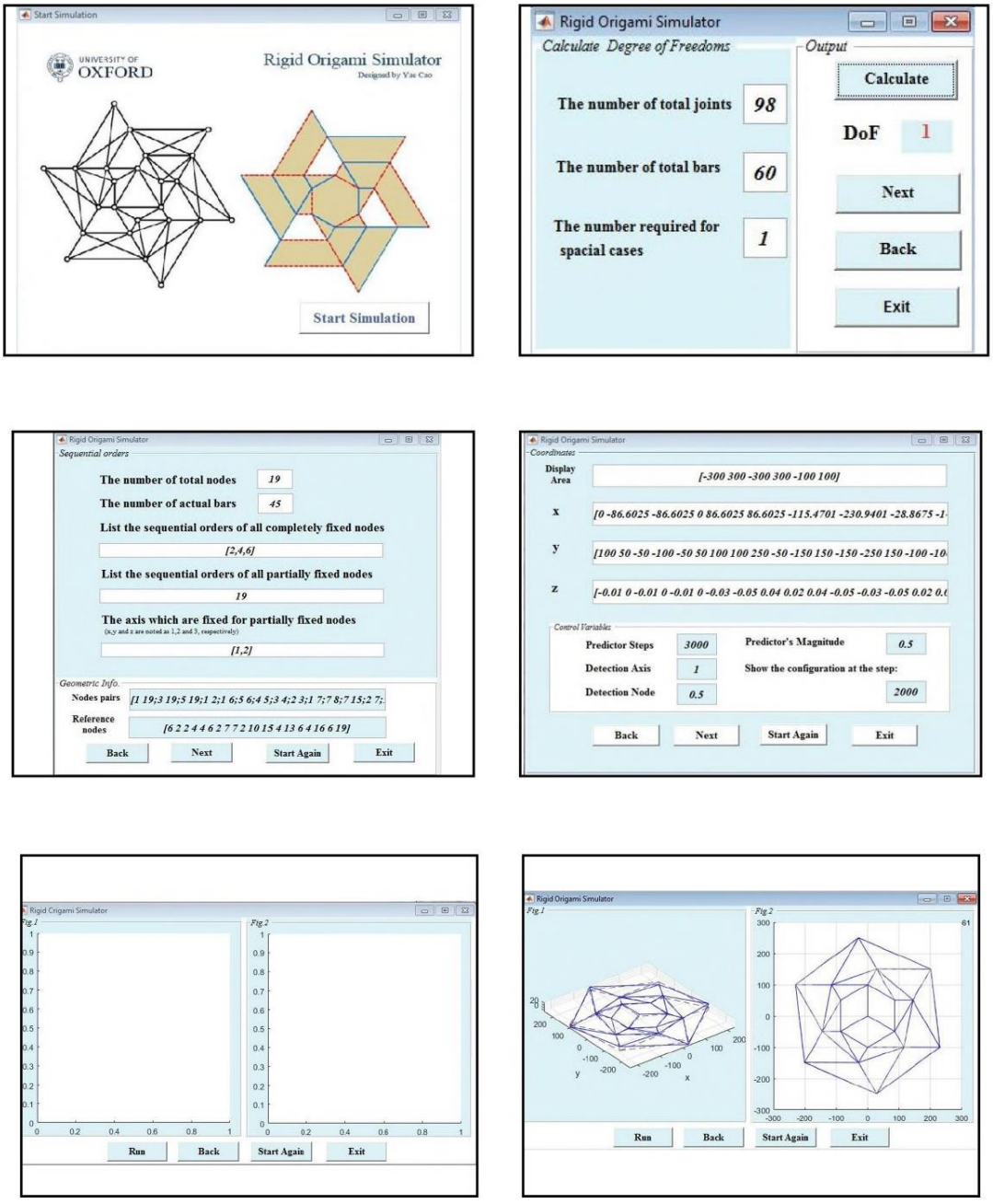

Figure 4.35 Screenshots of the interfaces in the rigid origami simulator.

This programme offers a comprehensive simulation of the motions for rigid origami patterns. The users can determine the rigid foldability and the folding path of any deployable structures with ease. Since the code of the algorithm has been enormously simplified, this system supports the simulation of highly complicated origami patterns with short computational and programming time. By adjusting the number of iteration steps, intermediate states of motion can be displayed by visualized animations. Moreover, the viewpoint of the framework can be rotated freely during the animation, which aids users to understand the analysed pattern from all directions.

Despite being capable of simulating the motion of rigid origami in a comprehensive way, the rigid origami simulator still has some drawbacks. Since the patterns are represented by bars and pins, the simulator is incapable of automatically detecting self-intersections between adjacent panels. The virtual surfaces may pass through each other without conceding the rigidity of bars, which requires extra actions to avoid local self-intersections. Besides that, the folding direction at the creases is not taken into account, which means a crease can be a mountain or valley fold. Although most patterns are unaffected, it may cause ambiguity for particular patterns where the folding direction needs to be pre-specified. Finally, the code written in Matlab® is not sufficiently robust; a proven correct code might report an error for the second run. This calls for further improvements.

4.7 Sequential square twist patterns

Instead of wrapping, an alternative method is considered to retract circumambient facets into the hub. Inspired by the rigid foldable square-twist pattern, as reviewed in section 2.3.2, I aimed to achieve a higher deployed-to-stowed ratio by repetitively twisting the central square.

To enable twisting for every sequential step, the pattern must be configured by strictly imposing rotational symmetry. The four creases around the square hub must be arranged in a two-by-two sequential form. Otherwise the global compatibility cannot be achieved. Despite composing of multiple creases, the vertices still behave as spherical 4R linkages, with the extra joints temporarily locked for subsequent motions. Therefore, the sector angles of each degree-four vertices must be partitioned following the rules of flat-foldability, as reviewed in section 2.3.1. The crease pattern of the sequential twisted square-hub model is depicted in Figure 4.36.

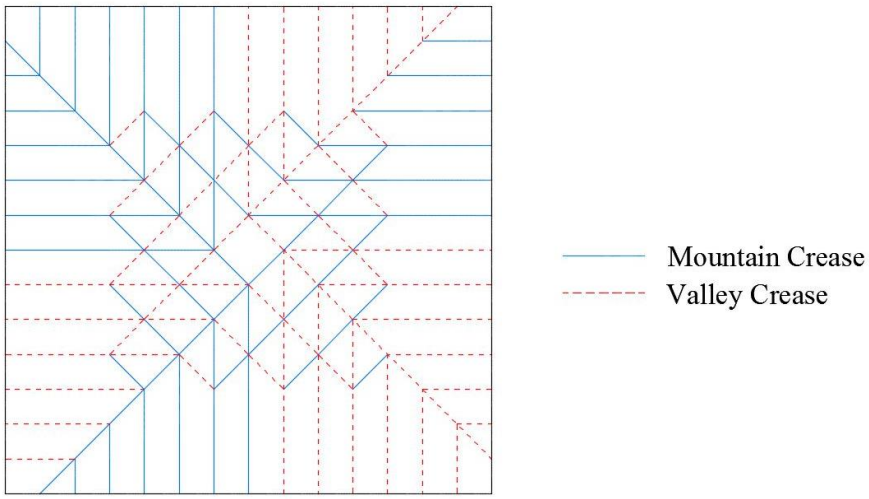

Figure 4.36 The crease arrangement of the sequential twisted pattern.

This new design allows the strips in twisting areas to be stowed sequentially and simultaneously around the central square, which is ideal for satellites with spinning deployment methods. The rotation symmetry allows each twist to fold two strips from every direction. These retracted strips are stowed under twisting areas, as shown by the shaded zones in Figure 4.37, where a darker colour implies more accumulated layers. Following each twisting step, the surface area of the pattern is gradually reduced. The deployed-to-stowed ratios from the 1st to the 4th step are 1.36, 1.97, 3.08 and 5.50, respectively. A larger ratio is expected by more twisting steps.

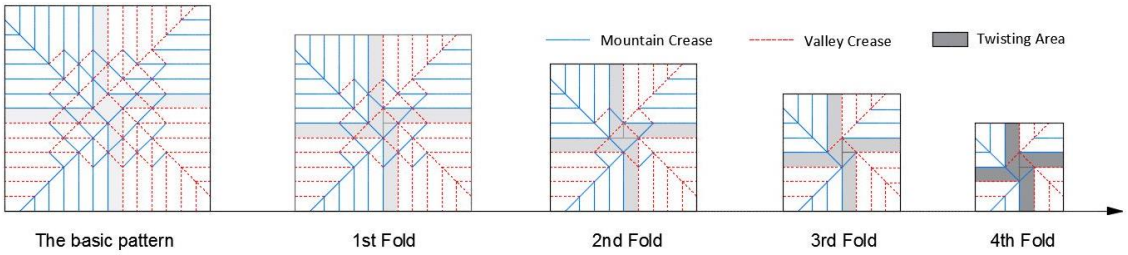

Figure 4.37 The sequential twisting process.

It should be noted that this sequential twisted design is limited to the square hub only, as it is the only known twist pattern with rigid foldability. The retracted rigid facets are extensively accumulated in twisting areas. The inner layers are enveloped by the outer layers; which denies the possibility of exerting the existing thickness-accommodating approaches. Therefore, the sequential twisted pattern is ineligible for applications made of thick materials (e.g. solar panel arrays) due to self-intersections. However, this pattern can be folded rigidly with a relatively large deployed-to-stowed ratio. This is a huge advantage over the flexible wrapping pattern proposed by Satou and Furuya (2013) as the surface accuracy of the antenna and the space power system require the surface of the sail to be undeformable. Therefore, the sequential twisting pattern is considered as an adequate prototype for a deployable membrane with infinitesimal thickness. This makes it an ideal pattern for application as the solar sail of a CubeSat, which is made of 7 μm to 12 μm Kapton films (Lappas et al., 2011). Moreover, the four-sided hub of this pattern exactly fits the square cross-section of a CubeSat, presenting great potential for application on this miniaturized satellite.

4.8 Concluding remarks

This chapter has presented the attempts to discover adequate deployable patterns for the solar receivers of satellites. An ideal pattern should be capable of stowing to a compact form before deploying to an annular disk with a large deployed-to-stowed ratio. Meanwhile,

it is supposed to be inextensional throughout the folding process, preferably with the ability to accommodate material thickness.

The chapter started with a strict validation to verify the rigid foldability of the six-sided winding membrane proposed by Guest and Pellegrino (2012). By adopting the matrix method, encircled forward paths were created, allowing the compatibility to be simply checked from loop-closure conditions. The results suggested that compatibility is only achieved in the completely flat and folded state, and the existence of a rigid transition was denied. Considerable new patterns have been designed and validated with the same approach, but none of them appropriately fulfil the requirements of solar receivers.

Albeit lacking a rigid transition, the winding membrane is still considered the most proximal pattern to achieve inextensional wrapping. Therefore two derivative prototypes, Ω_4 and Ω_5, were proposed and simulated using the mechanical modelling method. Compared to the matrix method, this approach enables the trajectories of motion to be obtained without relying on loop-closure conditions, which is more suitable for the two patterns with disconnected surfaces. The results demonstrate that although both prototypes can be stowed rigidly, only the latter achieved the desired compact shape. Therefore Ω_5, along with Ω_2, as reviewed in Section 2.5.3, are deemed as the two eligible prototypes for inextensional wrapping.

Next, these six-sided two-layer prototypes were extended to the patterns with multi-layer layouts or with square hubs. Again, numerical simulation was carried out and the results suggest the extension schemes are valid for both prototypes.

Applying the patterns to a solar panel array requires material with finite thickness to be used. However, the origami prototypes are primarily designed for paper where the thickness can be disregarded. Therefore, a thickness-accommodating scheme was

proposed based on the offset panel technique, enabling the thickened model to maintain original kinematics from its origami source pattern. This scheme can be applied for the inextensional wrapping patterns with arbitrary thickness and a number of layers, producing an elegant compact form at the fully stowed configuration.

The mechanical modelling method provides an effective and robust tool in simulating rigid origami. However, the programming process could be extremely time-consuming when dealing with slightly complicated assemblies. Therefore, a visualised operation software system has been created to provide users with rigid foldability detection, nodal trajectories display and animation of motion. This is achieved by an immensely simplified code based on the mechanical modelling method, followed by user-friendly interfaces. As a result, rigid origami can be analysed with comprehensive visualization and largely reduced computational time, by simply inputting a number of necessary variables.

Finally, instead of adopting the wrapping mechanism, an alternative deployable method was used by sequentially twisting the square hub. This pattern achieves rigid foldability with a relatively high deployed-to-stowed ratio. However, it is limited to applications with infinitesimal thickness, such as solar sails, due to its incapability in thickness accommodation.

5. Final Remarks

This dissertation has mainly focused on two origami-related issues: rigid origami with thick panels and the inextensional deployable membranes. In this chapter, the major achievements are summarised, followed by an attempt to identify necessary future work.

5.1 Major achievements

5.1.1 Rigid origami with thick panels

The first effort of this dissertation was to systematically prove that adopting the offset crease technique allows material thickness to be accommodated without altering the kinematics of the original origami. This was achieved by converting rigid origami patterns to mechanical linkages. A comprehensive kinematic algorithm for the three representative spatial linkages has been constructed. The identical geometric conditions throughout the full range of motion demonstrated that the kinematics of the said linkages precisely mimics that of their zero-thickness counterpart. Therefore, it was concluded that the original origami and the offset crease patterns possess kinematic equivalence.

An elaborated implementation strategy for adopting the offset crease technique has been proposed, with the traditional Miura-ori pattern being a demonstrative example. This strategy has provided an effective guidance on thickness accommodation and self-intersections avoidance for general origami tessellations. The feasibility of the strategy was confirmed by the successful construction of a number of thick models, with an analytical discussion of their strengths and limitations. Certain special crease patterns which are unfeasible for being thickened by the technique have been identified and analysed explicitly.

Furthermore, we have designed a novel tessellation based on the traditional Miura-ori pattern. This pattern maintains the desired properties that are possessed by its parent pattern, such as rigid foldability and a single mobility. Meanwhile, it greatly mitigates the unwanted condition in the traditional Miura-ori pattern, which has excessively stacked layers in the stowed configuration. In order to achieve a high deployed-to-stowed ratio, an optimisation approach has been quantitatively analysed, which allows the tessellation to be adjusted according to diverse requirements. Finally, we have proven that thickening this novel pattern by the existing thickness-accommodating techniques is feasible.

5.1.2 Inextensional deployable patterns

Another primary effort for this dissertation was to discover a fold pattern that can be stowed and deployed without deflecting any panels. Firstly, we have established a strict mathematical proof which denied the existence of a rigid transition from the hexagonal winding membrane. Nonetheless, having undertaken a considerable number of comparisons, we have concluded that this membrane is the most proximate pattern to achieve our goal.

Therefore, two derivative prototypes have been created and their trajectories of motions were simulated with the mechanical modelling method. This allows us to discover the ideal prototype, which can be wrapped inextensionally into a desired compact configuration. Subsequently, the desired hexagonal wrapping patterns have been extended to the one with multiple layers or a square hub and their motions were studied respectively. A thickness accommodation scheme was proposed based on the offset panel technique, allowing the wrapping pattern to be utilised for applications with arbitrarily significant thickness.

In order to provide researchers with a visualised manipulation system, we have programmed a rigid origami simulator. This software employs graphic user interfaces,

which enable an arbitrary origami-inspired assembly to be analysed based on a simplified corrector-predictor algorithm. The use of the simulator leads to greatly reduced computational time, as well as a lower likelihood of human errors occurring during the laborious coding process.

Instead of wrapping the circumambient panels around the hub, a novel retraction approach has been proposed by sequentially twisting the square hub. This approach provides an alternative mode of motion that enables thin membranes to be folded inextensionally.

5.2 Future work

This dissertation has reported preliminary results for origami-inspired deployable structures, which opens up a multitude of potential research paths.

First of all, the intrinsic property of the offset crease technique requires symmetric rotations from each pair of creases. This property was stipulated in mathematical validations by letting identical values for corresponding rotational angles. When proceeding to physical implantations, however, adequate measures to ensure this symmetric condition were actually scarce. Although employing chained gears has been proposed in this report, this approach was proven to be unfeasible for creases wider than 2φ due to the risk of local collisions for the protruding part. Therefore, it is imperative to design a locking mechanism for each pair of creases to allow this promising thickness-accommodation technique to be applied to commercial products.

Secondly, in preliminary work we have only quantitatively defined the approximate shape of the discarded area for the offset crease pattern. Future work could aim to develop a more precise calculating algorithm for determining the trimmed zone, which is preferably capable of being generalised to all types of origami tessellations.

Thirdly, the motivating driver of designing inextensionally deployable patterns is to discover a proper model for solar panels on spacecraft. We have only derived an adequate model without considering the deployment method from its stowed configuration during launch. In reality, the adoption of a particular actuation approach may require the model to be modified. Further study of the development of a suitable deployment method is needed, with the features of both solar panels and the satellite being taken into consideration.

Fourthly, the strict rotational symmetric configurations of the inextensional wrapping patterns result in kinematic bifurcation points. The way it manifests itself in a mathematics context, is the existence a number of linear dependent equations due to the equality of bar lengths. Therefore, at each bifurcated configuration, more than one kinematic paths arise, which may cause faults during the motion. This problem could be solved by intentionally introducing imperfections in the assembly. That is to say, a slight variation in bar length can avoid the pattern to enter into an incorrect path. Although the physical implementations will inevitably produce imperfections due to manufacturing imprecisions, it would be more controllable to design the imperfections into the assembly. Therefore, a systematic analysis of such design is imperative to avoid abnormal motions at bifurcation points.

Furthermore, for the rigid origami simulator, we have only designed the fundamental functions based on a simplified Matlab® code, where the animation of motion from a pin-jointed frame is displayed. Ideally, the origami simulator should be able to present an interactive interface of a paper model that allows users to control the motion by simply dragging or rotating a panel. Also, the collisions between panels are supposed to be detected automatically. The folding direction for each crease should be predefined to avoid potential ambiguity for certain patterns. Furthermore, the construction of the model could be completed by importing from 3D modelling software, where the nodal coordinates can

be read automatically. In pursuit of an improved simulator, it might be helpful to use other programming languages to create a more sophisticated script.

Last but not the least, in this dissertation we have only considered the sequentially twisting pattern with a square hub, as it is the only known inextensional twisting pattern. Further effort could be made on extending the crease assignment principals to origami patterns with non-square hubs, with the rigid-foldability being preserved.

References

Baker, J. and Min, H. (1986). On spatial networks of overconstrained linkages. *Mechanism and Machine Theory*, 21(5), pp.427-437.

Cambridge Consulants, (1989). "*Design study for a Mars spacecraft*", Technical report.

Chen, Y., Peng, R. and You, Z. (2015). Origami of thick panels. *Science*, 349(6246), pp.396-400.

Denavit, J. and Hartenberg, R. (1965). A kinematic notation for lower-pair mechanisms based on matrices. *Journal of Applied Mechanics*, vol.77, pp. 215-221, June 1955.

De Temmerman, I., Mollaert, M., Van Mele, T. and De Laet, L. (2007). Design and Analysis of a Foldable Mobile Shelter System. *International Journal of Space Structures*, 22(3), pp.161-168.

Duerig, T. and Wholey, M. (2002). A comparison of balloon- and self-expanding stents. *Minimally Invasive Therapy & Allied Technologies*, 11(4), pp.173-178.

Edmondson, B., Lang, R., Magleby, S. and Howell, L. (2014). An offset panel technique for rigidly foldable origami. *In Proceedings of ASME IDET/CIE 2014*.

Edmondson, B., (2015). Development of a Thickness Accommodation Technique for Origami-Inspired Design. *BYU Scholars Archive All Theses and Dissertations.* Paper 5294

Evans, T., Lang, R., Magleby, S. and Howell, L. (2015). Rigidly foldable origami gadgets and tessellations. *R. Soc. Open Sci.*, 2(9), p.150067.

Felton, S., Tolley, M., Demaine, E., Rus, D. and Wood, R. (2014). A method for building self-folding machines. *Science*, 345(6197), pp.644-646.

Greenberg, H., Gong, M., Magleby, S. and Howell, L. (2011). Identifying links between origami and compliant mechanisms. *Mechanical Sciences*, 2(2), pp.217-225

Guest, S. D., & Pellegrino, S. (1992). Inextensional wrapping of flat membranes. First International Seminar on Structural Morphology, LMGC, Universite Montpellier−II, Montpellier, 203-215.

Herner, R., Puig-Suari, J. and Twiggs, R. (2012). An Advanced Standard for CubeSats. Proceedings of the AIAA/USU Conference on Small Satellites, SSC12-XII-1.

Hoberman, C. (2010). *Folding structures made of thick hinged sheets*. US patent 7794019.

Huffman, (1976). Curvature and Creases: A Primer on Paper. *IEEE Transactions on Computers*, C-25(10), pp.1010-1019.

Hull, T. (1994). On the mathematics of flat origamis. *Congressus Numerantium*, 100, pp.215-224.

Hull, T. (2003). Counting Mountain-Valley Assignments for Flat Folds. *Ars Combinatoria*, pp.175-178.

Hunt, K. (1978). *Kinematic geometry of mechanisms*. Oxford: Clarendon Press.

Huso, M. (1960). Sheet reel. US patent 2942794 A.

Hutchinson, R. and Fleck, N. (2006). The structural performance of the periodic truss. Journal of the Mechanics and Physics of Solids, 54(4), pp.756-782.

Johnson, W. and Yu, T. (1980). The angle of fold and the plastic work done in the folding of developable flat sheets of metal. *ARCHIVE: Journal of Mechanical Engineering Science 1959-1982 (vols 1-23)*, 22(5), pp.233-241.

Ku, J. and Demaine, E. (2016). Folding Flat Crease Patterns With Thick Materials. *J. Mechanisms Robotics*, 8(3), p.031003.

Kumar, P. and Pellegrino, S. (2000). Computation of kinematic paths and bifurcation points. *International Journal of Solids and Structures*, 37(46-47), pp.7003-7027.

Lang, R. (2003). Origami design secrets. *1st ed. Natick*, MA: A.K. Peters, pp.51-70.

Lappas, V., Adeli, N., Visagie, L., Fernandez, J., Theodorou, T., Steyn, W. and Perren, M. (2011). CubeSail: A low cost CubeSat based solar sail demonstration mission. *Advances in Space Research*, 48(11), pp.1890-1901.

Mavroidis, C. and Roth, B. (1995). Analysis of Overconstrained Mechanisms. *Journal of Mechanical Design*, 117(1), p.69.

Merchan, C. (1987). *Deployable Structures*. Master of Science thesis in Architecture Studies. Massachusetts Institute of Technology.

Miura, K. (1980). Method of packaging and deployment of large membrane in space. *31st Cong. of Int. Astronautical Federation*, (Paper A 31), pp.1-10.

Miura, K. (1989a). A note on intrinsic geometry of origami. *Research of Pattern Formation*, edited by R. Takaki, pp.91-101. Tokyo: KTK Scientific Publishers.

Miura, K. (1989b). Map fold a la Miura style, its physical characteristics and application to space science. *Research of Pattern Formation*, edited by R. Takaki, pp.77-90. Tokyo: KTK Scientific Publishers.

Pellegrino, S. and Calladine, C. (1986). Matrix analysis of statically and kinematically indeterminate frameworks. *International Journal of Solids and Structures*, 22(4), pp.409-428.

Pellegrino, S. and Guest, S. (1992). Inextensional wrapping of flat membranes. *In R. Motro, T. Wester (eds) Proc. First International Seminar on Structural Morphology, LMGC, Universite Montpellier*, pp.203-215.

Ruth, D. and McCarthy, J. (1999). The design of spherical 4R linkages for four specified orientations. *Mechanism and Machine Theory*, 34(5), pp.677-692.

Sareh, P. and Guest, S. (2015). A Framework for the Symmetric Generalisation of the Miura-ori. *International Journal of Space Structures*, 30(2), pp.141-152.

Satou, Y., & Furuya, H. (2006). Fold Line Based on Mechanical Properties of Crease in Wrapping Fold Membrane. Aiaa/asme/asce/ahs/asc Structures, Structural Dynamics, and Materials Conference (Vol.2, pp.233-240).

Scheel, H. (1974). *Space-saving storage of flexible sheets*. 3848821.

Schenk, M. and Guest, D. (2011). *Folded Shell Structures*. Doctor of Philosophy thesis. *University* of Cambridge.

Silverberg, J., Na, J., Evans, A., Liu, B., Hull, T., Santangelo, C., Lang, R., Hayward, R. and Cohen, I. (2015). Corrigendum: Origami structures with a critical transition to bistability arising from hidden degrees of freedom. *Nature Materials*, 14(5), pp.389-393.

Sternberg, S. (2010). Symmetry issues in collapsible origami. *Symmetry: Sci.*, 21(4), pp.345-364.

Tachi, T. (2011). Rigid foldable thick origami. *Origami 5: Fifth International Meeting of Origami Science, Mathematics and Education*, pp.253-264.

Wu, W. and You, Z. (2010). Modelling rigid origami with quaternions and dual quaternions. *Proceedings of the Royal Society A: Mathematical, Physical and Engineering Sciences*, 466(2119), pp.2155-2174.

Yoshimura Y. (1955). On the mechanism of buckling of a circular cylindrical shell under axial compression, NACA TM 1390. National Advisory Committee for Aeronautics.

You, Z. and Chen, Y. (2012). *Motion structures*. London: Spon Press.

Zirbel, S., Lang, R., Thomson, M., Sigel, D., Walkemeyer, P., Trease, B., Magleby, S. and Howell, L. (2013). Accommodating Thickness in Origami-Based Deployable Arrays 1. *Journal of Mechanical Design*, 135(11), p.111005.

Appendix A

Completed elements of Eq. 3.7 for the spatial 8R linkage.

(1.1) $\cos(2\theta_1)\cos(2\theta_3) - \cos\alpha_{23}\sin(2\theta_1)\sin(2\theta_3) = \cos(2\theta_5)\cos(2\theta_7) + \cos\alpha_{23}\sin(2\theta_5)\sin(2\theta_7)$

(2.1) $\cos(2\theta_3)\sin(2\theta_1) + \cos\alpha_{23}\cos(2\theta_1)\sin(2\theta_3) = -\cos\alpha_{23}\cos\alpha_{45}\cos(2\theta_7)\sin(2\theta_5) + \sin\alpha_{23}\sin\alpha_{45}\sin(2\theta_5) + \cos\alpha_{45}\cos(2\theta_5)\sin(2\theta_7)$

(3.1) $\sin\alpha_{23}\sin(2\theta_3) = -\cos\alpha_{45}\sin\alpha_{23}\sin(2\theta_5) - \cos\alpha_{23}\cos(2\theta_7)\sin\alpha_{45}\sin(2\theta_5) + \cos(2\theta_5)\sin\alpha_{45}\sin(2\theta_7)$

(4.1) $0 = 0$

(1.2) $-\cos\alpha_{23}\cos\alpha_{45}\cos(2\theta_3)\sin(2\theta_1) + \sin\alpha_{23}\sin\alpha_{45}\sin(2\theta_1) - \cos\alpha_{45}\cos(2\theta_1)\sin(2\theta_3) = \cos(2\theta_7)\sin(2\theta_5) - \cos\alpha_{23}\cos(2\theta_5)\sin(2\theta_7)$

(2.2) $\cos\alpha_{23}\cos\alpha_{45}\cos(2\theta_1)\cos(2\theta_3) - \cos(2\theta_1)\sin\alpha_{23}\sin\alpha_{45} - \cos\alpha_{45}\sin(2\theta_1)\sin(2\theta_3) = \cos\alpha_{23}\cos\alpha_{45}\cos(2\theta_5)\cos(2\theta_7) - c\cos(2\theta_5)\sin\alpha_{23}\sin\alpha_{45} + \cos\alpha_{45}\sin(2\theta_5)\sin(2\theta_7)$

(3.2) $\cos\alpha_{45}\cos(2\theta_3)\sin\alpha_{23} + \cos\alpha_{23}\sin\alpha_{45} = \cos\alpha_{45}\cos(2\theta_5)\sin\alpha_{23} + \cos\alpha_{23}\cos(2\theta_5)\cos(2\theta_7)\sin\alpha_{45} + \sin\alpha_{45}\sin(2\theta_5)\sin(2\theta_7)$

(4.2) $0 = 0$

(1.3) $\cos\alpha_{45}\sin\alpha_{23}\sin(2\theta_1) + \cos\alpha_{23}\cos(2\theta_3)\sin\alpha_{45}\sin(2\theta_1) + \cos(2\theta_1)\sin\alpha_{45}\sin(2\theta_3) = \sin\alpha_{23}\sin(2\theta_7)$

(2.3) $-\cos\alpha_{45}\cos(2\theta_1)\sin\alpha_{23} - \cos\alpha_{23}\cos(2\theta_1)\cos(2\theta_3)\sin\alpha_{45} + \sin\alpha_{45}\sin(2\theta_1)\sin(2\theta_3) = -\cos\alpha_{45}\cos(2\theta_7)\sin\alpha_{23} - \cos\alpha_{23}\sin\alpha_{45}$

(3.3) $\cos\alpha_{23}\cos\alpha_{45} - \cos(2\theta_3)\sin\alpha_{23}\sin\alpha_{45} = \cos\alpha_{23}\cos\alpha_{45} - c\cos(2\theta_7)\sin\alpha_{23}\sin\alpha_{45}$

(4.3) $0 = 0$

(1.4) $\cos\theta_1 a_{12} + \cos(2\theta_1)\cos\theta_3 a_{34} - \cos\alpha_{23}\sin(2\theta_1)\sin\theta_3 a_{34} = -\cos\theta_5\cos(2\theta_7)a_{56} - \cos\alpha_{23}\sin\theta_5\sin(2\theta_7)a_{56} - \cos\theta_7 a_{78}$

(2.4) $\sin\theta_1 a_{12} + \cos\theta_3\sin(2\theta_1)a_{34} + \cos\alpha_{23}\cos(2\theta_1)\sin\theta_3 a_{34} = \cos\alpha_{23}\cos\alpha_{23}\cos(2\theta_7)\sin\theta_5 a_{56} - \sin\alpha_{23}\sin\alpha_{45}\sin\theta_5 a_{56} - \cos\alpha_{45}\cos\theta_5\sin(2\theta_7)a_{56} - \cos\alpha_{45}\sin\theta_7 a_{78}$

(3.4) $\sin\alpha_{23}\sin\theta_3 a_{34} = \cos\alpha_{45}\sin\alpha_{23}\sin\theta_5 a_{56} + \cos\alpha_{23}\cos(2\theta_7)\sin\alpha_{45}\sin\theta_5 a_{56} - \cos\theta_5\sin\alpha_{45}\sin(2\theta_7)a_{56} - \sin\alpha_{45}\sin\theta_7 a_{78}$

(4.4) $1 = 1$

Appendix B

Completed elements of Eq. 3.43 for the spatial 10R linkage.

(1.1) $\cos(2\theta_5)(\cos(2\theta_1)\cos(2\theta_3) - \cos\alpha_{23}\sin(2\theta_1)\sin(2\theta_3)) + \sin\alpha_{23}\sin(2\theta_1)\sin(2\theta_5) = \cos(2\theta_3)\cos(2\theta_5)$

(2.1) $\cos(2\theta_5)(\sin(2\theta_1)\cos(2\theta_3) + \cos\alpha_{23}\cos(2\theta_1)\sin(2\theta_3)) - \sin\alpha_{23}\cos(2\theta_1)\sin(2\theta_5) = -\cos\alpha_{23}\sin(2\theta_3)\cos(2\theta_5) + \sin\alpha_{23}\sin(2\theta_5)$

(3.1) $\cos\alpha_{23}\sin(2\theta_5) + \sin\alpha_{23}\cos(2\theta_5)\sin(2\theta_3) = \cos\alpha_{23}\sin(2\theta_5) + \sin\alpha_{23}\cos(2\theta_5)\sin(2\theta_3)$

(4.1) $0 = 0$

(1.2) $\sin(2\alpha_{23})\cos(2\theta_1)\sin(2\theta_3) + \sin(2\alpha_{23})\cos\alpha_{23}\cos(2\theta_3)\sin(2\theta_1) + \cos(2\alpha_{23})\sin(2\theta_5)\cos(2\theta_1)\cos(2\theta_3) - \cos(2\alpha_{12})\sin(2\theta_5)\cos\alpha_{23}\sin(2\theta_1)\sin(2\theta_3) - \cos(2\alpha_{23})\sin\alpha_{23}\cos(2\theta_5)\sin(2\theta_1) = \cos(2\theta_3)\sin(2\theta_5)$

(2.2) $\sin(2\alpha_{23})\sin(2\theta_1)\sin(2\theta_3) - \sin(2\alpha_{23})\cos\alpha_{23}\cos(2\theta_1)\cos(2\theta_3) + \cos(2\alpha_{23})\sin(2\theta_5)(\cos(2\theta_3)\sin(2\theta_1) + \cos\alpha_{23}\cos(2\theta_1)\sin(2\theta_3)) + \cos(2\alpha_{23})\sin\alpha_{23}\cos(2\theta_1)\cos(2\theta_5) = -\cos\alpha_{23}\sin(2\theta_3)\sin(2\theta_5) - \sin\alpha_{23}\cos(2\theta_5)$

(3.2) $\cos(2\alpha_{23})\sin\alpha_{23}\sin(2\theta_3)\sin(2\theta_5) - \sin(2\alpha_{23})\sin\alpha_{23}\cos(2\theta_3) - \cos(2\alpha_{23})\cos\alpha_{23}\cos(2\theta_5) = \sin\alpha_{23}\sin(2\theta_3)\sin(2\theta_5) - \cos\alpha_{23}\cos(2\theta_5)$

(4.2) $0 = 0$

(1.3) $\sin(2\alpha_{23})\sin(2\theta_5)\cos(2\theta_1)\cos(2\theta_3) - \sin(2\alpha_{23})\sin(2\theta_5)\cos\alpha_{23}\sin(2\theta_1)\sin(2\theta_3) - \cos(2\alpha_{23})\cos(2\theta_1)\sin(2\theta_3) - \cos(2\alpha_{23})\cos\alpha_{23}\cos(2\theta_3)\sin(2\theta_1) - \sin(2\alpha_{23})\sin\alpha_{23}\cos(2\theta_5)\sin(2\theta_1) = \sin(2\theta_3)$

(2.3) $\sin(2\alpha_{23})\sin(2\theta_5)(\sin(2\theta_1)\cos(2\theta_3) + \cos\alpha_{23}\cos(2\theta_1)\sin(2\theta_3)) - \cos(2\alpha_{23})(\sin(2\theta_3)\sin(2\theta_1) - \cos\alpha_{23}\cos(2\theta_1)\cos(2\theta_3)) + \sin(2\alpha_{23})\sin\alpha_{23}\cos(2\theta_1)\cos(2\theta_5) = \cos\alpha_{23}\cos(2\theta_3)$

(3.3) $\cos(2\alpha_{23})\sin\alpha_{23}\cos(2\theta_3) - \sin(2\alpha_{23})\cos\alpha_{23}\cos(2\theta_5) + \sin(2\alpha_{23})\sin\alpha_{23}\sin(2\theta_3)\sin(2\theta_5) = -\sin\alpha_{23}\cos(2\theta_3)$

(3.4) $0 = 0$

(1.4) $a_{45}\cos\theta_5(\cos(2\theta_1)\cos(2\theta_3) - \cos\alpha_{23}\sin(2\theta_1)\sin(2\theta_3)) + a_{45}\sin\theta_5\sin\alpha_{23}\sin(2\theta_1) + a_{34}\cos\theta_3\cos(2\theta_1) - a_{34}\sin\theta_3\sin(2\theta_1)\cos\alpha_{23} + a_{12}\cos\theta_1 = -a_{78}\cos\theta_5\cos(2\theta_3) - a_{9,10}\cos\theta_3$

(2.4) $a_{45}\cos\theta_5(\sin(2\theta_1)\cos(2\theta_3) + \cos\alpha_{23}\cos(2\theta_1)\sin(2\theta_3)) - a_{45}\sin\theta_5\sin\alpha_{23}\cos(2\theta_1) + \sin\theta_1 a_{12} + \cos\theta_3\sin(2\theta_1)a_{34} + \cos\alpha_{23}\cos(2\theta_1)\sin\theta_3 a_{34} = a_{78}\cos\theta_5\sin(2\theta_3) + a_{9,10}\cos\alpha_{23}\sin\theta_3 - a_{78}\sin\alpha_{23}\sin\theta_5$

(3.4) $a_{45}\cos\theta_5\sin\alpha_{23}\sin(2\theta_3) + a_{45}\sin\theta_5\cos\alpha_{23} + a_{34}\sin\theta_3\sin\alpha_{23} = -a_{78}\cos\theta_5\sin(2\theta_3) - a_{9,10}\sin\alpha_{23}\sin\theta_3 - a_{78}\cos\alpha_{23}\sin\theta_5$

(4.4) $1 = 1$

Appendix C

Completed elements of Eq. 3.63 for the spatial 12R linkage, left hand side.

(1.1) $\sin(2\theta_3)(\cos(2\alpha_{23})\cos(2\theta_1)\sin(2\theta_3) + \sin(2\theta_1)\sin(2\alpha_{23})\sin\alpha_{23} + \sin(2\theta_1)\cos(2\theta_3)\cos(2\alpha_{23})\cos\alpha_{23}) + \cos(2\theta_3)(\cos(2\theta_1)\cos(2\theta_3) - \cos\alpha_{23}\sin(2\theta_3)\sin(2\theta_1))$

(2.1) $-\sin(2\theta_3)(\sin(2\alpha_{23})\sin\alpha_{23}\cos(2\theta_1) + \cos(2\alpha_{23})\cos(2\theta_1)\cos(2\theta_3)\cos\alpha_{23} - \cos(2\alpha_{23})\sin(2\theta_1)\sin(2\theta_3)) + \cos^2(2\theta_3)\sin(2\theta_1) + \cos(2\theta_1)\cos^2(2\theta_3)\cos\alpha_{23}$

(3.1) $-2\sin\alpha_{23}\sin(2\theta_3)(2\sin^2\theta_3\sin^2\alpha_{23} - 1)$

(4.1) 0

(1.2) $-\cos^2\alpha_{23}\sin(2\theta_1)(\cos^2(2\theta_3) - 1) + \cos(2\alpha_{23})\sin(2\theta_1)(\cos^2\alpha_{23} - 1) + 2\cos^3\alpha_{23}\cos(2\theta_1)\cos(2\theta_3)\sin(2\theta_3) - 2\cos(2\theta_1)\sin(2\theta_3)\cos\alpha_{23}(\cos^2\alpha_{23} - 1) - 2\cos\alpha_{23}\cos(2\theta_1)\cos(2\theta_3)\sin(2\theta_3) + \sin(2\theta_1)\cos^2(2\theta_3)\cos^2\alpha_{23}\cos(2\alpha_{23}) - 4\cos^2\alpha_{23}(\cos^2\alpha_{23} - 1)\cos(2\theta_3)\sin(2\theta_1)$

(2.2) $-\cos(2\alpha_{23})(\cos^2\alpha_{23} - 1)\cos(2\theta_1) + \cos^2\alpha_{23}\cos(2\theta_1)(\cos^2(2\theta_3) - 1) + 2\cos^3\alpha_{23}\cos(2\theta_3)\sin(2\theta_1)\sin(2\theta_3) - 2\cos\alpha_{23}\sin(2\theta_1)\sin(2\theta_3)(\cos^2\alpha_{23} - 1) - \cos(2\alpha_{23})\cos^2\alpha_{23}\cos(2\theta_1)\cos(2\theta_3) + 4\cos^2\alpha_{23}(\cos^2\alpha_{23} - 1)\cos(2\theta_1)\cos(2\theta_3) - 2\cos\alpha_{23}\cos(2\theta_3)\sin(2\theta_1)\sin(2\theta_3)$

(3.2) $2\cos\alpha_{23}\sin\alpha_{23}(\cos^2(2\theta_3) - 1)(\cos(2\theta_3) + \cos^2\alpha_{23} - \cos^2\alpha_{23}\cos(2\theta_3))$

(4.2) 0

(1.3) $2\sin\alpha_{23}(\cos^2\alpha_{23} + \cos(2\theta_3) - \cos^2\alpha_{23}\cos(2\theta_3))(-\cos\alpha_{23}\sin(2\theta_1) + \cos(2\theta_1)\sin(2\theta_3) + \cos\alpha_{23}\cos(2\theta_3)\sin(2\theta_1))$

(2.3) $2\sin\alpha_{23}(\cos^2\alpha_{23} + \cos(2\theta_3) - \cos^2\alpha_{23}\cos(2\theta_3))(\cos\alpha_{23}\cos(2\theta_1) + \sin(2\theta_1)\sin(2\theta_3) - \cos\alpha_{23}\cos(2\theta_3)\cos(2\theta_1))$

(3.3) $8\sin^2\alpha_{23}\sin^2\theta_3 - 8\sin^2\theta_3\sin^4\alpha_{23} + 2\sin^4\alpha_{23}\sin^2(2\theta_3) - 1$

(4.3) 0

(1.4) $a_{45}\cos\theta_3(\cos(2\theta_1)\cos(2\theta_3) - \cos\alpha_{23}\sin(2\theta_1)\sin(2\theta_3)) + a_{45}\sin\theta_3(\sin\alpha_{23}\sin(2\alpha_{23})\sin(2\theta_1) + \cos\alpha_{23}\cos(2\theta_1)\cos(2\theta_3) + \cos\alpha_{23}\cos(2\alpha_{23})\sin(2\theta_1)\cos(2\theta_3)) + a_{34}\cos\theta_3\cos(2\theta_1) + a_{34}\sin\theta_3\sin(2\theta_1)\cos\alpha_{23} + a_{12}\cos\theta_1$

(2.4) $a_{45}\cos\theta_3(\sin(2\theta_1)\cos(2\theta_3) + \cos\alpha_{23}\cos(2\theta_1)\sin(2\theta_3)) - a_{45}\sin\theta_3(\cos\alpha_{23}\cos(2\alpha_{23})\cos(2\theta_1)\cos(2\theta_3) + \cos(2\alpha_{23})\sin(2\theta_1)\cos(2\theta_3) + \sin\alpha_{23}\sin(2\alpha_{23})\cos(2\theta_1)) + \sin\theta_1 a_{12} + \cos\theta_3\sin(2\theta_1)a_{34} + \cos(2\alpha_{23})\cos(2\theta_1)\sin\theta_3 a_{34}$

(3.4) $a_{45}\cos\theta_3\sin\alpha_{23}\sin(2\theta_3) + a_{45}\sin\theta_3(\cos\alpha_{23}\sin(2\alpha_{23}) + \cos(2\alpha_{23})\sin\alpha_{23}\cos(2\theta_3)) + a_{34}\sin\theta_3\sin\alpha_{23}$

(4.4) 1

Completed elements of Eq. 3.63 for the spatial 12R linkage, right hand side.

(1.1) $\sin(2\alpha_{23})\sin\alpha_{23}\sin(2\theta_1)\sin(2\theta_3) + \cos(2\theta_1)\cos^2(2\theta_3) + \cos(2\theta_1)\cos(2\alpha_{23})\sin^2(2\theta_3) + 2\cos\alpha_{23}\cos(2\theta_3)\sin(2\theta_1)\sin(2\theta_3)\sin\alpha_{23}$

(2.1) $\sin(2\alpha_{23})\sin\alpha_{23}\cos(2\theta_1)\sin(2\theta_3) + \cos^2\alpha_{23}\sin(2\theta_1)\sin^2(2\theta_3) - \sin(2\theta_1)\cos^2\alpha_{23}\sin^2\alpha_{23} - \cos\alpha_{23}\cos(2\theta_1)\cos(2\theta_3)\sin(2\theta_3) + \cos(2\alpha_{23})\cos^2\alpha_{23}\cos^2(2\theta_3)\sin(2\theta_1) + 4\cos^2\alpha_{23}\sin^2\alpha_{23}\cos(2\theta_3)\sin(2\theta_1) + \cos(2\alpha_{23})\cos(2\theta_1)\cos(2\theta_3)\cos\alpha_{23}\sin(2\theta_3)$

(3.1) $2\sin\alpha_{23}(\cos^2\alpha_{23} + \cos(2\theta_3) - \cos^2\alpha_{23}\cos(2\theta_3))(-\cos\alpha_{23}\sin(2\theta_1) + \cos(2\theta_1)\sin(2\theta_3) + \cos\alpha_{23}\cos(2\theta_3)\sin(2\theta_1))$

(4.1) 0

(1.2) $-2\cos\alpha_{23}\cos(2\theta_1)\cos(2\theta_3)\sin(2\theta_3)\sin^2\alpha_{23}\sin(2\theta_3) - \sin(2\alpha_{23})\sin\alpha_{23}\cos(2\theta_1)\sin(2\theta_3) + \sin(2\theta_1)(\sin^2(2\theta_3)\cos(2\alpha_{23}) + \cos^2(2\theta_3))$

(2.2) $-\cos^2\alpha_{23}\cos(2\theta_1)\sin^2(2\theta_3) + \cos(2\alpha_{23})\sin^2\alpha_{23}\cos(2\theta_1) + \sin(2\alpha_{23})\sin\alpha_{23}\sin(2\theta_1)\sin(2\theta_3) - \cos(2\alpha_{23})\cos^2\alpha_{23}\cos(2\theta_1)\cos^2(2\theta_3) - 4\cos^2\alpha_{23}\sin^2\alpha_{23}\cos(2\theta_1)\cos(2\theta_3) - \cos(2\theta_3)\sin(2\theta_1)\sin(2\theta_3)\cos\alpha_{23} + \cos(2\alpha_{23})\cos\alpha_{23}\cos(2\theta_3)\sin(2\theta_1)\sin(2\theta_3)$

(3.2) $2\sin\alpha_{23}(\cos^2\alpha_{23} + \cos(2\theta_3) - \cos^2\alpha_{23}\cos(2\theta_3))(\cos\alpha_{23}\cos(2\theta_1) + \sin(2\theta_1)\sin(2\theta_3) - \cos\alpha_{23}\cos(2\theta_3)\cos(2\theta_1))$

(4.2) 0

(1.3) $2\sin\alpha_{23}\sin(2\theta_3)\,(\cos^2\alpha_{23} + \cos(2\theta_3) - \cos^2\alpha_{23}\cos(2\theta_3))$

(2.3) $2\sin\alpha_{23}(\cos^2\alpha_{23} + \cos(2\theta_3) - \cos^2\alpha_{23}\cos(2\theta_3))(\cos\alpha_{23}\cos(2\theta_1) + \sin(2\theta_1)\sin(2\theta_3) - \cos\alpha_{23}\cos(2\theta_3)\cos(2\theta_1))$

(3.3) $8\sin^2\alpha_{23}\sin^2\theta_3 - 8\sin^2\theta_3\sin^4\alpha_{23} + 2\sin^4\alpha_{23}\sin^2(2\theta_3) - 1$

(4.3) 0

(1.4) $-a_{78}\cos\theta_1(\cos^2(2\theta_3) + \sin^2(2\theta_3)\cos(2\alpha_{23})) + 0.5a_{78}\sin\theta_1\cos\alpha_{23}\sin(4\alpha_{23})\,(1 + \cos(2\alpha_{23})) - a_{78}\sin\alpha_{23}\sin\theta_1\sin(2\alpha_{23})\sin(2\theta_3) - a_{9,10}\cos(2\alpha_{23})\sin\theta_3\sin(2\theta_3) - a_{9,10}\cos\theta_3 - a_{78}\cos\theta_3$

(2.4) $-a_{78}\cos\theta_1\sin(2\theta_3)(\sin(2\alpha_{23})\sin\alpha_{23} - \cos\alpha_{23}\cos(2\theta_3) + \cos(2\alpha_{23})) + a_{78}\sin\theta_1\cos\alpha_{23}(-\cos(2\alpha_{23})\cos\alpha_{23}\cos(2\theta_3)\sin(2\theta_3) - \cos\alpha_{23}\sin^2(2\theta_3) - \sin(2\alpha_{23})\cos(2\theta_3)) - a_{78}\sin\alpha_{23}\sin\theta_1(-\cos(2\alpha_{23})\sin\alpha_{23} + \cos\alpha_{23}\sin(2\alpha_{23})\cos(2\theta_3)) + a_{9,10}\cos\theta_3\sin(2\theta_3)\cos\alpha_{23} - a_{9,10}\cos(2\alpha_{23})\cos\alpha_{23}\sin\theta_3\cos(2\theta_3) + a_{11,12}\cos\alpha_{23}\sin\theta_3 - a_{9,10}\sin(2\alpha_{23})\sin\alpha_{23}\sin\theta_1$

(3.4) $-a_{78}\cos\theta_1(\cos\alpha_{23}\sin(2\alpha_{23})\sin(2\theta_3) + \sin(2\theta_3)\cos(2\theta_3)\sin\alpha_{23} - \cos(2\alpha_{23})\sin\alpha_{23}\sin(2\theta_3)\cos(2\theta_3)) + a_{78}\cos\alpha_{23}\sin\theta_1(\sin^2(2\theta_3)\sin\alpha_{23} - \sin(2\alpha_{23})\cos\alpha_{23}\cos(2\theta_3) + \cos(2\alpha_{23})\cos^2(2\theta_3)\sin\alpha_{23}) - a_{78}\sin\theta_1\sin\alpha_{23}(-\cos\alpha_{23}\cos(2\alpha_{23}) - \sin(2\alpha_{23})\sin\alpha_{23}\cos(2\theta_3)) - a_{9,10}\cos\theta_3\sin(2\theta_3)\sin(2\alpha_{23}) + \sin\theta_3(a_{9,10}\sin\alpha_{23}\sin(2\theta_3)\cos(2\alpha_{23}) - a_{11,12}\sin\alpha_{23} - a_{9,10}\cos\alpha_{23}\sin(2\alpha_{23}))$

(4.4) 1

Appendix D

The sample Matlab® code of the rigid origami simulator for the Absent Panels prototype.

Calculate the degree of freedom

```
j=83; % Number of joints.
tb=51; % Number of links.
s=1; % Removed constraints for partial fixed joints.
DoF=5*tb-3*j-6+s;
```

Input variables

```
N=3000; % N=Number of iterations.
% NTP=Number of total nodes.
NTP=19;
% FP=Fixed nodes.
FP=[2,4,6];
% PFP=Partial fixed nodes.
PFP=19;
% If a node is partially fixed and it moves along z axis, for example, the
% x axis and y axis of that node needs to be constrained, noted as 1 and 2.
del=[1,2];
% NBar=Number of the bars
NBar=45;
% Stipulate the magnitude and the direction of predictor step
PS=0.5;
delta=PS*ones(N,1);
% Construct the matrices
x=zeros(N+1,NTP);
y=zeros(N+1,NTP);
z=zeros(N+1,NTP);
R=zeros(N,NBar); % R=real-time length of bars.
% The display area
DisA = [-300 300 -300 300 -100 100];
% The coordinates of the initial configuration
x(1,:)=[0 -86.60 -86.60 0 86.60 86.60 -115.47 -230.94 -28.86...
    -144.34 -202.07 202.07 -28.87 28.87 28.87 115.47 230.94 144.34 0];
y(1,:)=[100 50 -50 -100 -50 50 100 100 250 ...
    -50 -150 150 -150 -250 150 -100 -100 50 0];
z(1,:)=0;
% Detection parameters
DAs=2;
DP=9;
% These parameters stipulate the coordinates which are being detected.
% In this case, the y-coordinates of the node No.9 is selected to be
% checked if there is a change of motion direction.
% G=The nodal pairs, which describes the node-bar relationship.
G=[1 19;3 19;5 19;1 2;1 6;5 6;4 5;3 4;2 3;...
    1 7;7 8;7 15;2 7;1 15;3 11;8 10;8 11;6 15;...
```

```
    1 9;10 11;3 10;11 13;3 13;2 10;11 14;10 13;13 14;...
    16 18;4 13;5 17;12 18;4 16;14 16;12 15;9 15;14 17;...
    9 12;16 17;5 16;5 18;17 18;12 17;8 9;7 9;6 18];
% L=Bar length.
L=findlength(G(:,1),G(:,2),x,y,z,0);
% RP=Reference nodes. In corrector steps, the free nodes are pulled
% towards the reference nodes.
RP=[6 2 2 4 4 6 2 7 7 2 10 15 4 13 6 4 16 6 19];
% Show the configuration at the Ith step
I=1000;
% Use numbers to represent axes
if DAs==1
    DA=x;
elseif DAs==2
    DA=y;
else
    DA=z;
end
```

Predictor-corrector algorithm

```
for i=1:N

    XYZ=[x(i,:);y(i,:);z(i,:)];
    % Construct the equilibrium matrix H
    E=1; % The Eth row in the equilibrium matrix H.
    TPS=1:NTP; % TPS=The matrix contains the sequential numbers of the
    % non-foundation nodes
    TPS(FP)=[];
    % By equating to an empty space, the sequential numbers of the fully
    % fixed nodes are deleted
    H=zeros(3*length(TPS),NBar);
    % tp=Sequential numbers of the nodes at one end of the bar
    for tp = TPS
        [r,c]=find(G==tp); % Find tp from G. The sequences of rows and
        % columns are listed, respectively.
        cp=zeros(size(r));
        % cp=Sequential numbers of the nodes at the other end of the bar
        for NBTP=1:length(r)
            % NBTP=Number of bars connected to the point tp
            cp(NBTP)=G(r(NBTP),3-c(NBTP));
            % If an entry in a row is selected, the other entry in this row
            % is picked up accordingly.
        end
        H(E:E+2,r)=repmat(XYZ(:,tp),1,length(r))-XYZ(:,cp);
        E=E+3;
    end
    % For partial fixed nodes, if the motion along a particular direction
    % is constrained, the corresponding entries in H are removed.
    if ~isempty(PFP)
        H((find(TPS==PFP)-1)*3+del,:)=[];
        notdel=[1 2 3];
```

```
        notdel(del)=[];
    else notdel=[];
    end
    LL=repmat(L,size(H,1),1);
    H=H./LL; % The equilibrium matrix H is obtained.
    % Solving the nodal displacements
    nullspace=null(H'); % H' is the transpose of H
    % The rank of H
    ank=rank(H);
    % The reduced echelon form of H
    rra=rref(H);
    % The detection step
    if i>3
        d1 = (DA(i,DP)-DA(i-1,DP))*(DA(i-1,DP)-DA(i-2,DP));
        d2 = (DA(i-1,DP)-DA(i-2,DP))*(DA(i-2,DP)-DA(i-3,DP));
    else
        d1 = 1;
        d2 = 1;
    end

    if d1<0 && d2<0 && i>3
        i=i-3; %#ok<FXSET>
        delta(i:end)=-delta(i:end);
    else
        newnullspace=nullspace*delta(i);
        %  RM=Reshape the new null space to a matrix form
        RMP=reshape(newnullspace(1:3*(length(TPS)-
length(PFP)),1),3,(length(TPS)-length(PFP)));
        %  RMP=RM + movements of the fixed node(zero)
        if ~isempty(PFP)
            RMP=[RMP(:,1:find(TPS==PFP)-1),[0;0;0],RMP(:,find(TPS==PFP):end)];
            RMP(notdel,TPS==PFP)=newnullspace((find(TPS==PFP)-1)*3+1);
        end
        NS=RMP;
        for DI=FP
            NS=[NS(:,1:DI-1),[0;0;0],NS(:,DI:end)];
        end
        M=NS+XYZ;
        %  RPm=Reference points in matrix form
        RPm=M(:,RP);
        %  Assign the lengths of bars between the free nodes and its
        %  reference nodes
        RPL=zeros(1,NTP);
        FP_PFP=[FP,PFP]; % Non-free nodes
        for ii=1:NTP
            if ii>RP(ii)&ii~=FP_PFP %#ok<BDSCI,AND2>
                RPL(ii)=L(G(:,1)==RP(ii)&G(:,2)==ii);
            elseif ii<RP(ii)&ii~=FP_PFP %#ok<BDSCI,AND2>
                RPL(ii)=L(G(:,1)==ii&G(:,2)==RP(ii));
            elseif max(ii==FP)
                RPL(ii)=100;
            else
                RPL(ii)=M(notdel,ii)-RPm(notdel,ii);
            end
```

```
        end
        RPL=repmat(RPL,3,1);
        % The corrector step
        % Construct the simultaneous equations to solve the correctors
        A=zeros(NBar,NTP);
        b=zeros(NBar,1);

        for bar=1:NBar
            [A(bar,G(bar,1)),A(bar,G(bar,2))]=calculateA(M,RPm,G,RPL,bar);
            b(bar) = findlength(G(bar,1),G(bar,2),M(1,:),M(2,:),M(3,:),0).^2-
L(bar)^2;
        end
        if ~isempty(PFP)
            [r,c]=find(G==PFP);
            A(r,PFP)=2*(M(notdel,PFP)-M(notdel,G(r,3-c(1))));
        end
        lambda=A(:,TPS)\b;
        for DI=FP
            lambda=[lambda(1:DI-1);0;lambda(DI:end)];
        end
        lambdaMT=repmat(lambda',3,1);
        XYZ_new=M-lambdaMT.*(M-RPm)./RPL;
        % The bar length are corrected and the coordinates are updated
        x(i+1,:)=XYZ_new(1,:);
        y(i+1,:)=XYZ_new(2,:);
        z(i+1,:)=XYZ_new(3,:);
        % Bar length inspection
        R(i,:)=findlength(G(:,1),G(:,2),x,y,z,i);
    end
end
```

Function ‘calculateA’

```
function [a,b]=calculateA(M,RP,G,RPL,bar)

aa=G(bar,1);
bb=G(bar,2);
a = sum((M(:,bb)-M(:,aa)).*(M(:,aa)-RP(:,aa)))*(-2)/RPL(1,aa);
b = sum((M(:,bb)-M(:,aa)).*(M(:,bb)-RP(:,bb)))*2/RPL(1,bb);
```

Function ‘findlength’

```
function length = findlength(point1,point2,x,y,z,i)

length = sqrt((x(i+1,point1)-x(i+1,point2)).^2+(y(i+1,point1)-
y(i+1,point2)).^2+(z(i+1,point1)-z(i+1,point2)).^2);
```

Output plots

```
x=x(1:i+1,:);

y=y(1:i+1,:);

z=z(1:i+1,:);

% The trajactories of motion for all nodes
figure
plot3(x(:,1:NTP),y(:,1:NTP),z(:,1:NTP),'g-')
xlabel('x')
ylabel('y')
zlabel('z')
axis equal
hold on
grid on
% The initial configuration of the assembly
mmm=1;
for nnn=1:length(G)
    plot3(x(mmm,G(nnn,:)),y(mmm,G(nnn,:)),z(mmm,G(nnn,:)),'--
','Color',[.35 .35 .35])
end
% The final configuration of the assembly
mmm=i;
for nnn=1:length(G)
    plot3(x(mmm,G(nnn,:)),y(mmm,G(nnn,:)),z(mmm,G(nnn,:)),'b-')
end
axis(DisA)
axis equal
grid on
```

The animation of the folding/deployment process

```
AN=[];% Animation
LaB=[];% The lable that shows the current step number
figure
mmm=1;
hold on
for nnn=1:length(G)
    plot3(x(mmm,G(nnn,:)),y(mmm,G(nnn,:)),z(mmm,G(nnn,:)),'--
','Color',[.5 .5 .5])
end
axis equal
axis(DisA)
view(2)
drawnow
for mmm=1:20:I
    delete(AN)
    delete(LaB)
    for nnn=1:length(G)
        AN(nnn)=plot3(x(mmm,G(nnn,:)),y(mmm,G(nnn,:)),...
            z(mmm,G(nnn,:)),'b-');  %#ok<SAGROW>
        grid on
```

```
    end
    LaB=text(300,300,180,num2str(mmm));
    drawnow
    % pause(0.005)
end
```

Published with MATLAB® R2015b